FACULDADE DE ENGENHARIA DA UNIVERSIDADE DO PORTO

# Development of a Switched Reluctance Motor Drive for an Electrical Vehicle

**Ricardo Miguel Mendanha Ferreira Pereira**

FOR JURY EVALUATION

U.PORTO

FEUP **FACULDADE DE ENGENHARIA**
UNIVERSIDADE DO PORTO

Master in Electrical and Computers Engineering

Supervisor: Adriano da Silva Carvalho

October 2016

# Resumo

O presente documento tem como objetivo o desenvolvimento de um motor de relutância comutada para tração de um veículo elétrico.

Uma breve comparação deste tipo de motores com outros é feita de modo a enfatizar as suas vantagens e limitações, uma das quais sendo a necessidade do uso de um conversor de potência. Apesar de existirem na literatura bastantes topologias possíveis para o conversor de potência, o documento foca-se na ponte assimétrica.

Apesar do princípio físico de funcionamento do motor ser simples, o seu controlo é complexo. Uma revisão geral dos métodos de controlo presentes na literatura são expostos. Uma síntese dos procedimentos de construção do motor é feita, partindo dos requisitos básicos, tais como a potência e a velocidade nominal. Através de uma análise do binário de saída em função das dimensões do motor, os aspectos finais da máquina são obtidos, tais como a suas características, como por exemplo o binário em função da corrente e posição.

Com o desenho do motor finalizado, foi elaborado um modelo de simulação do motor através do uso do MATLAB e Simulink fazendo uso dos parâmetros obtidos em simulações anteriores. Utilizando alguns dos métodos estudados durante o capítulo de revisão bibliográfica sobre métodos de controlo, um controlador foi desenvolvido e simulado.

Finalmente, como um meio para testar simulações anteriores, tanto o motor e o controlo, a validação experimental é preparada. Esta última componente é bem detalhada, contendo a selecção dos componentes que consituem a parte de potência, como os semicondutores e condensador para o barramento DC, bem como a seleção dos sensores de tensão e sensores de corrente e o microcontrolador que vai estar encarregue de executar o do algoritmo de controlo. É também detalhado o desenvolvimento da placa que faz a ligação entre a parte de potência e de sinal.

ii

# Abstract

The present document aims at the development of a switched reluctance motor drive for an electrical vehicle. In order to achieve the final goal, a thorough resume on the machine principle of operation including the influence of magnetic circuit saturation on motor characteristics is discussed.

A brief comparison with other machines is made as to emphasize its advantages and limitations, one of which is the need of a power converter. Despite the several possible topology's for the converter, the document focus on the asymmetric H-bridge.

Although the physical principles behind the reluctance motor are simple, its control is complex. A general review of the control methods present in the literature are exposed. A synthesis of motor design procedures is made, starting from the basic motor requirements, such as output power and rated speed, passing trough the analysis of the output torque as a function of the motor dimensions, up until the acquisition of the final machine aspects such as its static torque characteristic.

With the motor designed, a dynamic model was elaborated using MATLAB and Simulink software using the motor parameters computed in earlier design procedures. Using torque sharing functions with direct torque control technique as revised in earlier chapters, torque control is accomplished.

Finally as a means to test previous simulations, both the motor and the control, the experimental validation is prepared. This last and final component is well detailed, containing the selection of semiconductors and DC link capacitor for the power unit and the control unit composed by voltage and current sensors, as well as the microcontroller that is responsible for executing the control algorithm. The interface between the former two units is also developed and documented.

# Acknowledgments

I would first like to thank my dissertation advisor professor Adriano da Silva Carvalho for his guidance and trust.

My thanks to my fellow colleagues that shared the sleepless nights we were working together. Special mentions are my brother Tiago Pereira and Gabriel Ribeiro whom I had interesting discussions while sharing a dissertation area. A special gratitude for all those who helped me finish this dissertation, namely Bruno Silva for his continuous support and friendship, Alexandre Pires for being there in flower power with his gay lover, Pedro Faria for showing me that everything is possible through the hard work of others, Joaquim Ribeiro for countless adventures together, Lucija Kopić for sheltering me in my much needed vacations, Eduardo Dixo for showing me it doesn't matter, Lagostinho Rocha for discouraging me to give up and finally Rafael Martins for supplying the distraction moments in Tinder.

I also would like to express my gratitude to my friends that provided great moments throughout these years.

Last but not the least, I would like to thank my family.

Ricardo Pereira

*"It had long since come to my attention that people of accomplishment rarely sat back and let things happen to them. They went out and happened to things. "*

Leonardo Da Vinci

# Contents

# List of Figures

# List of Tables

# Abbreviations and Symbols

| | | |
|---|---|---|
| AC | Alternate Current | |
| ADC | Analog to digital converter | |
| ADITC | Advanced Direct Instantaneous Torque Control | |
| ATC | Average Torque Control | |
| DAC | Digital to analog converter | |
| DC | Direct Current | |
| DITC | Direct Instantaneous Torque Control | |
| EMF | Electromotive Force | [V] |
| FEA | Finite element Analysis | |
| IC | Integrated circuit | |
| PWM | Pulse Width Modulation | |
| RPM | Revolutions per minute | |
| SRM | Switched Reluctance Motor | |
| TSF | Torque Sharing Function | |
| VEC | Veículo de competição elétrica | |
| $R_{Goff}$ | Turn off gate resistance | [Ω] |
| $R_{Gon}$ | Turn on gate resistance | [Ω] |
| $(\Delta i)$ | Current ripple | [A] |
| $\beta_r$ | Rotor pole arc angle | [°] |
| $\beta_s$ | Stator pole arc angle | [°] |
| $\Delta T_H$ | Torque error histeresis band | [$N \cdot m$] |
| $\eta$ | Efficiency | |
| $\eta_{slot}$ | Filling factor | |
| $\omega_m$ | Machine angular speed | [rad/s] |
| $\phi$ | Flux | [Wb] |
| $\psi$ | Flux-linkage | [V·s] |
| $\psi^*$ | Reference Flux-linkage | [V·s] |
| $\psi_{peak}$ | Peak flux | [$V \cdot s$] |
| $\sigma_s$ | Ratio between aligned saturated inductance and aligned unsaturated inductance | |
| $\sigma_u$ | Ratio between aligned unsaturated inductance and unaligned inductance | |
| $\tau_r$ | Rotor pole pitch | [°] |
| $\tau_s$ | Stator pole pitch | [°] |
| $\theta$ | Rotor position | [rad] |
| $\theta_{dwell}$ | Conduction angle | [°] |
| $\theta_{off}$ | Turn-off angle | [°] |
| $\theta_{on}$ | Turn-on angle | [°] |
| $\theta_{ov}$ | Overlap angle | [°] |
| $\theta_a$ | Advance angle | [°] |

| | | |
|---|---|---|
| $\theta_c$ | Conduction angle | [°] |
| $\theta_f$ | Fall angle | [°] |
| $\theta_i$ | Current conduction angle | [°] |
| $\theta_m$ | Position where the inductance slope changes from zero to positive | [[°]] |
| $\theta_p$ | Rotor period | [°] |
| $\theta_p predicted$ | Predicted next rotor position | [°] |
| $\theta_z$ | Position where the phase current reaches zero | [°] |
| $\varepsilon^\circ$ | Step angle | [°] |
| $< I_D >$ | Average diode current | [A] |
| $A_{coil}$ | Coil winding area | $[m^2]$ |
| $A_{sp}$ | Area of stator pole | $[m^2]$ |
| $A_s$ | Specific electric loading | [A / m ] |
| $B_m$ | Total Friction | $[kg \cdot m \cdot s^{-2}]$ |
| $C_{min}$ | Minimum DC-link capacitance | [F] |
| $d_{sh}$ | Shaft diameter | [m] |
| $D_r$ | Rotor diameter | [m] |
| $D_t$ | Duty cycle | |
| $Ds_i$ | Stator inner diameter | [m] |
| $Ds_o$ | Stator outer diameter | [m] |
| $f_{fall}$ | Function defining the falling torque | |
| $f_{rise}$ | Function defining the rising torque | |
| $f_{sw}$ | Switching frequency | [Hz] |
| $f_s$ | Stator phase frequency | [Hz] |
| $h_{coil}$ | Stator coil length | [m] |
| $h_r$ | Rotor Pole height | [m] |
| $h_s$ | Stator Pole height | [m] |
| $I_{coil}$ | Coil current | [A] |
| $I_{G(off)\_peak}$ | Gate discharging peak current | [A] |
| $I_{G(on)\_peak}$ | Gate charging peak current | [A] |
| $I^2_{G(on)RMS}$ | Root mean square current flowing trough the gate resistor | [Ω] |
| $I_{OUT(avg)}$ | Average driver output current | [A] |
| $I_{OUT(avg)}$ | Average driver output current | [A] |
| $I_{ph}$ | Current flowing trough a phase winding | [A] |
| $I_{ref}$ | Reference current | [A] |
| $I_{RMS_{Diode}}$ | Root mean square current flowing trough the Diode | [A] |
| $I_{RMS_{IGBT}}$ | Root mean square current flowing trough the IGBT | [A] |
| $I_{RMS}$ | Rated rms current | [A] |
| $I_T$ | RMS current of a asymmetric H-bridge transistor | [A] |
| $I_A$ | Current flowing in phase A | [A] |
| $I_B$ | Current flowing in phase B | [A] |
| $I_G$ | Gate current | [A] |
| $I_p$ | Maximum allowed phase current | [A] |
| $J$ | Current density | $[A/mm^2]$ |
| $J_m$ | Total Inertia | $[kg \cdot m^2]$ |
| $k_d$ | Duty cycle | |
| $k_L$ | Ratio between stator length and inner stator diameter | |
| $K_o$ | Output coefficient | |

| $L_{fe}$ | Stator Core length | [m] |
|---|---|---|
| $L_a^s$ | Saturated aligned inductance | [H] |
| $L_a^u$ | Aligned but unsaturated inductance | [H] |
| $L_u$ | Unaligned inductance | [H] |
| $M_{AB}$ | Mutual inductance between phase A and B | [H] |
| $M_a$ | System angular momentum | $[[N \cdot m \cdot s]$ |
| $N_{coil}$ | Number of turns per coil | |
| $N_{ph}$ | Number of phases | |
| $N_r$ | Number of rotor poles | |
| $n_c$ | Number of coils per phase | |
| $n_n$ | Rated Speed | [RPM] |
| $N_s$ | Number of stator poles | |
| $P_{cond_{Diode}}$ | Switching losses from the IGBT | [W] |
| $P_{cond_{IGBT}}$ | Switching losses from the IGBT | [W] |
| $P_{cond}$ | Conduction losses | [W] |
| $P_{cu}$ | Copper losses | [W] |
| $P_{G(on)}$ | Power dissipated by the turn on resistance | [Ω] |
| $P_{in}$ | Input Power | [W] |
| $P_{loss}$ | Power loss | [W] |
| $P_{mech}$ | Mechanical Power | [W] |
| $P_{sw_{IGBT}}$ | Switching losses from the IGBT | [W] |
| $P_{sw}$ | Switching losses | [W] |
| $P_{total_{conv}}$ | Switching losses from power converter | [W] |
| $P_n$ | Rated Power output | [W] |
| $Q_{rr}$ | Recovery charge | [C] |
| $Q_G$ | Gate charge | [C] |
| $R_{CE}$ | IGBT collector emitter resistance | [Ω] |
| $R_{Gmin}$ | Minimum gate resistance | [Ω] |
| $R_{ph}$ | Winding phase resistance | [Ω] |
| $R_F$ | Forward Diode resistance | [Ω] |
| $S_{cond}$ | Conductor cross section | $[m^2]$ |
| $T_{avg}$ | Average torque | $[N \cdot m]$ |
| $t_{cross}$ | Crossover period | [s] |
| $t_{down}$ | Flux falling time | [s] |
| $T_{err}$ | Torque error | $[N \cdot m]$ |
| $T_L$ | Load Torque | $[N \cdot m]$ |
| $T_{max}$ | Maximum torque | $[N \cdot m]$ |

| | | |
|---|---|---|
| $T_{max}$ | Maximum torque | $[N \cdot m]$ |
| $T_{min}$ | Minimum torque | $[N \cdot m]$ |
| $T_{ripple}$ | Torque ripple | |
| $t_{rr}$ | Reverse recovery time | [s] |
| $t_{up}$ | Flux rising time | [s] |
| $T_e$ | Electromagnetic Torque | $[N \cdot m]$ |
| $T_n$ | Rated Torque | $[N \cdot m]$ |
| $t_r$ | Rotor Pole width | [m] |
| $T_s$ | Sampling time | [s] |
| $t_s$ | Stator Pole width | [m] |
| $T_x$ | Torque produced by phase x | $[N \cdot m]$ |
| $T_y$ | Torque produced by phase x | $[N \cdot m]$ |
| $U_{ph}$ | Voltage applied to a phase winding | [V] |
| $V_{ph}^*$ | Required output voltage | [V] |
| $V_{dc}$ | Dc link voltage | [V] |
| $V_F$ | Forward voltage drop | [V] |
| $V_G-$ | Turn off voltage | [V] |
| $V_G+$ | Turn on voltage | [V] |
| $w_{coil}$ | Stator coil width | [m] |
| $w_{cs}$ | Space between two stator coils | [m] |
| $W_c$ | Magnetic field co-energy | [J] |
| $W_f$ | Magnetic field energy | [J] |
| $y_r$ | Rotor Yoke Thickness | [m] |
| $y_s$ | Stator Yoke Thickness | [m] |
| B | Flux density | [Wb/$m^2$] |
| g | Air gap | [m] |
| L | Self inductance | [H] |
| M | Multiplicity | |
| m | Number of phases conducting simultaneously | |
| MMF ($\theta_{coil}$) | Magnetomotive force | [Ampere/turn] |
| N | Number of Turns per phase | |
| P | Power developed by the machine | [W] |
| Q | Energy conversion ratio | |
| S | Loops per revolution | |

# Chapter 1

# Introduction

Within the following dissertation the design of a switched reluctance motor and drive is accomplished. Said design includes the development of the electric motor as well as the development of an electronic power converter that will later enable its control. The proposed theme covers a large number of electrical engineering topics, from electromagnetism and electric machines to power electronics, systems control and programming. The work was done together with Tiago Pereira and Gabriel Ribeiro, whose dissertations were within the same domain and with the supervision of professor Adriano Carvalho and Armando Araújo.

## 1.1 Motivation

By definition an electric machine is a system that converts mechanical energy into electrical energy or vice versa. The development of electric machines is a field that even today has considerable amount of research. Nowadays electric machines consume about 85% of the electrical energy in the world and research is mostly driven by the motivation for higher efficiency and lower cost [1]. New trends in the area are the switched reluctance motors (SRMs) which are going to be the focus of the dissertation. Although the SRM is one of the oldest motors, dating back since 1800s, only recently started to emerge in the market due to the advances in the semiconductor industry, power electronics and microprocessors.

The SRM is a viable candidate for variable speed applications, because of its high torque density, low losses, wide speed range capability and the absence of permanent magnets or windings in the rotor makes it a low-cost machine. Despite its inherent advantages over the conventional machines, during its operation the output torque contains high ripple and therefore emit significant amounts of vibration making the machine unsuitable for certain applications [2] [3]. The final goal of the dissertation is the development of a motor and a control algorithm capable of achieving a low torque ripple.

## 1.2   Scope of the Dissertation

The following dissertation aims to document the design and the eventual implementation of a switched reluctance motor drive with the minimum torque ripple. A thorough review of the state of the art of motor drives is presented, which includes the fundamentals of operation of the machine and its control schemes. The boundaries of the dissertation were on the practical implementation of the algorithm, considering that at the beginning of the dissertation there wasn't a switched reluctance motor available within the premises. The supervisor and student along with the collaboration of *WEG* designed and manufactured a reluctance machine. The requirements and its design criteria are properly justified. With the motor characteristics acquired, the control algorithm was simulated via Simulink.

## 1.3   Dissertation Structure

This document is divided into 8 chapters. An overview of the switched reluctance motor characteristics is presented in chapter 2. The typical power converters used in Switched reluctance machines are reviewed in chapter 3, with a focus on the asymmetric H-bridge. Within chapter 4 a thorough review of the control schemes presented in the literature are depicted. The design procedure of the motor is presented in chapter 5. During chapter 6 the control of the developed motor is simulated. With all the theoretical work prepared in the earlier chapters, in chapter 7 the experimental validation is planned. Chapter 8 presents the dissertation final conclusions and some suggestions for future work are described.

# Chapter 2

# Switched Reluctance Motor

## 2.1 Introduction

Ever since the invention of the electric motor by Moritz Hermann Jacobi, there has been a continuous research and development focused on electric machines. The Switched Reluctance Motor elementary versions date back since the early 1800s. However, the problem of de-energizing the inductors remained an unsolved challenge [4].

Recently due to the innovations on the power electronics field, these motors have resurfaced and the technology is now slowly penetrating into the industry with the promise of providing an efficient drive system at a lower cost [5].

Within the following chapter an overview of these type of motors is made that includes their physical principle of operation as well as their advantages and limitations.

## 2.2 Configuration

Like every electric motor, the SRM is composed by a stator and a rotor. The stator consists of steel laminations forming salient poles with series of coil windings enveloping them. The rotor is also made of steel laminations, but without any windings or magnets, making it the only motor with salient poles on both the rotor and the stator (double salient).

This trait gives them some inherent advantages over conventional machines. Taking into consideration that the rotor has no windings or magnets, it is cheaper to manufacture. The absence of copper losses on the rotor, imply that the major sources of heat are on the stator, therefore cooling is simpler. Furthermore the rotor has a low moment of inertia, hence it can accelerate faster than the traditional motor [2].

However due to its double saliency, the machine characteristics are highly non-linear, thus the production of an even torque is not an easy task. Some of the present limitations of the machine are its inherent torque ripple, which can be reduced by overlapping phase currents, acoustic noise and the complete dependence on a electronic power converter and a rotor position sensor [2].

3

In these machines, the number of poles on the rotor differ from the ones on the stator. The reason is that if the stator and rotor poles were exactly aligned, it would be impossible to develop a starting torque. The configurations with higher number of stator/rotor pole combinations have less torque ripple, at the cost of added complexity, and do not have the problem of starting torque [5].
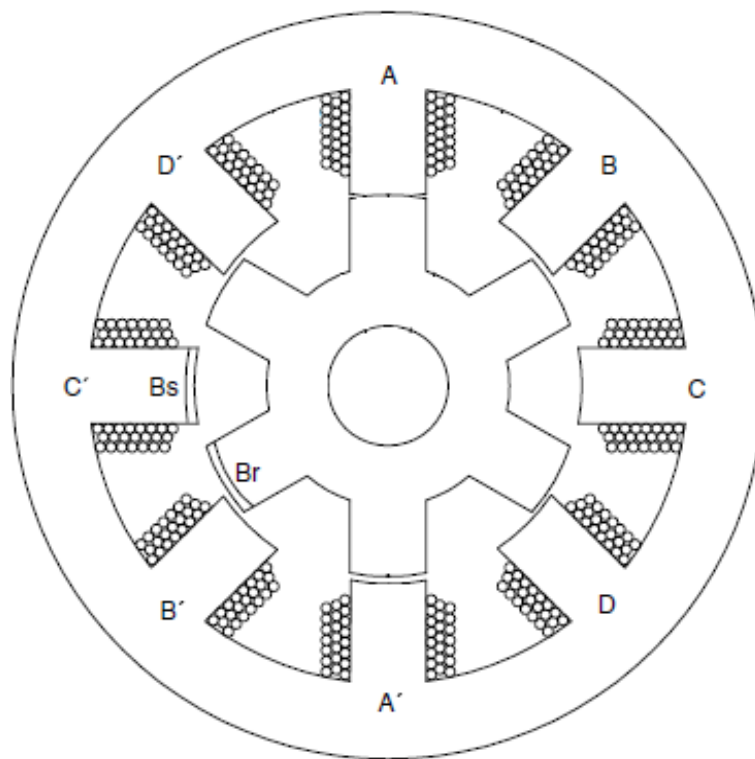


Figure 2.1: Cross section of a four phase 8/6 Switched Reluctance Motor [5]

The common stator/rotor pole configurations are 6/4, 8/6, 10/8. The figure 2.1 represents the cross section of a four phase motor, in which the stator and rotor pole arcs are represented, $\beta_s$ and $\beta_r$ respectively.

## 2.3   Principle of Operation

Opposite magnetic poles will attract each other with the tendency to bring them into alignment as much as possible in an effort to minimize the reluctance of the system [4]. Continuous torque can be produced by the synchronization of each phase excitation with the rotor position.

Since the torque is the result of the system trying to reach a state of minimum reluctance, it is called reluctance torque. Unlike other machines, such as the induction motor, which work by producing alignment torque or permanent magnet synchronous machine, which depending on the disposition of the magnets can use a combination of both.

In the following image, figure 2.2, there are four types of motors. Motor a) can only produce reluctance torque when winding 1 is excited, and alignment torque when both windings are excited. Motor b) similar to motor a) can produce alignment torque when both windings are excited and reluctance torque only when winding 1 is excited. Motor c) develops reluctance torque when either winding is excited and alignment torque when both windings are excited. Motor d) can't generate reluctance torque, only produces alignment torque when both windings are excited.
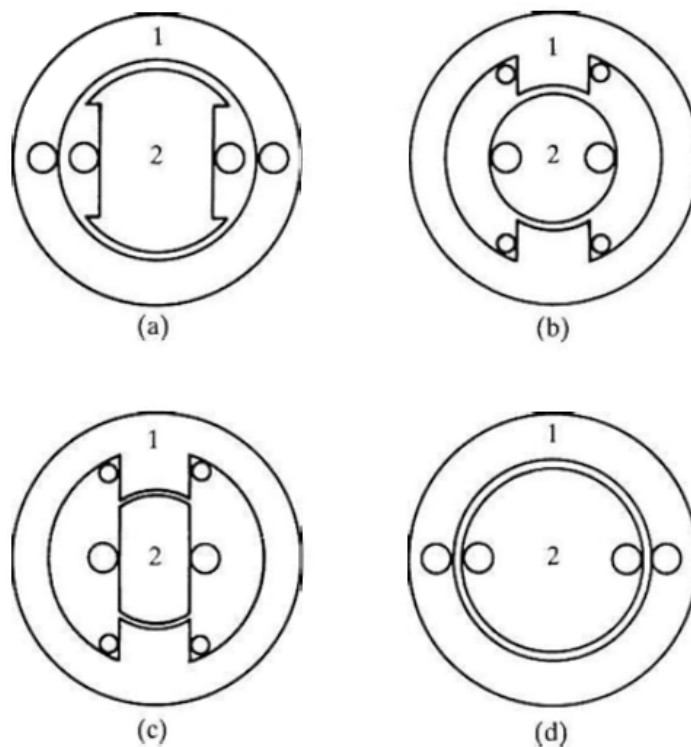


Figure 2.2: Illustrating reluctance torque and alignment torque [6]

### 2.3.1   Linear Model

In the conventional operation of the SRM, ideal inductance profiles are assumed. In the following subsection, the mathematical analysis is performed assuming a linear magnetic system. When the SRM is operating in a magnetically linear region, the inductance varies only as a function of rotor position.

A one phase switched reluctance machine is presented in figure 2.3.
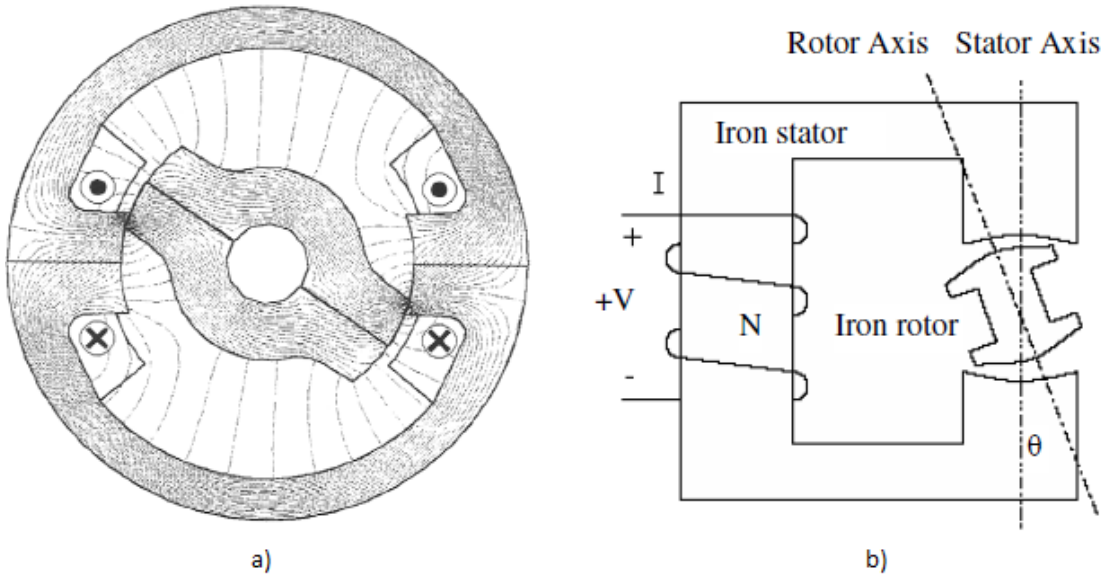


Figure 2.3: Simple single phase reluctances machines [3] [7]

A mathematical model of the motor torque can be derived by a simple resistor in series with a variable inductance when ignoring mutual inductance between phases.

According to Kirchoff's law, the direct sum of the electrical potential differences around any closed network equals zero. In the case of circuit diagram presented in figure 2.4, the instantaneous voltage across the terminals of a single phase of a Switched Reluctance Motor winding can be described as the sum of voltage drops in the phase resistance and induced voltage on the phase inductance. Since the mutual coupling between phases is very small, it is ignored.

The voltage equation governing one phase is

$$U_{ph} \;=\; I_{ph} \cdot R_{ph} + \frac{d\psi}{dt} \;\; [V] \tag{2.1}$$

In which $U_{ph}$ is the applied phase voltage, $I_{ph}$ is the phase current, $R_{ph}$ is the motor phase resistance, and $\psi$ is the flux-linkage in Volt-second.

Knowing that the machine's angular velocity speed can be expressed as
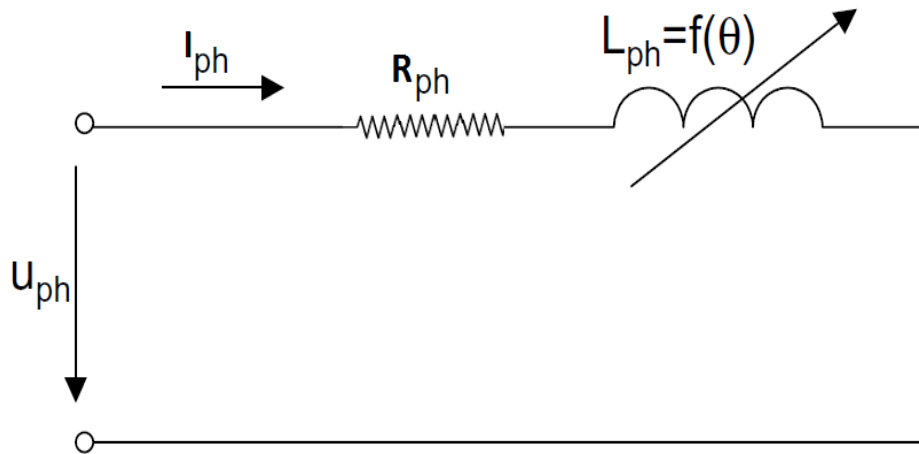
Figure 2.4: Equivalent circuit diagram of single phase SRM [8]

$$\omega_m = \frac{d\theta}{dt} \quad [rad/s] \tag{2.2}$$

Rearranging the equation 2.1

$$U_{ph} = I_{ph} \cdot R_{ph} + \frac{d\theta}{dt} \cdot \frac{d\psi}{d\theta} = I_{ph} \cdot R_{ph} + \omega_m \cdot \frac{d\psi}{d\theta} \quad [V] \tag{2.3}$$

The self and mutual flux linkages produced by a winding are proportional to the current in the winding. The ratio of flux linkage to the current that produces it, is therefore a constant and it is defined as the inductance of the winding. [9].

Assuming magnetic saturation does not occur, the self inductance (L) is given by 2.4

$$L = \frac{Self\ flux\ linkage}{Current} = \frac{\psi}{I_{ph}} \quad [H] \tag{2.4}$$

Therefore

$$U_{ph} = I_{ph} \cdot R_{ph} + \omega_m \cdot \frac{d(L \cdot I_{ph})}{d\theta} \quad [V] \tag{2.5}$$

The product rule states that the derivative of the product of two functions is the first function times the derivative of the second, plus the second function times the derivative of the first.

$$\frac{d(L \cdot I_{ph})}{d\theta} = L \cdot \frac{dI_{ph}}{d\theta} + I_{ph} \cdot \frac{dL}{d\theta} \quad [V] \tag{2.6}$$

Taking into consideration the above equation and recalling equation 2.2

$$U_{ph} \quad = \quad I_{ph} \cdot R_{ph} + L \cdot \frac{d\theta}{dt} \cdot \frac{dI_{ph}}{d\theta} + \omega_m \cdot I_{ph} \cdot \frac{dL}{d\theta} \quad [V] \tag{2.7}$$

$$U_{ph} \quad = \quad I_{ph} \cdot R_{ph} + L \cdot \frac{dI_{ph}}{dt} + \omega_m \cdot I_{ph} \cdot \frac{dL}{d\theta} \quad [V] \tag{2.8}$$

In the equation 2.8 the first two terms on the right-hand side represent the resistive voltage drop and the inductive voltage drop, and the last term represents what is sometimes interpreted as 'back-EMF' (electromotive force) $\varepsilon$ [3]

$$\varepsilon \quad = \quad \omega_m \cdot I_{ph} \cdot \frac{dL}{d\theta} \quad [V] \tag{2.9}$$

The instantaneous electrical power $I_{ph} \cdot U_{ph}$ is

$$U_{ph} \cdot I_{ph} \quad = \quad R_{ph} \cdot I_{ph}^2 + L \cdot I_{ph} \cdot \frac{dI_{ph}}{dt} + \omega_m \cdot I_{ph}^2 \cdot \frac{dL}{d\theta} \quad [W] \tag{2.10}$$

The magnetic energy $W_m$ stored by an inductor with current $I_{ph}$ is as follows

$$W_m \quad = \quad \frac{1}{2} \cdot L \cdot I_{ph}^2 \quad [J] \tag{2.11}$$

By definition, power is equivalent to the amount of energy consumed per time unit. The rate of change of magnetic stored energy at any instant is given by

$$\frac{d}{dt}\left(\frac{1}{2} \cdot L \cdot I_{ph}^2\right) \quad = \quad \frac{1}{2} \cdot I_{ph}^2 \cdot \frac{dL}{dt} + L \cdot I_{ph} \cdot \frac{dI_{ph}}{dt} = \frac{1}{2} \cdot I_{ph}^2 \cdot \omega_m \cdot \frac{dL}{d\theta} + L \cdot I_{ph} \cdot \frac{dI_{ph}}{dt} \quad [W] \tag{2.12}$$

The rate at which work is done by the motor is defined as

$$P \quad = \quad T_e \cdot \omega_m \quad [W] \tag{2.13}$$

The resistive losses, also know as copper losses ($P_{cu}$) are

$$P_{cu} \quad = \quad R_{ph} \cdot I_{ph}^2 \quad [W] \tag{2.14}$$

Taking into account the law of conservation of energy. After subtracting the copper losses ($P_{cu}$) and the rate of change of magnetic stored energy from the input power, what is left is nothing other than the mechanical power.

$$P \;=\; T_e \cdot \omega_m \;=\; U_{ph} \cdot I_{ph} - P_l - \frac{\mathrm{d}}{\mathrm{d}t}\left(\frac{1}{2} \cdot L \cdot I_{ph}^2\right) \;[W] \tag{2.15}$$

Thus from 2.15, and bearing in mind 2.12, 2.13 and 2.14, the instantaneous electromagnetic torque $T_e$ is given by

$$T_e = \left(R_{ph} \cdot I_{ph}^2 + L \cdot I_{ph} \cdot \frac{\mathrm{d}I_{ph}}{\mathrm{d}t} + \omega_m \cdot I_{ph}^2 \cdot \frac{\mathrm{d}L}{\mathrm{d}\theta} - R_{ph} \cdot I_{ph}^2 - \frac{1}{2} \cdot I_{ph}^2 \cdot \omega_m \cdot \frac{\mathrm{d}L}{\mathrm{d}\theta} - L \cdot I_{ph} \cdot \frac{\mathrm{d}I_{ph}}{\mathrm{d}t}\right) \cdot \frac{1}{\omega_m} \;[Nm]$$
$$\tag{2.16}$$

Resulting

$$T_e \;=\; \frac{1}{2} \cdot I_{ph}^2 \cdot \frac{\mathrm{d}L}{\mathrm{d}\theta} \;[Nm] \tag{2.17}$$

Hence, the sign of the torque is directly related to the sign of $\frac{\mathrm{d}\psi}{\mathrm{d}\theta}$. In other words, a positive torque is developed when the change in stator flux increases with respect to the rotor position, so to produce a negative torque, the change in stator flux should decrease with respect to the rotor movement. When $\frac{\mathrm{d}\psi}{\mathrm{d}\theta}$ is positive it may be defined as "flux acceleration" and when it is negative it may be defined as "flux deceleration" [10].

Since the torque is proportional to the square of the current, this machine resembles a DC series motor, hence it has good starting torque [2]. Considering that the current flow in a motor phase winding is always positive, unipolar power converter topologies can be used with less than two switches per phase.

### 2.3.2 Inductance Profile

The reluctance of the flux path between the two diametrically opposite stator poles varies as a pair of rotor poles rotates into and out of alignment. The inductance of a phase winding is maximum when the rotor is in the aligned position and minimum when the rotor is in the non aligned position.
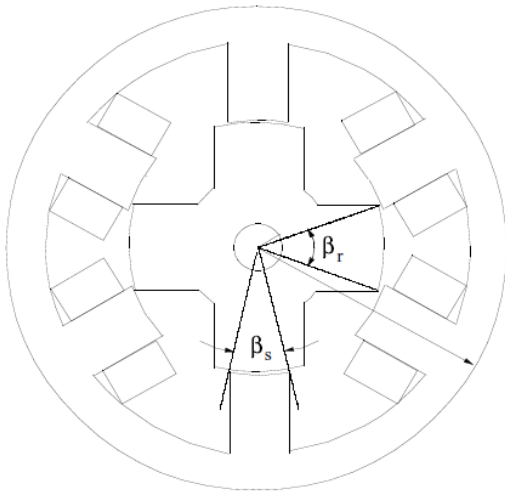
$$\theta_1 = \tfrac{1}{2} \cdot \left[ \tfrac{360}{N_r} - (\beta_s + \beta_r) \right] \qquad (2.18)$$

$$\theta_2 = \theta_1 + \beta_s \qquad (2.19)$$

$$\theta_3 = \theta_2 + (\beta_r - \beta_s) \qquad (2.20)$$

$$\theta_4 = \theta_3 + \beta_s \qquad (2.21)$$

$$\theta_5 = \theta_4 + \theta_5 = \tfrac{360}{N_r} \qquad (2.22)$$

Figure 2.5: SRM pole arcs [2]

The inductance profile presented in figure 2.6 can be analysed with the above equations, which depend on the pole arcs and number of poles presented in figure 2.5.
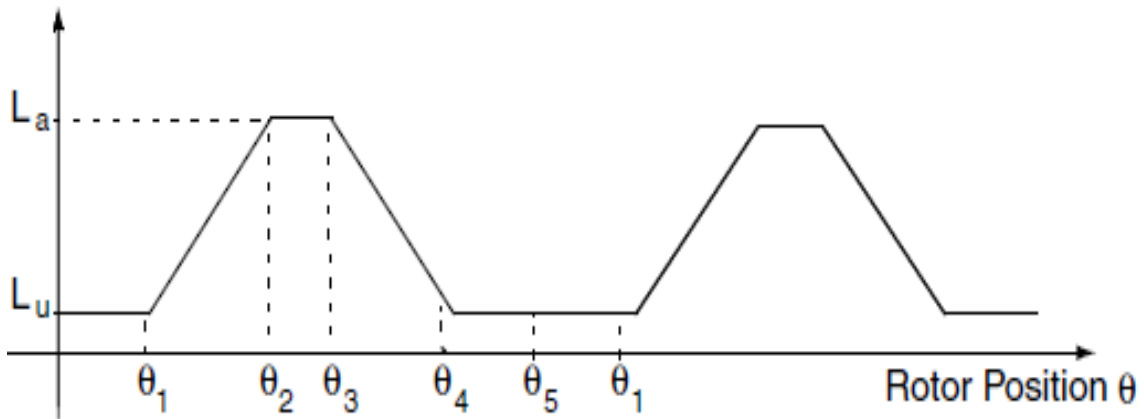


Figure 2.6: SRM Inductance profile [2]

As seen in figure 2.6, the variation of inductance is composed of four different zones, where the inductance varies in a range between unaligned inductance, $L_u$, and aligned inductance $L_a$.

In the first region, $(0 - \theta_1)$ and $(\theta_4 - \theta_5)$ neither the stator nor the rotor poles are aligned with each other, the inductance in this case is minimum and constant, the physical representation of this position is shown in figure 2.7.
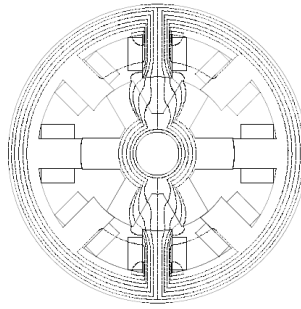
Figure 2.7: Flux paths at unaligned position [2]

In the second region, ($\theta_1$ - $\theta_2$) the rotor pole starts to align with the stator pole, so the inductance value gets increased with respect to rotor position. Similarly there is a zone, ($\theta_3$ - $\theta_4$), in which the rotor starts to misalign with respect to stator, thus the inductance value decreases. These positions are presented in figure 2.8.
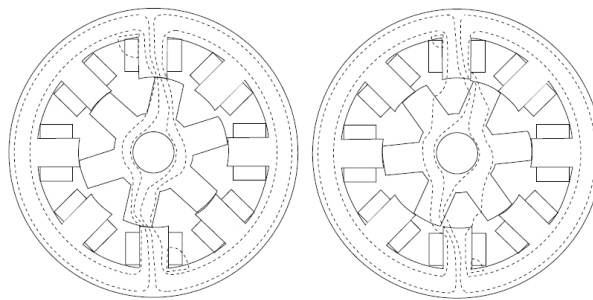


Figure 2.8: Flux distribution in the alignment and disalignment regions [2]

Between ($\theta_2$ - $\theta_3$), when the poles are completely aligned, the movement of rotor pole does not alter the complete overlap between the poles, hence the inductance is maximum and constant. It is possible to see in figure 2.9 the cross section of a motor with its poles aligned.
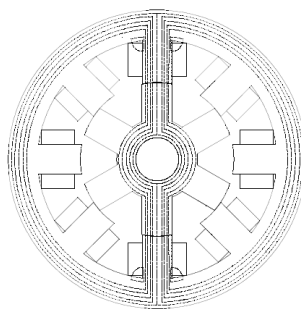


Figure 2.9: Flux paths at fully alligned position [2]

According to the relation defined earlier, between the electromagnetic torque, and the variation of the inductance.

$$T_e \; = \; \frac{1}{2} \cdot I_{ph}^2 \cdot \frac{dL}{d\theta} \; [Nm] \tag{2.18}$$

The torque produced over a period of the inductance variation, assuming a constant current, is presented in figure 2.10.
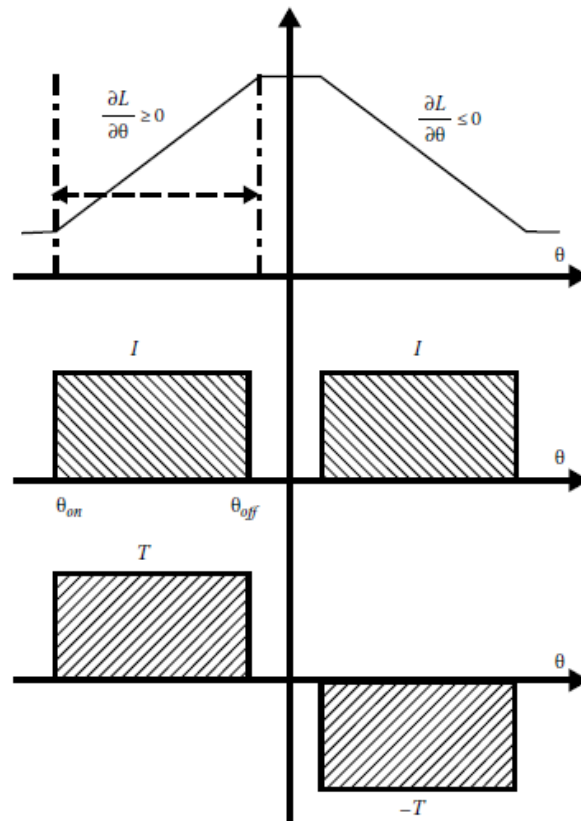


Figure 2.10: Torque production [4]

Negative torque generation can be avoided entirely with a dead zone ($\theta_3$ - $\theta_2$), given by ($\beta_r - \beta_s$), in which no torque is produced even if there is current present. Elimination of negative torque generation reduces the torque ripples and the audible noise generation.

### 2.3.3 Nonlinear Model

Although the analysis of the SRM is initially performed assuming a linear magnetic system, the machine is normally operated in the saturated region. The saturated motor operates in the same fashion as the linear one, however in the B(H) magnetization curve, saturation now limits the maximum flux-linkage to a smaller value. The inductance becomes function of phase current as well as rotor position.

To properly understand the electromagnetic energy conversion, a nonlinear analysis that takes into account the saturation of the magnetic circuit is needed. Such analysis is based on magnetization curves [11]. The difference between a saturating machine and a linear one is presented in figure 2.11, where an increase in applied external magnetic field does not increase the magnetization of the material.
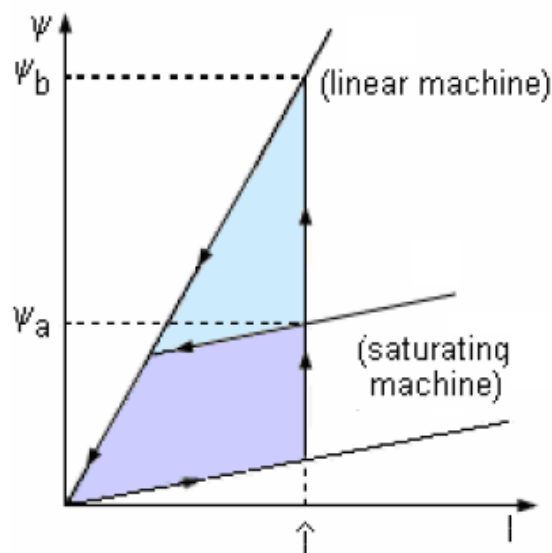


Figure 2.11: Idealizeed $\psi$-I-curves of linear SRM with the same maximum current

A typical current profile for the SRM excitation is shown in figure 2.12. The top trace denotes the ideal linearized inductance profile and the bottom trace denotes the ideal current profile. The rotor position is represented on the horizontal axes of both graphs and the rotor is moving from the unaligned position $\theta_u$ to the aligned position $\theta_a$.

For an ideal current profile such as the one presented in figure 2.12, when the rotor position matches the turn-on angle, $\theta_{on}$, the phase switches are turned on. As the current begins to increase, part of the input energy will be stored in the magnetic field. With the increasing inductance, the magnetic field energy will increase until the turn-off angle, $\theta_{off}$.

The other components of the input energy will be converted into mechanical work and loss.
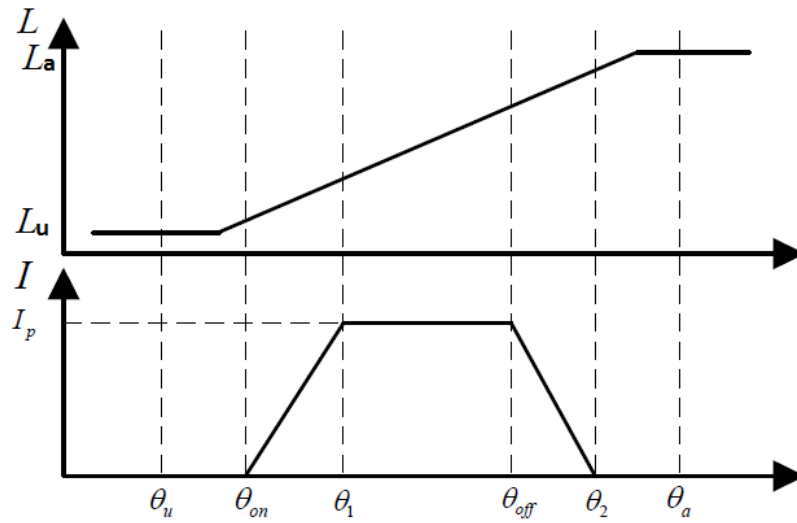
Figure 2.12: Typical SRM excitation current profile

When the rotor position matches the turn-off angle, the phase switches are turned off. The remaining magnetic field energy needs to be released.

Due to the larger inductance around the aligned position, the de-energization of the commutated current is not instantaneous which results in a small rotation before the current drops to zero. Thus some of the magnetic field energy is converted to into mechanical work and loss.
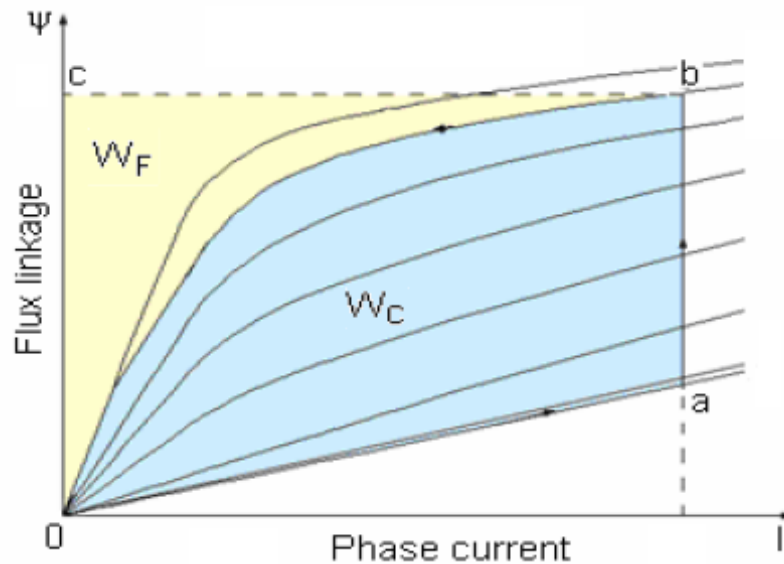


Figure 2.13: Energy conversion loop [11]

As presented in figure 2.13, the energy supplied by the converter (area *oabco*) can be divided into two parts.

The stored field energy $W_f$ (area *obco*) which is returned to the supply during commutation appart

from hysteresis losses and the co-energy $W_c$ (area *oabc*) that is available to be converted into mechanical work.

The magnetic field energy can be numerically determined by the equation 2.19, and graphically by the shaded area in figure 2.14.

$$W_f = \int_0^{\psi} I_{ph}(\theta, \psi) \; d\psi \quad [J] \tag{2.19}$$
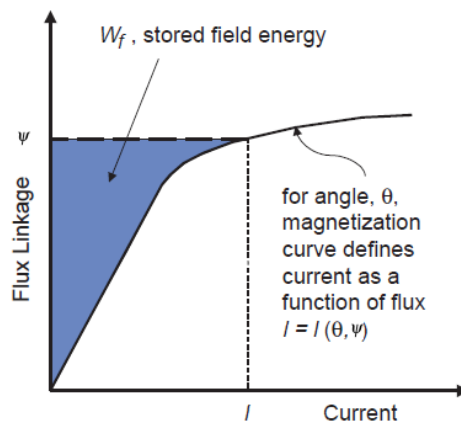


Figure 2.14: Graphical Interpretation of Magnetic Field Energy [12]

The magnetic field co-energy can be defined by the equation 2.20, and graphically by the shaded area in figure 2.15.

$$W_c = \int_0^{I_{ph}} \psi(\theta, I_{ph}) \; dI_{ph} \quad [J] \tag{2.20}$$
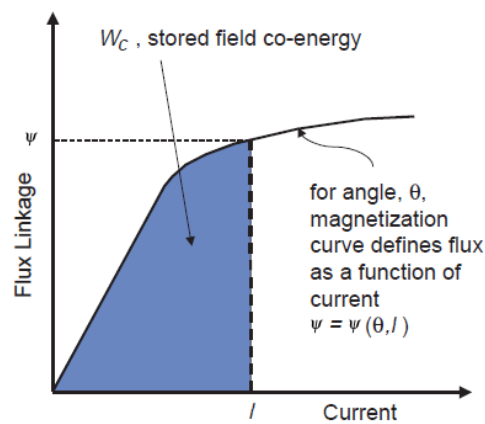


Figure 2.15: Graphical Interpretation of Magnetic Field Co-Energy [12]

Recalling the equation, 2.1, that governs one phase of the SRM. Multiplying each side by the electrical current, $I_{ph}$ , results in the expression for the instantaneous power in the motor.

$$U_{ph} \cdot I_{ph} \quad = \quad I_{ph}^2 \cdot R_{ph} + I_{ph} \cdot \frac{d\psi}{dt} \quad [W] \tag{2.21}$$

The first term in the right-hand side (RHS) of Equation 2.21 represent the ohmic losses in the SRM winding. If power is to be conserved, then the second term in the RHS of Equation 2.21 must represent the sum of the mechanical power output of the SRM and any power stored in the magnetic field. Thus,

$$I_{ph} \cdot \frac{d\psi}{dt} \quad = \quad \frac{dW_f}{dt} + \frac{dW_c}{dt} \quad [W] \tag{2.22}$$

Where, $\frac{dW_c}{dt}$ is the instantaneous mechanical power and $\frac{dW_f}{dt}$ is the instantaneous power, which is stored in the magnetic field. Because power, by it's own definition is the time rate of change of energy, $W_c$ is the mechanical energy and $W_f$ is the magnetic field energy.

Since mechanical power can be written as the product of torque and speed,

$$\frac{dW_c}{dt} \quad = \quad T_e \cdot \omega \quad = \quad T_e \cdot \frac{d\theta}{dt} \quad [W] \tag{2.23}$$

Where, $T_e$ stands for torque, and $\omega$ stands for rotational velocity of the shaft. Substitution of Equation 2.23 into Equation 2.22 results in

$$I_{ph} \cdot \frac{d\psi}{dt} \quad = \quad T_e \cdot \frac{d\theta}{dt} + \frac{dW_f}{dt} \quad [W] \tag{2.24}$$

Solving Equation 2.24 for torque yields the equation,

$$T_e(\theta, \psi) \quad = \quad I_{ph}(\theta, \psi) \cdot \frac{d\psi}{d\theta} - \frac{dW_f(\theta, \psi)}{d\theta} \quad [Nm] \tag{2.25}$$

From figures 2.14 and 2.15, the area defining the field energy and co-energy can be described by following relation

$$W_c + W_f \quad = \quad I_{ph} \cdot \psi \quad [J] \tag{2.26}$$

Differentiating both sides of the equation 2.27 results in

$$dW_c + dW_f \quad = \quad I_{ph} \cdot d\psi + \psi \cdot di \qquad (2.27)$$

Solving for the differential field energy in Equation 2.27 and substituting back into Equation 2.25 gives,

$$T_e \quad = \quad \frac{I_{ph} \cdot d\psi - (\psi \cdot dI_{ph} + I_{ph} \cdot d\psi - dW_c(\theta, I_{ph}))}{d\theta} \quad [Nm] \qquad (2.28)$$

For simplification, the general torque equation, equation 2.28, is usually simplified for values of constant current. The differential co-energy can be written in terms of its partial derivatives as

$$dW_c(\theta, I_{ph}) \quad = \quad \frac{\partial W_c}{\partial \theta} \cdot d\theta + \frac{\partial W_c}{\partial I_{ph}} \cdot dI_{ph} \qquad (2.29)$$

From Equation 2.28 and Equation 2.29, it is fairly easy to show that under constant current

$$T_e \quad = \quad \frac{\partial W_c}{\partial \theta} \quad [Nm] \qquad (2.30)$$

The graph in figure 2.16 is drawn for a motor with the same unsaturated inductance ratio and the same energy conversion, (and therefore the same torque). Saturation now limits the maximum flux linkage to a smaller value, and if the rotor displacement between A and C is unchanged, then the supply voltage must be reduced. In other words, the saturating motor cannot accept as large a voltage impulse (voltage-time integral) as the non-saturating motor. For the same energy conversion, the maximum current must now be greater.
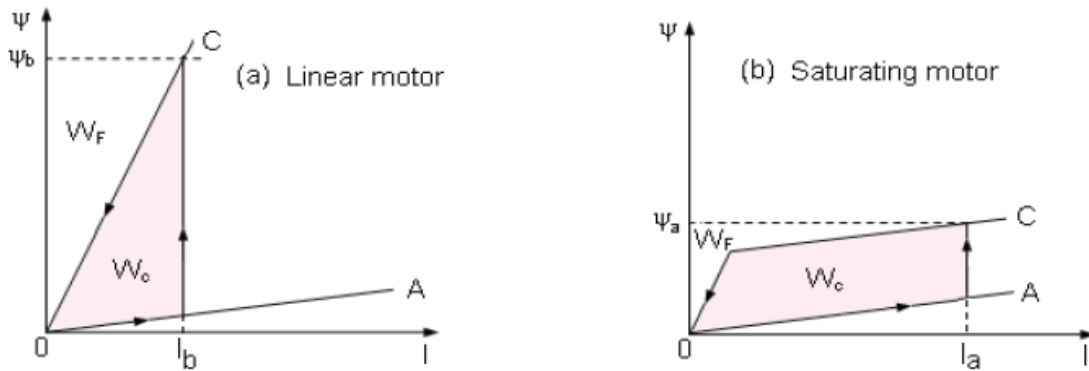


Figure 2.16: Idealized $\psi$- I - curves: a) linear and b) saturating SRM for the same torque [11]

However for the same enclosed area $W_c$, the *V·I* product is lower in the saturated motor compared to the linear one. For a given torque and speed, the saturation decreases the inverter VA re-

quirement. If there were no saturation, then the Switched Reluctance drive would have no chance of competing with the induction motor in terms of inverter kVA. Saturation therefore generally leads to a smaller inverter but a larger motor. The degree of saturation will influence the balance between the motor size and the inverter size [13].

The Energy conversion ratio (Q) can be defined as

$$Q = \frac{converted\ energy}{energy\ supplied} = \frac{W_c}{W_f + W_c} \tag{2.31}$$

and is a kind of generalized power factor which tells how much converted energy ($W_c$) is obtained for a supplied input energy ($W_c + W_f$) in each working stroke. The larger energy conversion ratio results in a decrease of the reactive power, which improves the efficiency of the motor.

The dc link capacitor is directly related to the value of $W_f$, thus in order to achieve a zero ripple voltage, the filter capacitance must be large enough to absorb $W_f$. This requirement may be reduced by overlapping charge/discharge requirements of adjacent phases.

## 2.4   Torque Speed characteristic

The torque-speed operating point of an SRM is essentially programmable, and determined almost entirely by the control. This is one of the features that makes the SRM an attractive solution [12].
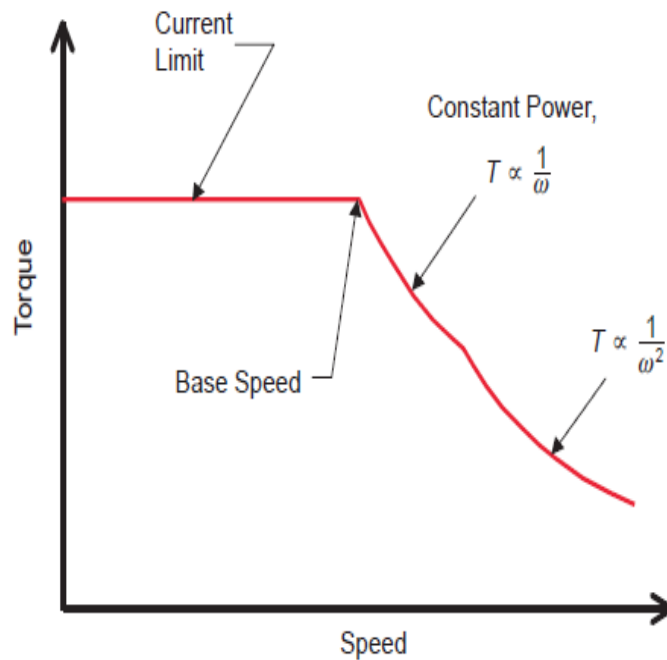


Figure 2.17: Switched Reluctance Motor Torque Speed characteristics [12]

Like all motors, the torque is limited by the maximum allowed current and the speed is limited by bus voltage. The torque-speed plane of a SRM drive can be divided into three regions as shown in Fig 2.17.

In the first region the torque is controlled by the regulation of the current, with relatively minor adjustments to the firing angles.With increasing shaft speed, a current limit region persists until the rotor reaches a speed in which the back-EMF becomes comparable to the DC bus voltage. Given this limitation it is not possible to get more current into the winding, thus no more torque from the motor. At this point, called the base speed, and beyond, the shaft's output power remains constant, and at its maximum. The medium speed range through which constant power operation can be maintained is quite wide and very high maximum speeds can be achieved.

And still, at higher speeds, the back-EMF increases and the shaft output power begins to drop. This region is characterized by the product of torque and the square of speed remaining constant [12] [5] [3].

## 2.5   Conclusion

The relationship of torque with rotor position and stator current was derived for both the ideal linear machine and a real saturating machine. The typical torque speed characteristic of the switched reluctance drive was analysed. Although the switched reluctance machines have been around for some time, only in last decades that real progress has been made and high performance drives are becoming available.

# Chapter 3

# Power supply

## 3.1 Introduction

As discussed earlier, one of the limitations of the SRM drive is its incapability of working directly from the grid. It always needs a certain amount of control and power electronics to function properly. The power converter topology is an important topic, because it determines how the motor can be controlled.

## 3.2 Converter configurations

Considering that the output torque is independent of the direction of current, for certain applications it is possible to use only one switch per phase. In the literature numerous converter topologies have been proposed [2].

One of the advantages of this type of converters (i.e. R-Dump converter in figure 3.1) is the lower number of switches, which imply less gate drivers, reduced area and volume of the heatsink, resulting in greater compactness and lower costs. Nonetheless, they have the problem of being unable to provide zero voltage across the winding during current conduction so the voltage rate of change is doubled [14] [2].
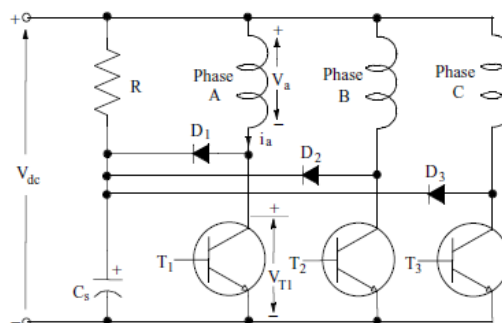


Figure 3.1: R-Dump circuit diagram [2]

21

### 3.2.1   Asymmetric H-bridge

The most popular and also the most flexible configuration for four quadrant operation is the asymmetric H-bridge, shown in figure 3.2. Despite requiring two switches and diodes per phase, it allows independent control of each phase, which is particularly important when phase overlap is desired.
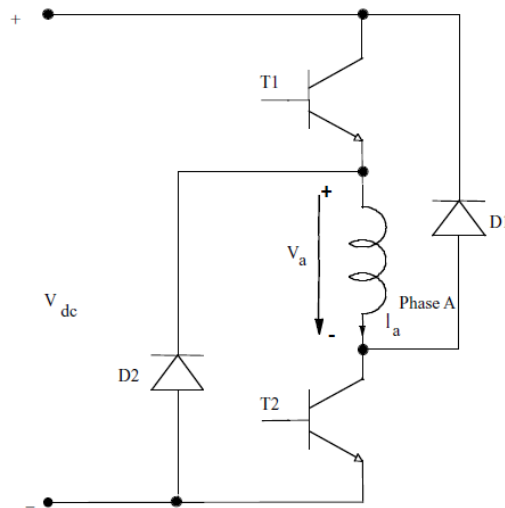


Figure 3.2: Asymmetric H-bridge circuit diagram [2]

Since each phase winding is connected to its own asymmetric H-bridge, in the case of one bridge failure, uninterrupted operation of the motor drive operation is still possible, although with reduced power output. Furthermore, seeing that the phase winding is in series with the switch, it is not possible that a shoot-through fault occurs. The asymmetric H-bridge can apply a three level voltage to the stator winding. It has the capability to provide a positive voltage to increase phase current, negative voltage to decrease the current, and zero voltage to maintain the desired current. These three modes of operation are defined as magnetization, freewheeling and demagnetization mode respectively.

#### 3.2.1.1   Magnetization mode

During the magnetization period, both the switches ($T_1$ and $T_2$) are turned on and the current in the phase winding increases rapidly hence the energy is transferred from the source to the motor, this mode is presented in figure 3.3.
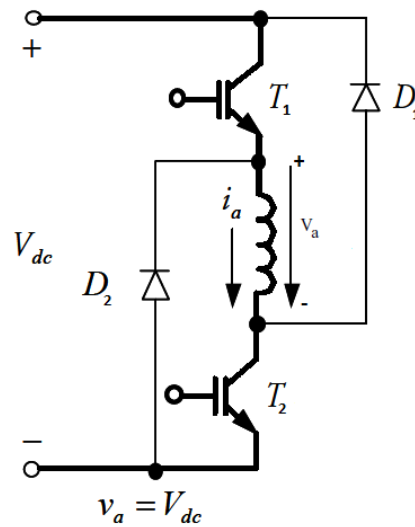
Figure 3.3: Asymmetric H-bridge magnetization mode of operation [14]

### 3.2.1.2 Freewheeling mode

When the conduction interval ends, both switches are turned off. The stored magnetic energy that was not converted to mechanical work is returned to the power supply by the current freewheeling through the diodes. During this time interval in which the diodes ($D_1$ and $D_2$) are forward-biased, the induced voltage across the winding is equal to $-V_{dc}$. When all the stored energy in the inductor is completely returned to the power source (current has returned to zero) the induced voltage collapses to zero too, figure 3.4 illustrates this mode of operation.
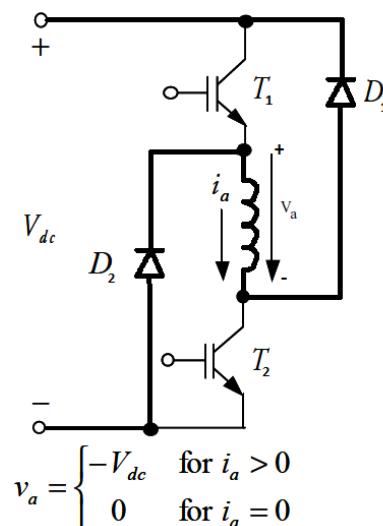


Figure 3.4: Asymetric H-bridge freewheeling mode of operation [14]

### 3.2.1.3   Demagnetization mode

During the demagnetization mode, phase current continues to flow and decay slowly through one switch and one diode, ($T_1$ and $D_1$) or ($T_2$ and $D_2$), and energy is neither taken from nor returned to the DC supply, these two modes are shown in figure 3.5.
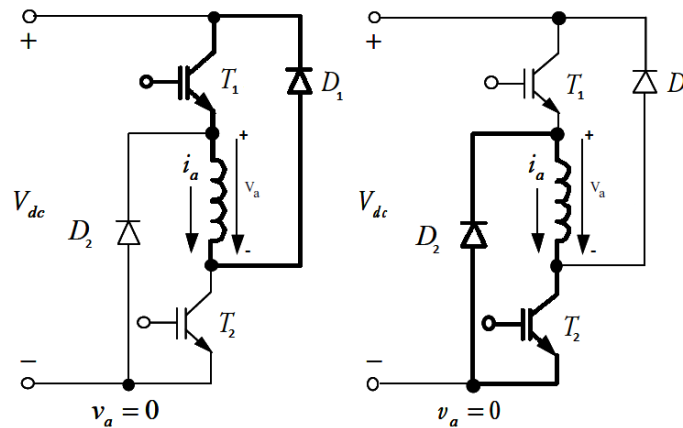


Figure 3.5: Asymetric H-bridge demagnetization mode of operation [14]

## 3.3   Switching strategies

With the asymmetric H-bridge converter, the SRM is usually controlled by either current or voltage.

The main advantage of current control over voltage control is that the output torque can be directly controlled and the reduction of torque ripple or noise is possible. There are two main approaches for controlling the current that is flowing into and out of the winding: bipolar and unipolar.

### 3.3.1   Bipolar

During current control, both switches $T_1$ and $T_2$ are activated simultaneously, thus the voltage across the winding terminals is either $V_{dc}$ or $-V_{dc}$ This switching scheme only uses the first two modes of operation presented in figures 3.3 and 3.4.

The main drawback that this scheme presents is the larger current ripple into the DC link capacitor, which reduces its lifetime. The machine phase winding and the semiconductors experience twice the rate of change of dc link voltage, resulting in a higher deterioration of the insulation, and the rated voltage of the semiconductors has to be essentially doubled which results in higher costs.
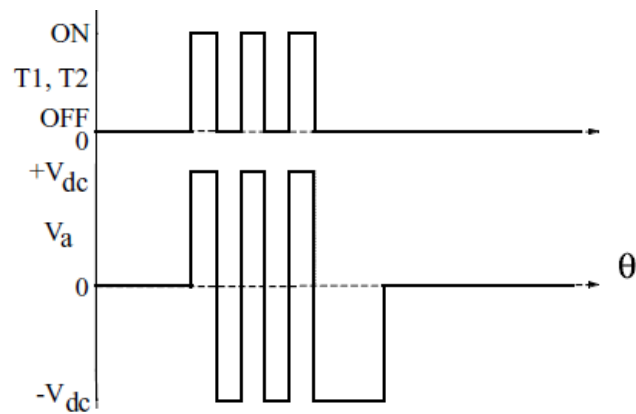
Figure 3.6: Bipolar switching strategy wave forms [2]

### 3.3.2 Unipolar

The second switching scheme allows simultaneous control of the switches only during the commutation of phases and introduces zero voltage loops by introducing the mode of operation presented in figure 3.5. This results in smaller current ripple comparatively with the bipolar switching strategy, because the current does not decrease as rapidly as when the induced voltage was $-V_{dc}$. This switching strategy exploits all the possible modes of operation previously discussed and is ideal for high-performance current and torque control of SRM drive systems.
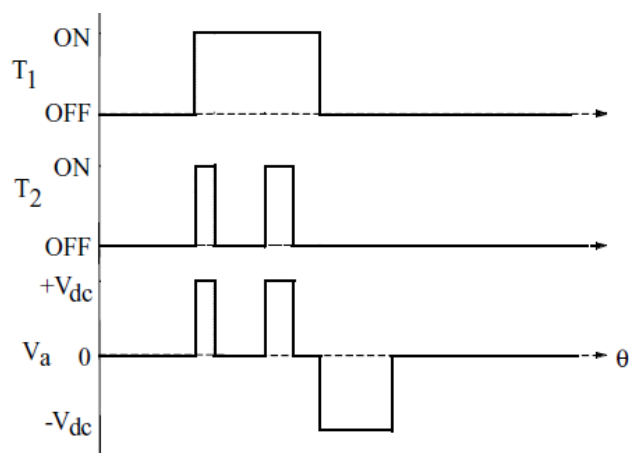


Figure 3.7: Unipolar switching strategy wave forms [2]

## 3.4   Device ratings

Using the unipolar switching strategy, the minimum voltage rating of the power devices is equal to the maximum of the DC link voltage.

Considering that each phase has its own asymmetric H-bridge, and that in each full turn of the rotor that the semiconductors only conduct for a fraction of that turn, which depends on the number of phases the motor has. The current ratings of the switches are equal to or less than $\frac{Maximum\ allowed\ current}{\sqrt{Number\ of\ phases}}$.

For a more thorough analysis, using the unipolar switching strategy, it is possible to have equal ratings for the power devices. This can be accomplished by alternating the diodes, $D_1$ and $D_2$ during the freewheeling mode by turning off $T_1$ and $T_2$ respectively within the switching period as shown in figure 3.8 [2].
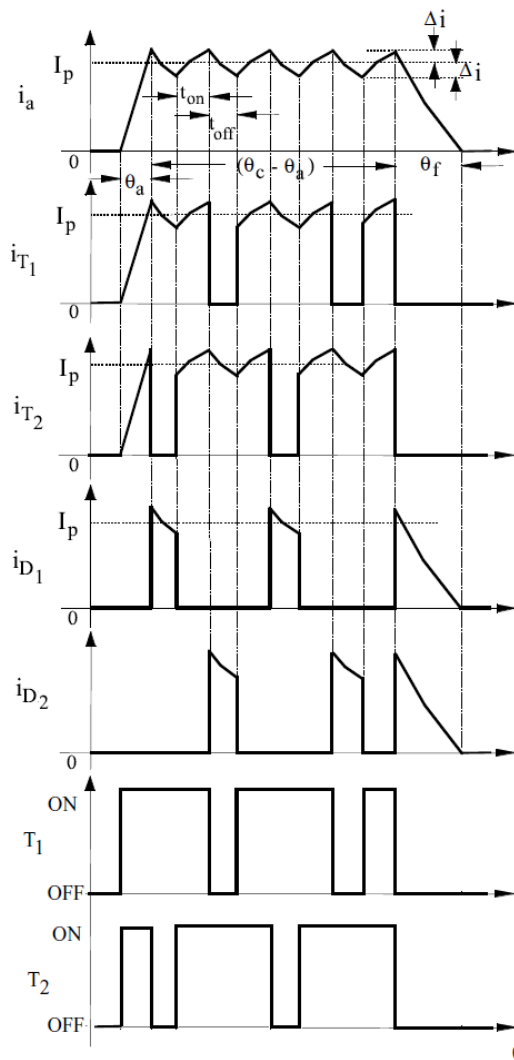
Figure 3.8: Unipolar switching strategy current wave forms [2]

In which $\theta_c$ is the conduction angle, $\theta_a$ advance angle and $\theta_f$ is the current fall angle.

The average duty cycle in the interval ($\theta_c$ - $\theta_a$) is the following

$$D_t \;\; = \;\; \frac{I_p \cdot \left(R_s + \omega_m\right)}{V_{dc}} \tag{3.1}$$

If a current ripple of $2(\Delta i)$ is assumed during the switching period, the power switch rms current is defined as

$$I_T \;\; = \;\; \sqrt{\frac{1}{\tau_r} \cdot \left( (I_p + \Delta i)^2 \cdot \frac{\theta_a}{3} + \left( I_p^2 + \frac{7}{3} \cdot (\Delta i)^2 \right) \cdot \frac{\theta_c - \theta_a}{2} \cdot (1 + D_t) \right)} \;\; [A] \tag{3.2}$$

Where $\tau_r$ is the rotor pole pitch, in other words the conduction angle, which is given by a rotor full turn dividing by the number of rotor poles.

$$\tau_r \;\; = \;\; \frac{2 \cdot \pi}{P_r} \;\; [rad] \tag{3.3}$$

The average diode current can be derived as

$$< I_D > \;\; = \;\; \frac{I_p}{\tau_r} \cdot \left( (1 - D_t) \cdot \frac{\theta_c - \theta_a}{2} + \frac{\theta_f}{2} \right) \;\; [A] \tag{3.4}$$

The converter semiconductors have to be chosen based on the maximum values they may experience. The maximum current rating depends on the maximum allowed voltage and the maximum speed as seen in equation 3.2.

## 3.5 Conclusion

Since the mutual coupling between phases is negligible, each phase is independent and it allows the complete control of the winding for torque generation. Although there is a big number of possible converter configurations, the chapter focused on the asymmetric H-bridge. It is the topology which allows the most flexible control of the winding and also has the capability of fault tolerance in case of winding failure. A comparison between the two possible switching strategies is made and the SRM drive that is being developed will make use of the unipolar switching strategy due to its inherent advantages.

# Chapter 4

# Control of Switched Reluctance Motor Drive

## 4.1 Introduction

The classical approach for torque control is based on the direct current (DC) machine in which torque is proportional to the product of flux and current. Ideally the flux and current are controlled independently. In DC motors this is accomplished by the commutator, and in conventional alternate current (AC) machines it is necessary to resort to the use of mathematical transformations. In either case, torque control is characterized by the concept of vector control, where one component defines the magnetic flux of the motor, and the other, the torque. Unfortunately in SRM there is no equivalent of field-oriented control, the basic principle for continuous torque production is achieved by synchronizing phase currents pulses with rotor position. Since the flux in each phase is built up from zero and returned to zero each stroke, the "armature current" and "field current" are indistinguishable from the actual phase current. [3].

The fact that the machine inductance is not only a function of the rotor position but also the current complicates the development control strategies for SRM drive systems.

For EVs and HEVs applications, the operating points of drive motor change according the driving situation, hence the drive system should have rapid torque response to improve dynamic performance [15].

## 4.2 Control Methods Overview

In order to reduce the torque ripple in SRM drives, different control schemes have been proposed in the literature. These can be divided into two different categories, mechanical or electronic methods. The first category is based on the modification of the constructive design in order to

reduce the inherent torque ripple of the motor. Within the former category, a few methods stand out :

- Rotor skewing

- Pole shaping

- Bifurcated teeth with asymmetric air gap

However the drawback of these approaches is the reduction of the maximum achievable torque due to an increased effective air gap [16].

The second category, which will be the focus os this chapter, includes a larger variety of approaches. The electronic control methods work over a wider operating range. Nonetheless it is necessary to review the torque speed characteristics of the motor as it is important to understand the reason that limits the speed range for some control methods.

At low speed the motor Electromotive Force (EMF) is small when compared to the available supply voltage, and the current can be regulated by chopping. Within this speed range, the current waveform typical shape is shown in figure 4.1.
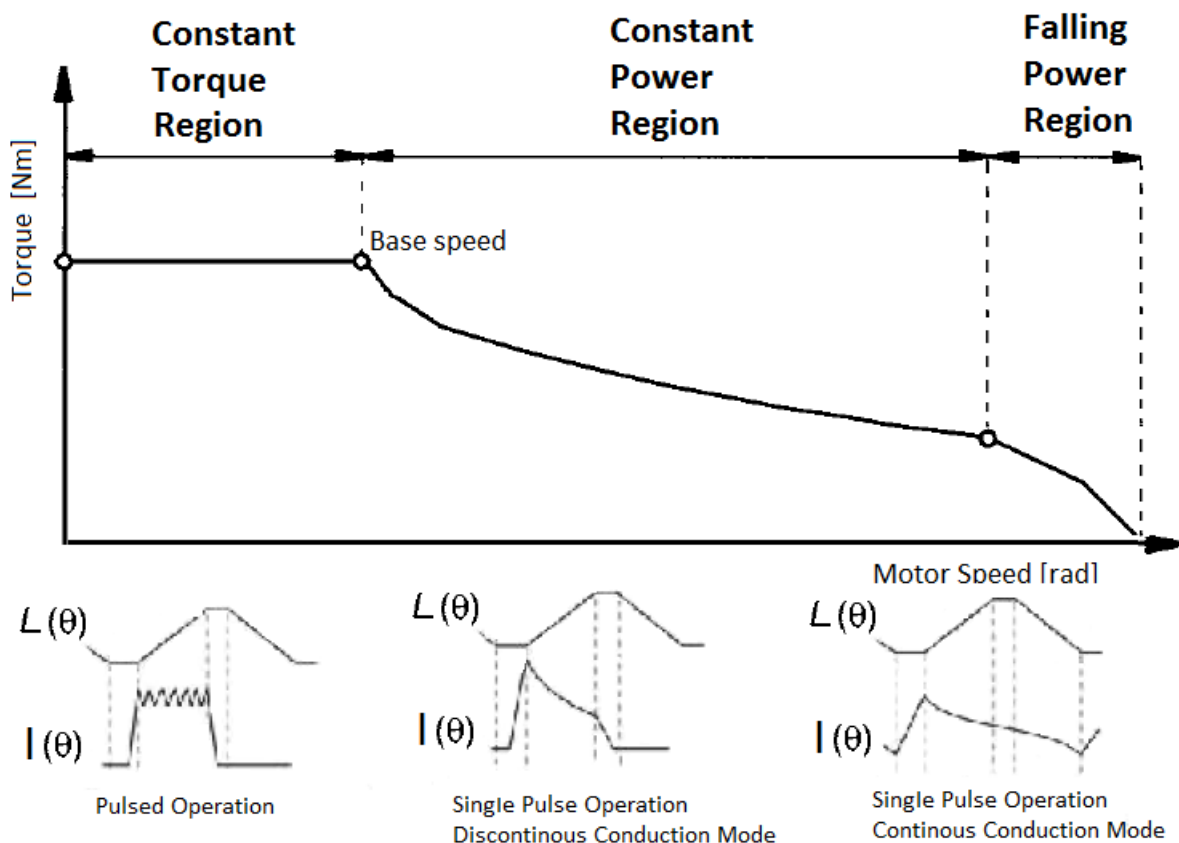


Figure 4.1: Torque speed characteristics with typical current waveforms

As the speed increases, so does the EMF and the available voltage becomes insufficient for chopping. The base speed is the which maximum current and rated torque can be achieved at rated voltage. In the constant torque region, the torque can only be controlled by varying the firing angles of a single pulse of current.

Eventually as even greater velocity's, the turn-on angle can be advanced no more, and the torque falls off more rapidly so that constant power cannot be maintained, If the turn-on angle is advanced beyond the point where the dwell becomes equal to about half the rotor pole-pitch, continuous conduction will begin: the phase current never falls to zero [3]. In this operation region, due to the continued conduction, the magnitude of the current in the phase winding is increased, therefore the power density is also increased [16].

The rise in the conduction period is beneficial because it allows the current to achieve much higher values resulting in higher torques compared to the standard operation mode, because because since never reaches zero it is easier to achieve higher current values during motoring operation. Nonetheless in the continuous conduction mode the machines produces both negative and positive torque because the phase is excited trough the whole conduction period. Consequently the machine efficiency decreases and the torque ripple increases [17].

## 4.3   Firing Angle Control

Appropriate positioning of the phase excitation pulses, relative to the rotor position is the key to obtaining effective performance from an SRM drive system. The Firing Angle (FA) control is the basic approach for controlling average torque at a given speed. The control parameters are the turn-on angle $\theta_{on}$, turn-off angle $\theta_{off}$, and the phase current.

The conduction angle is defined as

$$\theta_{dwell} \quad = \quad \theta_{off} - \theta_{on} \quad [rad] \tag{4.1}$$
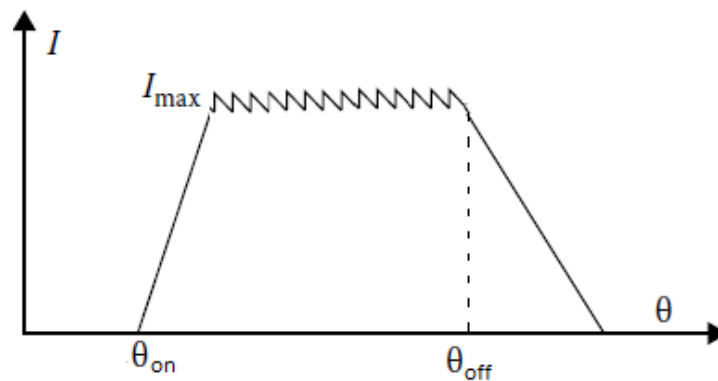


Figure 4.2: Typical current pulse at low speeds [4]

Within each electrical cycle, every phase is excited only once. To guarantee the production of continuous torque, it is necessary that the desired current arrives in the interval in which the inductance is rising.

Seeing that the stator is composed by a resistor inductor (RL), the current cannot rise or fall instantly. It becomes imperative to excite the phase in advance in order to achieve the necessary current in time. Similarly, this needs to be done for the turn-off angle, so that the current reaches zero before the negative inductance slope is met.
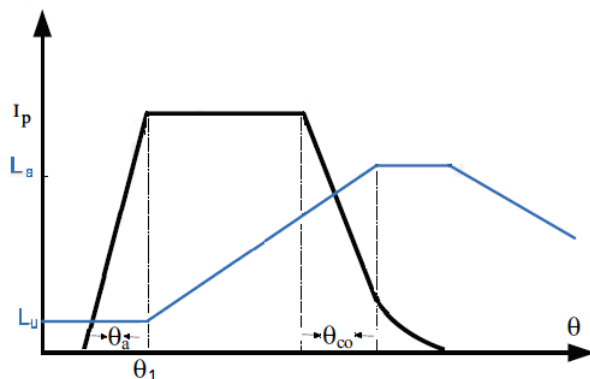


Figure 4.3: Angle control

In the figure 4.3, $\theta_a$ stands for advance angle, and $\theta_{co}$ the cut-off angle, these are dependent on the rotor speed, and the desired peak current. As the speed increases, phase advancing is necessary to achieve the desired current while the rotor and stator overlap.

### 4.3.1   Turn-on angle calculation

Ideally, the turn-on angle is advanced so that the reference current level $I_{ref}$ is reached just as the inductance slope changes from zero to positive, defined as $\theta_1$ [18].

As the rotor speed increases, so does the advance angle, with its maximum being at the beginning of the minimum inductance region, so as not to produce negative torque.

$$\theta_{on} \quad = \quad \theta_1 - L_u \cdot \omega_m \cdot \frac{I_{ref}}{V_{dc}} \quad [rad] \tag{4.2}$$

### 4.3.2   Turn-off angle calculation

When the phase winding is turned on, the phase voltage is positive and the flux-linkage starts to rise from zero, reaching its peak at $\theta_{off}$ [19]. When the phase winding is turned off, the phase voltage is negative and the flux starts to decrease, eventually returning to zero.

$$(U_{ph} - I_{ph} \cdot R_{ph}) \cdot t_{up} + (-U_{ph} - I_{ph} \cdot R_{ph}) \cdot t_{down} \quad = \quad 0 \quad [V \cdot s] \tag{4.3}$$

Where $t_{up}$ is the flux-linkage's rising time and $t_{down}$ the falling time.

$$t_{up} \quad = \quad \frac{\theta_{off} - \theta_{on}}{\omega} \quad [rad] \tag{4.4}$$

$$t_{down} \quad = \quad \frac{\theta_z - \theta_{off}}{\omega} \quad [rad] \tag{4.5}$$

Where $\theta_z$ represents the position where the phase current reaches zero.
Assuming

$$I_{ph} \cdot R_{ph} \quad << \quad V_s \quad [V] \tag{4.6}$$

The term $I_{ph} \cdot R_{ph}$ can be ommited. Replacing 4.3, 4.4 and 4.5 into 4.6 results in

$$\frac{\theta_{off} - \theta_{on}}{\omega} \cdot U_{ph} \quad = \quad \frac{\theta_z - \theta_{off}}{\omega} U_{ph} \quad [V \cdot s] \tag{4.7}$$

Resulting in

$$\theta_{off} \quad = \quad \frac{\theta_z + \theta_{on}}{2} \quad [rad] \tag{4.8}$$

## 4.4   Average Torque Control

For applications where the torque ripple is not a concern, the Average Torque Control (ATC) method can be employed. This approach offers some advantages when compared to the classical direct torque control strategies. In those schemes, the phase current is regulated at each sample time according to the torque command and rotor position, while ATC keeps phase current constant over one excitation period, thus for ATC there is no need to high resolution rotor position sensor, only discrete position sensors to detect maximum and minimum inductance areas [15]. Since current chopping can only be used when the motor speeds is below the base speed, the usual direct torque control methods can only be employed for limited speed ranges, whereas ATC is applicable of the whole speed range.

For ATC, the main control variables are the reference current $i_{ref}$, turn-on angle $\theta_{on}$ and turn-off angle $\theta_{off}$.

As stated in chapter 2, the electromagnetic torque can be expressed in terms of co-energy.

$$T_e \quad = \quad \frac{\partial W_c}{\partial \theta} \bigg|_{I_{ph}=const} \quad [Nm] \tag{4.9}$$

One cycle of the loop represented in figure 4.4 is called a stroke. The number of strokes per revolution for a given SRM depends on the number of phases ($N_{ph}$) and the number of rotor poles ($N_r$).
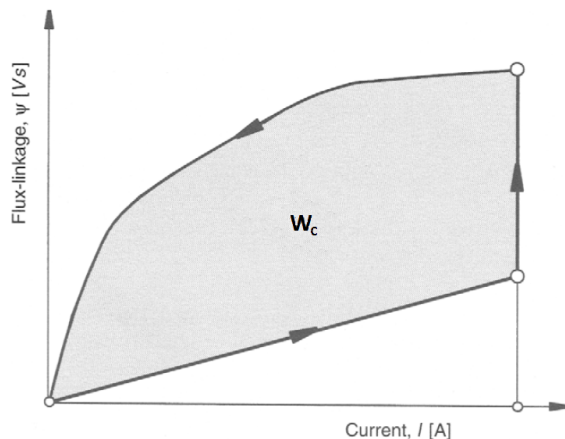


Figure 4.4: Typical $\psi$-I excitation period [3]

Therefore the average electromagnetic torque in Nm is

$$T_{e\ [avg]} \quad = \quad \frac{N_{ph} \cdot N_r}{2 \cdot \pi} \cdot W_c \quad [Nm] \tag{4.10}$$
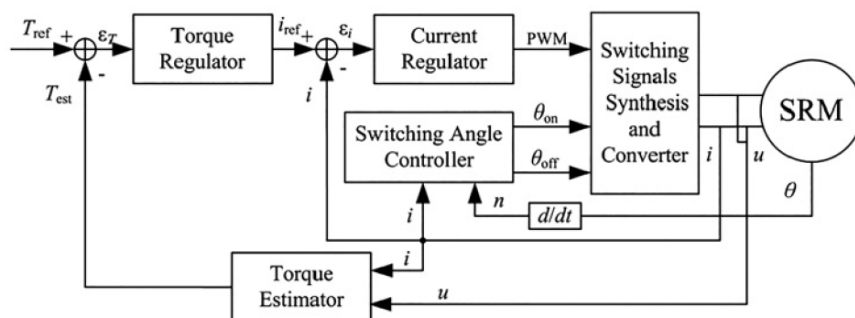


Figure 4.5: Block diagram of a closed-loop average torque control [15]

This type of control that only regulates average output torque is not effective for high performance operation. In order to obtain good transient performance, it is necessary to employ instantaneous torque control.

## 4.5   Direct Instantaneous Torque Control

Direct instantaneous torque control, also know as DITC, is a method that consists essentially on two components, torque estimator and torque hysteresis controller.

For a given measured rotor position and current, the instantaneous torque of the motor can be found from the look-up table derived from the measured motor torque or by finite-element simulations. Once the phase torques are found, the total motor torque can be found by addition.
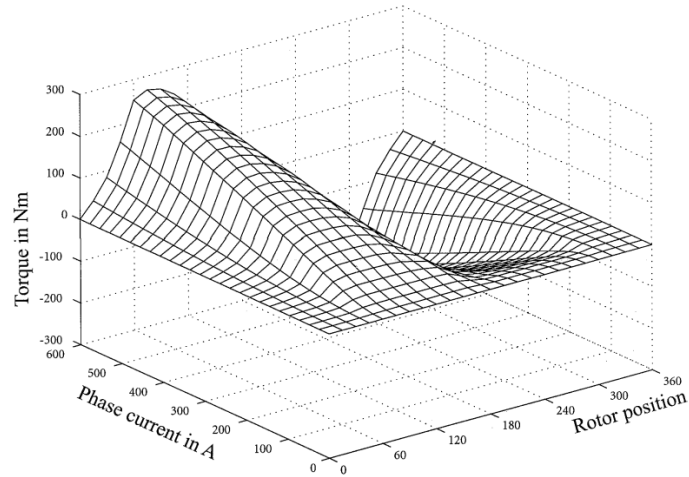


Figure 4.6: Static torque versus current and rotor position of a single phase SRM [20]

Depending on the deviation of the instantaneous torque from the reference torque, a negative, zero, or positive voltage level is applied to the phase terminals, as the hysteresis controller tries to balance the torque produced in each phase in attempt to maintain the produced torque constant [20] [21].
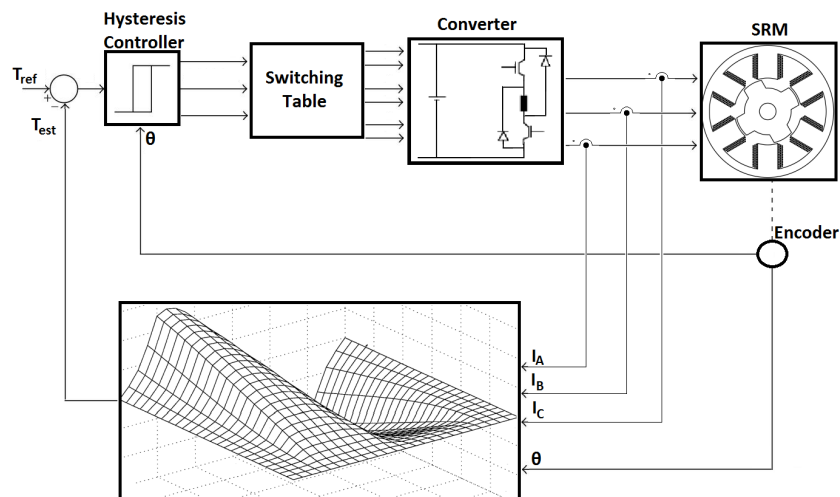


Figure 4.7: Control Diagram of DITC

The advantages of this method are its high robustness and fast torque response.

## 4.6   Advanced Direct Instantaneous Torque Control

For certain applications, when the torque ripple is a critical issue, more developed torque control strategies are required.

Ideally torque control would be achieved by the use of a current source, however these are more difficult and expensive to realise. So in order to produce similar current shapes with a voltage source it is necessary to regulate the applied voltage. This is normally accomplished with pulse width modulation (PWM) techniques. Advanced direct instantaneous torque control, ADIC, combines the conventional DITC and PWM method, however in DITC due to its typical hysteresis control, the switching frequency is not constant. The ADTIC allows the reduction of the torque ripple and the switching frequency becomes constant, which simplifies the design of input power filter [22].

The average voltage of each phase winding can be adjusted from 0 to $V_{dc}$ in one sampling time. The duty cycle of the phase switch is regulated according to the torque error and simple control rules of DITC [23].

$$D_t \quad = \quad \frac{|T_{err}|}{\Delta T_H} \tag{4.11}$$

Where, $T_{err}$ is torque error, $\Delta T_H$ is torque error boundary, and $D_t$ the duty cycle.

Considering that the ADITC is just an extension of the existing DITC, its control diagram, illustrated in figure 4.8 is very similar to the one presented in Figure 4.7.
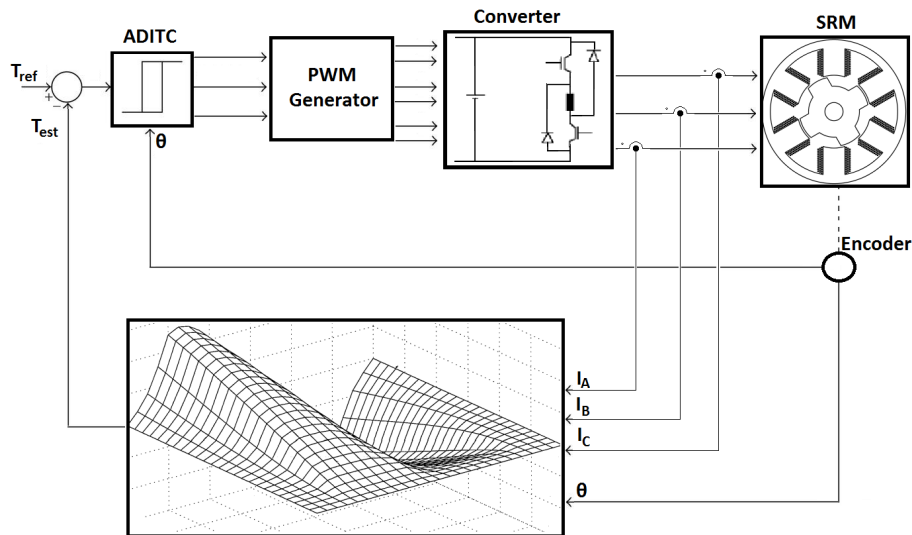


Figure 4.8: Control Diagram of ADITC

## 4.7  Predictive PWM-based Direct Instantaneous Torque Control

As stated earlier, torque control is performed using voltage source converters, normally the controlled variable is the phase current, although that is achieved by controlling the voltage and therefore the flux-linkage. Thus the directly controlled machine variable is flux-linkage rather than current. [24].

Flux linkage values are usually obtained trough lookup tables, such as the one presented in figure 4.9.
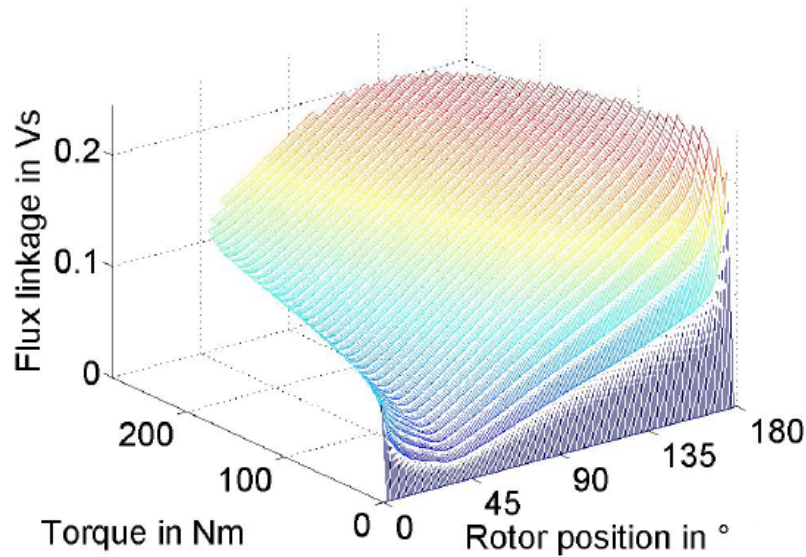


Figure 4.9: Flux linkage as a function of torque and rotor position [25]

In every iteration, with a simple extrapolation of the next rotor position, the necessary flux-linkage for a given torque can be obtained.

Over one sampling period, the rotor position is predicted by making use of the next expression

$$\theta_{predicted} \quad = \quad \theta + \omega_m \cdot T_S \quad [°] \tag{4.12}$$

Where, $\theta_{predicted}$ is the extrapolated rotor position, $\theta$ the present rotor position, $\omega_m$ the machine angular speed and $T_S$ the sampling time.

Together with the reference torque, the desired flux-linkage can be obtained from the above mentioned table which can be used as a function of predicted position [25].

$$\psi^* \quad = \quad F(\theta_{predicted}) \quad [V \cdot s] \tag{4.13}$$

The machine phase flux-linkage can be estimated directly from integration of the terminal voltage, or indirectly from phase current and machine characteristics.

The difference between reference and current flux-linkage is given by

$$\Delta \psi \;\; = \;\; \psi^* - \psi \quad [V \cdot s] \tag{4.14}$$

Knowing the necessary variation in flux necessary to achieve the desired torque, the required output voltage can be calculated as

$$V_{ph}^* \;\; = \;\; \frac{\Delta \psi}{T_S} \quad [V] \tag{4.15}$$

Making use of pulse width modulation, it is possible to reach any voltage within the interval $-V_{dc}$ and $+V_{dc}$. Neglecting voltage drops across the resistance and semiconductors, the duty cycle can be computed as

$$D_t \;\; = \;\; \frac{V_{ph}^*}{V_{dc}} \tag{4.16}$$

For a more precise calculation, these drops must be considered. The typical control diagram for this method is shown in figure 4.10
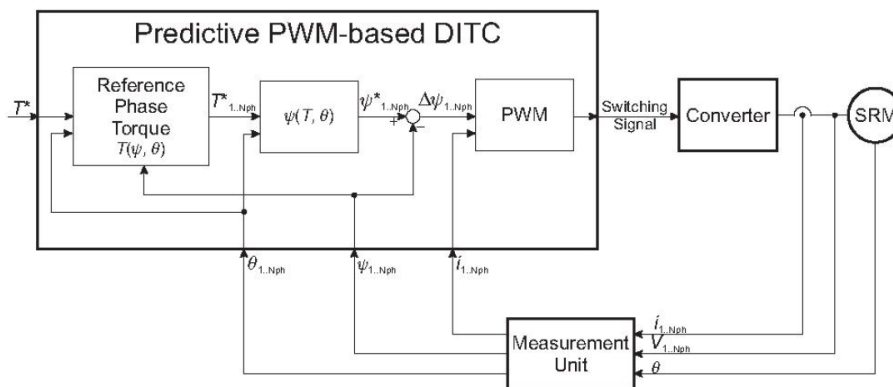


Figure 4.10: Control Diagram Predictive PWM-based DITC [25]

Since every phase has its own torque estimation, during phase changes, it is possible to create separate torque commands, and the sum of all torque commands equals the reference torque. [25]

## 4.8   Torque sharing control

Another effective control method for torque ripple minimization and losses in SRMs at low speed is Torque Sharing Function (TSF) control and current profiling control. The approach relies essen-

tially on tracking the instantaneous torque in every individual phase trough suitable torque sharing functions.

$$T_e = T_x + T_y \tag{4.17}$$

Where $T_x$ and $T_y$ stands for the torque produced by phase x and y respectively and these are dependent on the current rotor position.

$$T_x = T_e \cdot f_x(\theta) \tag{4.18}$$

$$T_y = T_e \cdot f_y(\theta) \tag{4.19}$$

And then the choice of the reference angles depends on the inductance profile of a specific motor. The typical torque control diagram using TSF is depicted in figure 4.11. Conventionally almost all TSF schemes use the DITC torque control.
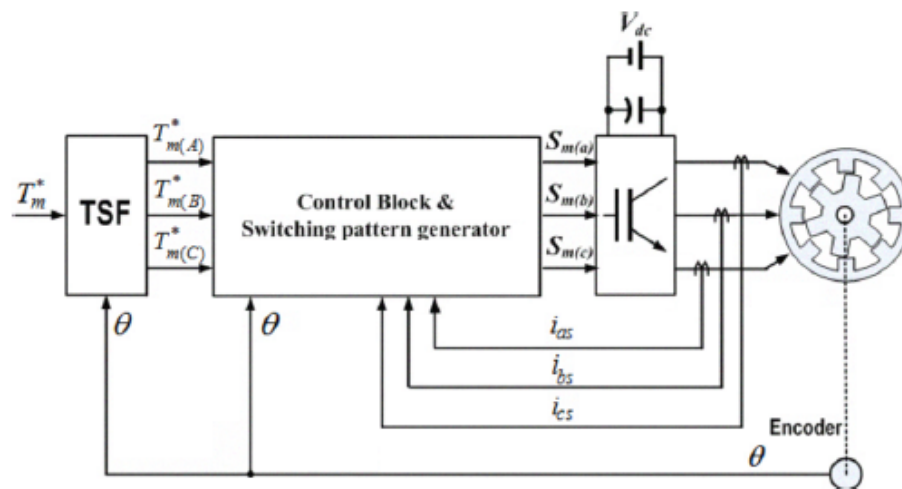


Figure 4.11: Torque control block diagram with TSF method [26]

There are a total of four different kinds of TSFs proposed in the literature, they can be classified as linear [27], exponential [28], sinusoidal [29] and cubic [30].The name indicates the type of variation of the TSFs (as function of the rotor position) during the commutation intervals [31].

The TSFs are dependent on the turn on angle, overlap angle, turn off angle and expected torque [32]. The reference phase torque $T_K^*$ can be defined as

$$
T_k(\theta) = \begin{cases}
0, & 0 \leq \theta \leq \theta_{on} \\
T^* \cdot f_{rise}(\theta), & \theta_{on} \leq \theta \leq \theta_{on} + \theta_{ov} \\
T^*, & \theta_{on} + \theta_{ov} \leq \theta \leq \theta_{off} - \theta_{ov} \\
T^* \cdot f_{fall}(\theta), & \theta_{off} - \theta_{ov} \leq \theta \leq \theta_{off} \\
0, & \theta_{off} \leq \theta \leq \theta_p
\end{cases}
\tag{4.20}
$$

The phase k is energized between turn-on $\theta_{on}$ and turn-off $\theta_{off}$ angles, the overlap angle $\theta_{ov}$ denotes intervals when phase k shares torque with outgoing phase (k-1) or with incoming phase (k+1). The rotor period is defined as $\theta_p$, and the rising and falling of phase torques during commutation are represented by the functions $f_{rise}$ and $f_{fall}$. These are dependent on the type of torque sharing function [31].

For the following TSFs, the $f_{fall}$ can be defined as a function of $f_{rise}$

$$
f_{fall}(\theta) \;=\; 1 - f_{rise}(\theta + \theta_{ov} - \theta_{off} + \theta_{on})
\tag{4.21}
$$

### 4.8.1   Linear

The linear TSF is the simplest, however it does not consider the non-linear characteristics of the motor. Therefore, the actual torque error is increased around the start and end of the commutation region due to the higher non-linear characteristics [26].

During commutation region, the linear TSF has constant slope of torque, and is defined as

$$
f_{rise}(\theta) \;=\; \frac{\theta - \theta_{on}}{\theta_{ov}}
\tag{4.22}
$$
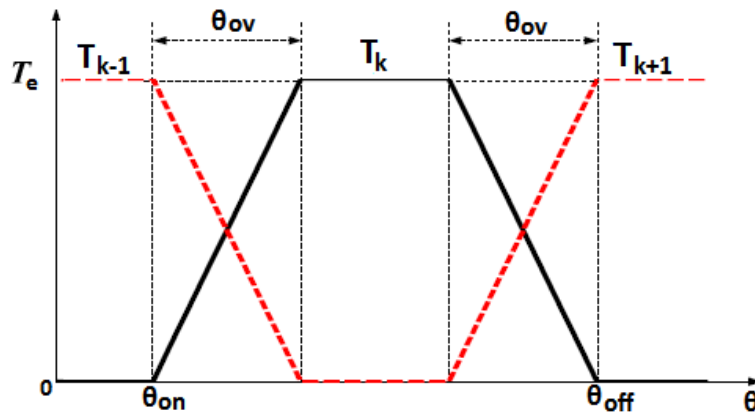


Figure 4.12: Typical torque profile obtained with linear TSF [31]

### 4.8.2 Exponential

In the case of exponential TSF, the $f_{rise}$ is defined as

$$f_{rise}(\theta) \quad = \quad 1 - exp\left(\frac{-(\theta - \theta_{on})^2}{\theta_{ov}}\right) \tag{4.23}$$
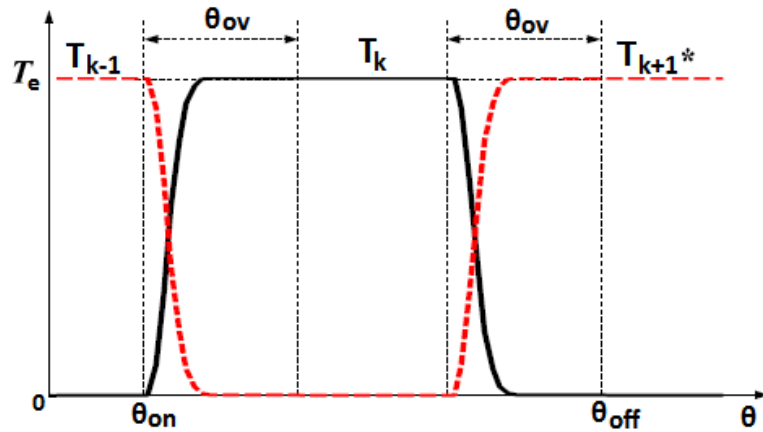


Figure 4.13: Typical torque profile obtained with exponential TSF [31]

### 4.8.3 Sinusoidal

For the sinusoidal TSF, the $f_{rise}$ given by

$$f_{rise}(\theta) \quad = \quad \left[sin\left(\frac{\pi}{2} \cdot \frac{\theta - \theta_{on}}{\theta_{ov}}\right)\right]^2 \tag{4.24}$$
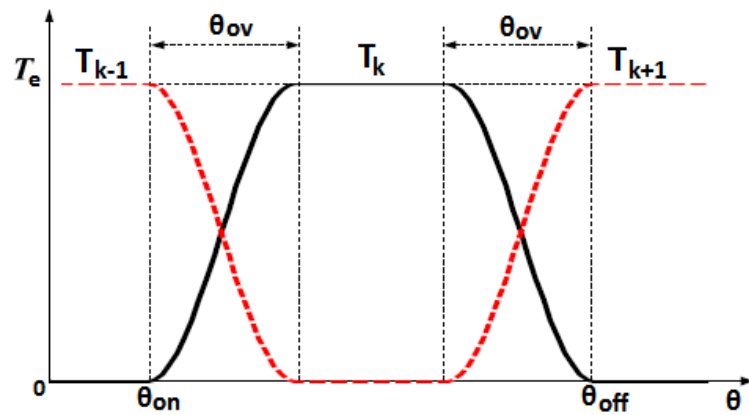


Figure 4.14: Typical torque profile obtained with sinusoidal TSF [31]

### 4.8.4 Cubic

The cubic $f_{rise}$ function is expressed as

$$f_{rise}(\theta) \quad = \quad \frac{3 \cdot (\theta - \theta_{on})^2}{\theta_{ov}^2} - \frac{2 \cdot (\theta - \theta_{on})^3}{\theta_{ov}^3} \qquad (4.25)$$
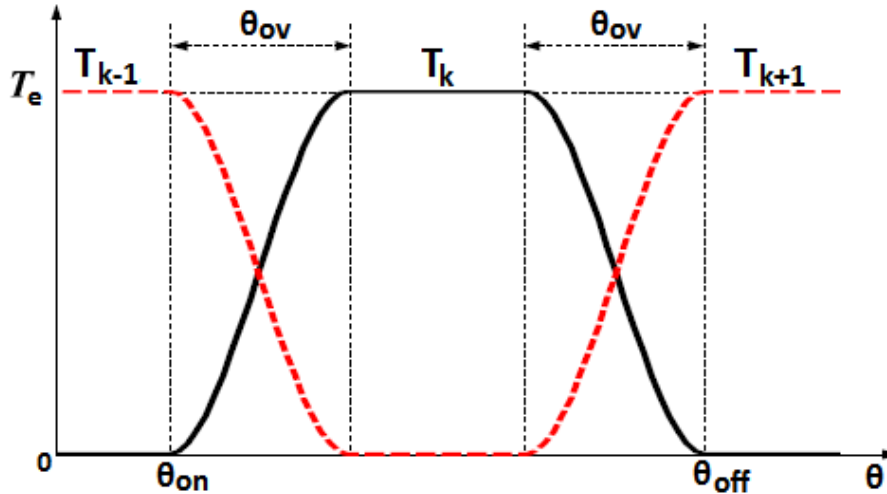


Figure 4.15: Typical torque profile obtained with cubic TSF [31]

Most of the proposed torque-sharing functions only have a primary goal which is the reduction of torque ripple, however it is possible to have several objectives. For example there is yet another TSF, that is basically an extension of the cubic one, named piecewise cubic TSF [33], that provides the lowest copper losses as well as an extension of torque-speed region in which smooth torque can be produced [31]. However it increases the complexity of the optimization problem and the computational time.

## 4.9 Conclusion

The dynamics of the SRM are non linear as is evident from the system equations described in Chapter 2, making an accurate torque control difficult. The methods for average torque control need lower resolution position sensors and are less computationally intensive, which implies a cheaper controller. A thorough review on the control schemes was made and unlike other types of machines, the controller has to be specifically programmed for a particular motor, even if the voltage and current ratings are matched [3]. To extend the machine operating speed range, different modes should be adopted according to different speed ranges [15].

[34]

# Chapter 5

# Motor Design

## 5.1 Introduction

The final goal of the dissertation was to have a SRM drive capable of traction for the electric vehicle competition *Veículo Elétrico de Competição (VEC)*. At the beginning of the thesis it was decided that it was necessary to design and build a Switched Reluctance Motor in order to reach that goal.

Within the following chapter, a synthesis of motor design procedures is made. Starting from the basic motor requirements, such as output power and rated speed, up until the machine construction parameters like its length or number of phases. During the chapter a general review of electric machines magnetic steel and power losses is made. Finally the machine dynamic behaviour is simulated by making use of ansoft maxwell as a simulation tool.

## 5.2 Design Procedure

The design of electric machines is a complex task and requires a lot of expertise in order to achieve good results. Seeing that the machine performance depends on various parameters which interact with each other. The so called optimal design, is nothing more than than a trade off or compromise of certain aspects. For example, in order to increase the efficiency one can resort to superior quality steel, however it comes at the expense of increased price.

An overview of the typical design steps taken during the design of switched reluctance machine is depicted in the flow chart present in figure 5.1.

The designer's goal is the determination of the main parameters of the electric and geometric parts that integrate the motor in a way that meets the required specifications.

The actual machine design is an iterative modification of geometry, winding and material. Some parameters are narrowed down by the application itself, for instance in high-speed applications which are not sensitive to torque ripple, single phase machines are preferred.
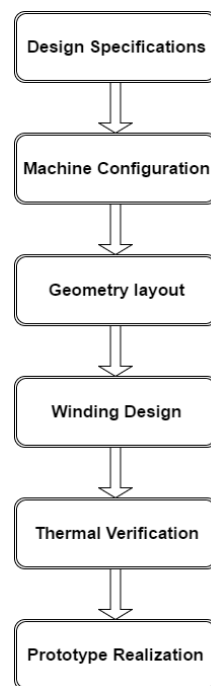
Figure 5.1: Typical steps in the design process SRM

## 5.3    Motor Requirements

An efficient electrical motor should be able to provide constant torque under the base speed and be able to to operate at constant power over a wide speed range. Ideally an electrical vehicle power plant should have a constant power output across the entire operating range. However in order not to exceed the adhesion limit between the tire-ground contact area, at low speeds the motor torque is forced to maintain a constant value [36].
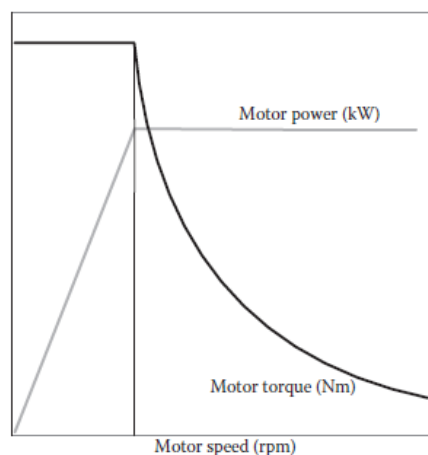


Figure 5.2: Ideal performance characteristics for vehicular power plants [36]

The torque/speed profile of the SRM looks similar to the ideal traction characteristics presented in figure 5.2.

Considering that the motor is to be used in a real car, there are some requirements that it must be capable of achieving, such as the ability to perform regenerative breaking, as well as the capability of spinning in either direction. In other words the motor must be capable of producing positive or negative torque, independently of the direction it is rotating, this is usually referred as four-quadrant operation.
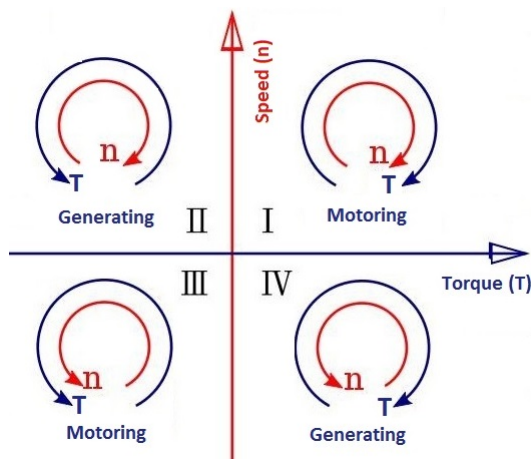


Figure 5.3: Electric motor four quadrant operation

The main design specifications for the motor are its rated output power $P_n$ and rated speed $n_n$. Currently, the *VEC* is installed with a permanent magnet synchronous motor, *EMRAX 207*, that is capable of achieving 40 kW of continuous power and 80 kW of peak power. The plan is to upgrade it with an *EMRAX 228*, that is capable of 55 kW continuous power and 100kW peak power. In order to properly compare the performance of the two motors in the car, the following specifications were decided.

Table 5.1: Dimensions of the proposed Switched Reluctance Motor

| Parameter | Symbol | Value | Units |
|---|---|---|---|
| Rated output Power | $P_n$ | 60000 | W |
| Rated Speed | $n_n$ | 2500 | RPM |
| DC link voltage | $V_{dc}$ | 600 | V |

Knowing the rated speed and output power will automatically fix the rated torque $T_n$ that motor has to develop.

$$T_n \quad = \quad \frac{P_n}{2 \cdot \pi \cdot n_n} \quad [N \cdot m] \tag{5.1}$$

However, by themselves, these specifications are not sufficient to determine unambiguously and quantitatively all the various motor parameters. Criteria like continuous power, peak torque, maximum machine length and outer diameter specifications must be provided [17][11].

Torque ripple should be as low as possible. Reducing torque tipple to imperceptible levels is critical in electrically assisted steering applications, because handwheel torque variation is extremely objectionable and detectable by most drivers in the population. [3]

The machine is to be manufactured and assembled by the company *WEG*, consequently some constraints were imposed, namely the stator outer diameter and the shaft diameter.

Table 5.2: Dimensions of the proposed Switched Reluctance Motor

| Parameter | Symbol | Value | Units |
|---|---|---|---|
| Stator outer diameter | $Ds_o$ | 0.380 | m |
| Shaft diameter | $d_{sh}$ | 0.085 | m |

With the mentioned specifications it is possible to start the preliminary machine design.

## 5.4   Machine Configuration

There are many possible stator rotor configurations, and machines with the same number of phases, can differ in their geometrical structure, for example the 8/4 two phase, $N_{ph} = 2$ , motor is effectively a 4/2 motor with a multiplicity of two, $M = 2$.

Figure 5.4 presents a set of possible machine configurations.

Where $N_s$ stands for stator poles, $N_r$ rotor poles, $\varepsilon^{\circ}$ is the step angle and S represents the number of energy conversion loops in one motor revolution.

$$S = N_{ph} \cdot N_r \tag{5.2}$$

$$\varepsilon^{\circ} = \frac{360}{N_{ph} \cdot N_r} \quad [^{\circ}] \tag{5.3}$$

Ideally double the number of repetitions on the stator poles (while other parameters are held constant with all the coils of each phase connected in series) does not affect the maximum or minimum inductance, but doubles the angular rate of change of phase flux, resulting in doubled torque at a given speed. However when taking into account the saturation behaviour, increase in iron losses, available coil area and the variation in the magnetic circuit due to the increase of the repetition modifies this simplistic conclusion [37].

With such a large variety of viable configurations it is necessary to weigh the pros and cons of increased number of phases and multiplicity in order to get the design that best fits the application in question.

| $N_{PH}$ | $N_s$ | $N_r$ | M | $\varepsilon^o$ | S |
|---|---|---|---|---|---|
| 2 | 4 | 2 | 1 | 90.00 | 4 |
| 2 | 8 | 4 | 2 | 45.00 | 8 |
| 2 | 4 | 6 | 1 | 30.00 | 12 |
| 2 | 8 | 12 | 2 | 15.00 | 24 |
| 2 | 12 | 18 | 3 | 10.00 | 36 |
| 2 | 16 | 24 | 4 | 7.50 | 48 |

| $N_{PH}$ | $N_s$ | $N_r$ | M | $\varepsilon^o$ | S |
|---|---|---|---|---|---|
| 3 | 6 | 2 | 1 | 60.00 | 6 |
| 3 | 6 | 4 | 1 | 30.00 | 12 |
| 3 | 6 | 8 | 1 | 15.00 | 24 |
| 3 | 12 | 8 | 2 | 15.00 | 24 |
| 3 | 18 | 12 | 3 | 10.00 | 36 |
| 3 | 24 | 16 | 4 | 7.50 | 48 |

| $N_{PH}$ | $N_s$ | $N_r$ | M | $\varepsilon^o$ | S |
|---|---|---|---|---|---|
| 4 | 8 | 6 | 1 | 15.00 | 24 |
| 4 | 16 | 12 | 2 | 7.50 | 48 |
| 4 | 24 | 18 | 3 | 5.00 | 72 |
| 4 | 32 | 24 | 4 | 3.75 | 96 |
| 4 | 8 | 10 | 1 | 9.00 | 40 |

| $N_{PH}$ | $N_s$ | $N_r$ | M | $\varepsilon^o$ | S |
|---|---|---|---|---|---|
| 5 | 10 | 4 | 1 | 20.00 | 18 |
| 5 | 10 | 6 | 1 | 12.00 | 30 |
| 5 | 10 | 8 | 1 | 9.00 | 40 |
| 5 | 10 | 12 | 1 | 6.00 | 60 |

| $N_{PH}$ | $N_s$ | $N_r$ | M | $\varepsilon^o$ | S |
|---|---|---|---|---|---|
| 6 | 12 | 10 | 1 | 6.00 | 10 |
| 6 | 24 | 20 | 2 | 3.00 | 120 |
| 6 | 12 | 14 | 1 | 4.29 | 84 |

| $N_{PH}$ | $N_s$ | $N_r$ | M | $\varepsilon^o$ | S |
|---|---|---|---|---|---|
| 7 | 14 | 10 | 1 | 5.14 | 70 |
| 7 | 14 | 12 | 1 | 4.29 | 84 |

Figure 5.4: Examples of valid stator/rotor pole number combinations (preferred combinations are not shaded) [3]

## 5.4.1 Number of phases

With the machine requirements known, it is possible to start to delimit some of its parameters such as its number of phases.

Since the motor needs to have self starting capability, single phase machines are not desirable, because if the rotor and stator poles are aligned it does not possess the ability to self start, although this problem can be solved with permanent magnet on the stator at intermediate positions, the average torque is diminished.

One of the main requirements for the motor is its ability to perform four-quadrant operation, therefore a minimum of three phases are needed to fulfil this condition.

As the number of phases of the motor rises, so does its power density and reliability, considering that with a higher number of phases, if there is a failure the motor is still be able to run. However it is not without its disadvantages, a higher number of phases requires a corresponding number of converter phase units and their respective drivers.

## 5.4.2 Pole selection

The choice of number of stator slots and rotor poles depend on the application. It is preferred to have the ratio between stator and rotor poles to be a non-integer, even though some integer values

have been attempted [2].

Usually the number of stator poles exceed the number of rotor poles, this is beneficial because switched reluctance motors make use of the *"vernier"* principle common in stepper motors, in which an internal torque multiplication is achieved with a rotor speed slower than that of the rotating field machine. Without this multiplication, the torque per unit volume would be lower than that of the induction machine, nonetheless the price is paid by a substantial increase in commutation frequency, which means higher core losses and converter losses [6].

For the application in question the following combinations were considered.

|                    | Poles |    |   |    |    |    |
| ------------------ | :---: | :-: | :-: | :-: | :-: | :-: |
| Stator poles $N_s$ | 6 | 12 | 8 | 16 | 10 | 12 |
| Rotor poles $N_r$  | 4 | 8  | 6 | 12 | 8  | 10 |
| Phases $N_{ph}$    | 3 | 3  | 4 | 4  | 5  | 6  |
| Multiplicity M     | 1 | 2  | 1 | 2  | 1  | 1  |

Table 5.3: Machine configurations considered

If the maximum speed of the machine is $\omega_m$, then the stator frequency for phase is given by

$$ f_s \quad = \quad \frac{\omega_m}{2 \cdot \pi} \cdot N_r \quad [Hz] \tag{5.4} $$

From the equation 5.4 it is obvious that an increase in the number of rotor poles implies an increase in the stator frequency in proportion,

The increase in the number of rotor poles ($N_r$) results in a reduction of aligned flux, which consequently allows the reduction in size of different parts of the motor, making it more compact [38]. However there is an increase in iron losses, for low speed application these are not significant but in the case of an electric car high speed operation is required.

As the number of rotor poles increase the energy conversion ratio (Q) decreases, hence the converter volt - ampere rating increases [3].

The two main weaknesses of the switched reluctance machine are its torque ripple and acoustic noise, but these can be reduced depending on the machine configuration and control method.

The advantage of the larger Nr is a smaller step angle which leads to a lower torque ripple.

One of the causes of acoustic noise are the radial forces in SRM, and as the number of rotor poles increase, these forces decrease, therefore lowering the noise of the machine.

Weighing all of the above, it was decided to use 12/8 configuration for the motor, which is also one of the most popular configurations for three-phase machines.

## 5.5   Output torque equation

With the basic configuration defined, in order to determine the geometrical dimensions, it is necessary to have a relationship between motor characteristics and output power. For electrical machines e.g. induction machine and synchronous machine, the preliminary machine dimension for a specified torque is conventionally determined using the well know torque output equation present in equation 5.5 [2].w

$$T_e \;=\; K_o \cdot Ds_i^2 \cdot L_{fe} \quad [N \cdot m] \tag{5.5}$$

Where $K_o$ is the output coefficient, $Ds_i^2$ the stator inner diameter and $L_{fe}$ is the stator core length. The range of the output coefficient is very wide (2.7 - 30 $[k \cdot N \cdot m/m^3]$ ), and depends on the machine dimension, application and cooling system, thus the estimated torque output could be inaccurate if a wrong $K_o$ is chosen.

For a conventional SRM, the typical and basic method of deriving the output power has been well covered in the literature [2] [39].

For a flat topped shaped current, I , neglecting the resistive voltage drop, the flux-linkage voltage relationship is given by

$$V_{dc} \;\cong\; \frac{d\psi}{dt} \;=\; \frac{\left(L_a^s - L_u\right) \cdot I}{t} \quad [V] \tag{5.6}$$

Where $L_a^s$ symbolizes the aligned saturated inductance per phase, $L_u$ the unaligned inductance per phase, V the applied voltage and t the time it takes for the rotor to move from the unaligned to the aligned position. That time time can also be expressed in terms of the stator pole arc, $\beta_s$, and rotor speed, $\omega_m$, as

$$t \;=\; \frac{\beta_s}{\omega_m} \quad [s] \tag{5.7}$$

The ratio between aligned inductance and unaligned inductance is defined as

$$\sigma_u \;=\; \frac{L_a^u}{L_u} \tag{5.8}$$

Seeing that a real machine saturates in its rated operation zone, a correction factor must be considered for the inductance ratio.

$$\sigma_s \;=\; \frac{L_a^s}{L_a^u} \tag{5.9}$$

Where $L_a^s$ stands for aligned saturated inductance and $L_a^u$ aligned unsaturated inductance. Substituting equations 5.8, 5.9 and 5.7 in equation 5.6, results in

$$V_{dc} \;=\; \frac{\omega_m}{\beta_s} \cdot L_a^s \cdot I \cdot \left(1 - \frac{1}{\sigma_s \cdot \sigma_u}\right) \quad [V] \tag{5.10}$$

In the aligned position, the flux-linkage can be described by the product of the total number of turns per phase, N, with the aligned flux

$$L_a^s \cdot I \;=\; \phi \cdot N \quad [V \cdot s] \tag{5.11}$$

Recording that magnetic flux is nothing other than the total magnetic field passing through a surface. Knowing the stator pole flux density, B, at the aligned position and the area of the stator pole $A_{sp}$, it becomes easy to describe the flux linkage in terms of the machine dimensions.

$$\phi \cdot N \;=\; A_{sp} \cdot B \cdot N \quad [V \cdot s] \tag{5.12}$$

The surface in which the flux flows through, can be viewed as an rectangle, therefore the stator pole area is given by its height times the side. The side is nothing less than the stator core length,$L_{fe}$, and considering that the motor cross section is a circular shape, its height can be determined as the product of the stator inner radius, $\frac{Ds_i}{2}$, with the stator pole arc $\beta_s$.

Taking into account all of the above

$$L_a^s \cdot I \;=\; \phi \cdot N \;=\; B \cdot A_{sp} \cdot N \;=\; B \cdot N \cdot \cdot L_{fe} \cdot \left(\frac{Ds_i}{2} \cdot \beta_s\right) \quad [H \cdot A] \tag{5.13}$$

The current is dependent on the specific electric loading, $A_s$, which is defined as [2]

$$A_s \;=\; \frac{2 \cdot N \cdot I \cdot m}{\pi \cdot Ds_i} \quad [A/m] \tag{5.14}$$

Where m stands for the number of phases conducting simultaneously and $Ds_i$ the stator inner diameter. In the case of a 12/8 configuration, only one phase conducts at a time.

The specific electric loading is generally within the range of
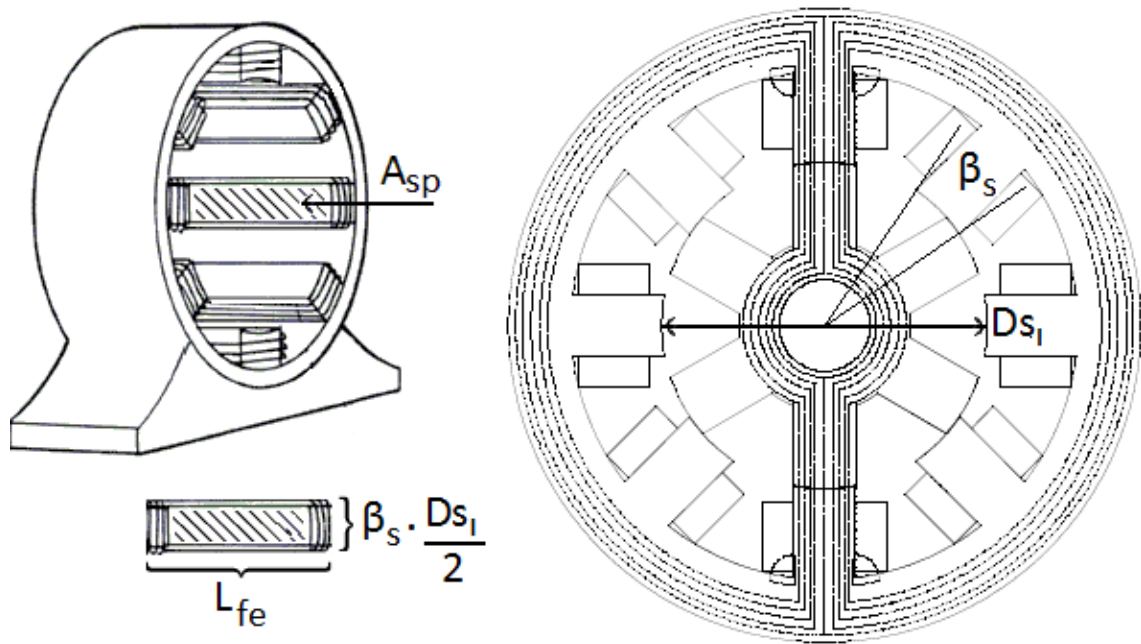
Figure 5.5: Stator pole area

$$25000 \; < \; A_s \; < \; 90000 \tag{5.15}$$

The machine duty cycle can be expressed as [2]

$$k_d \;\; = \;\; \frac{\theta_c \cdot N_{ph} \cdot N_r}{360} \tag{5.16}$$

Where $\theta_c$ represents the current conduction angle for each rising inductance profile, and therefore can be the same as the step angle. Generally the duty may vary from 0.5 to 1, but can be assumed to be one to start with.

The power developed by the machine when taking into account its efficiency, $\eta$, duty cycle, $k_d$, power supply voltage, $V_{dc}$, and maximum allowed peak current, $I_p$, is given by

$$P_n \;\; = \;\; \eta \cdot k_d \cdot V \cdot I_p \cdot N_{ph} \quad [W] \tag{5.17}$$

Since the efficiency cannot be determined in advance, and in SRM it is usually in the range of 0.8 and 0.94, it is arbitrary given the value of 0.9.

Combining equations 5.17, 5.13 and 5.10, the power developed as function of machine geometry characteristics is given by

$$P_n \;=\; \eta \cdot k_d \cdot \left(\frac{\pi}{4}\right) \cdot \left(1 - \frac{1}{\sigma_s \cdot \sigma_u}\right) \cdot B \cdot A_s \cdot Ds_i^2 \cdot L_{fe} \cdot \omega_m \quad [W] \tag{5.18}$$

From equation 5.18, the torque can be obtained and expressed as

$$T \;=\; \eta \cdot k_d \cdot \left(\frac{\pi}{4}\right) \cdot \left(1 - \frac{1}{\sigma_s \cdot \sigma_u}\right) \cdot B \cdot A_s \cdot Ds_i^2 \cdot L_{fe} \quad [N \cdot m] \tag{5.19}$$

## 5.6   Sizing internal dimensions

Having the torque as a function of machine parameters, it is possible to start the machine construction design process.

In order to simplify the iterative process of choosing the initial parameters, the stack length is usually a multiple or sub-multiple of the stator inner diameter [2].

$$L_{fe} \;=\; k_L \cdot Ds_i \quad [m] \tag{5.20}$$

Making the output power of the machine proportional to the cube of the stator inner diameter.

$$P_n \;\propto\; k_L \cdot Ds_i^3 \quad [W] \tag{5.21}$$

The ratio between stator length and inner stator diameter, $k_L$, depends on application. Typically for non-servo applications the range is within [2] [11]

$$0.25 \;<\; k_L \;<\; 0.70 \tag{5.22}$$

And for servo applications, it is normally within the range of

$$1 \;<\; k_L \;<\; 3 \tag{5.23}$$

The parameters that are to be defined are the following.

Table 5.4: Switched Reluctance Motor geometry parameters

| Parameter | Symbol | Units |
|---|---|---|
| Stator Pole arc | $\beta_s$ | ° |
| Rotor Pole arc | $\beta_r$ | ° |
| Stator Core length | $L_{fe}$ | m |
| Stator outer diameter | $Ds_o$ | m |
| Air gap | g | m |
| Rotor diameter | $D_r$ | m |
| Shaft diameter | $d_{sh}$ | m |
| Stator Pole Height | $h_s$ | m |
| Rotor Pole Height | $h_r$ | m |
| Stator Yoke Thickness | $y_s$ | m |
| Rotor Yoke Thickness | $y_r$ | m |
| Stator Pole Width | $t_s$ | m |
| Rotor Pole Width | $t_r$ | m |

The figure 5.6 presents what each of the table 5.4 parameters represent in physical terms.
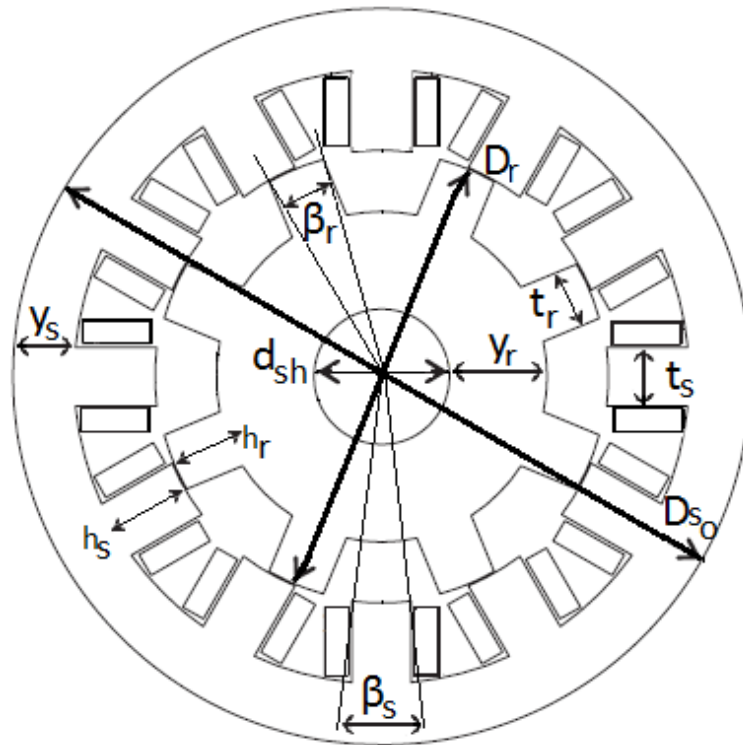


Figure 5.6: Cross section of a 12/8 SRM with its dimensions

### 5.6.1 Pole arcs selection

The choice of the pole arcs is relevant and has a direct impact on the motor ability to meet the required specifications. The rotor pole pitch, $\tau_s$, and rotor pole pitch, $\tau_r$ are defined as

$$\tau_r \quad = \quad \frac{2 \cdot \pi}{N_r} \tag{5.24}$$

$$\tau_s \quad = \quad \frac{2 \cdot \pi}{N_s} \tag{5.25}$$

In order to produce a continuous torque, the minimum stator pole arc, $\beta_s$, and rotor pole arc, $\beta_r$, must be greater than the stroke angle, $\varepsilon°$, to ensure that there is always an overlap of at least 2 stator and rotor pairs, thus there are no gaps where no torque is produced.

$$\beta_s \ , \ \beta_r \quad > \quad \varepsilon° \tag{5.26}$$

As the stator pole arc increases, the slot area decreases and limits the maximum magnetomotive force (MMF) and therefore the maximum torque. On the other hand, from a mechanical aspect a narrower stator pole can be easier stimulated to oscillate, that increases the acoustic noise [11].

If the above condition is not met, the motor won't be able to self start in some situations. In order to get the largest possible variation of phase inductance with rotor position, and therefore the largest average torque, the interpolar arc of the rotor must exceed the stator pole arc. Leading to the condition

$$\left( \beta_s + \beta_r \right) \quad \leq \quad \tau_r \tag{5.27}$$

which ensures that when the rotor is in the 'unaligned' position relative to the stator poles of one phase, there will be no overlap and therefore a very low inductance [6].

A further constraint on the pole arcs is that usually the stator pole arc is made slightly smaller than the rotor pole arc.

$$\beta_r \quad \geq \quad \beta_s \tag{5.28}$$

Making the rotor pole arc bigger than the stator pole arcs has its benefits. Since in SRMs it is impossible to have ideal current turn-off (zero time for the current to return to zero), as to avoid the production of negative torque, a "dead-zone" can be created in the inductance profile ($\theta_3$ - $\theta_2$), which is given by ($\beta_s$ - $\beta_r$). There is no torque produced even if there is current present, thus increasing the average torque contribution of a phase winding. Elimination of negative torque also reduces the torque ripples and hence the audible noise generation.

Due to the dead zone in which no torque is produced, it is possible to maintain the peak current for the entire positive torque producing region. Thus the average torque is bigger in machines where $\beta_r \geq \beta_s$ than with equal stator and rotor pole arcs. The effect is illustrated in figure 5.7.
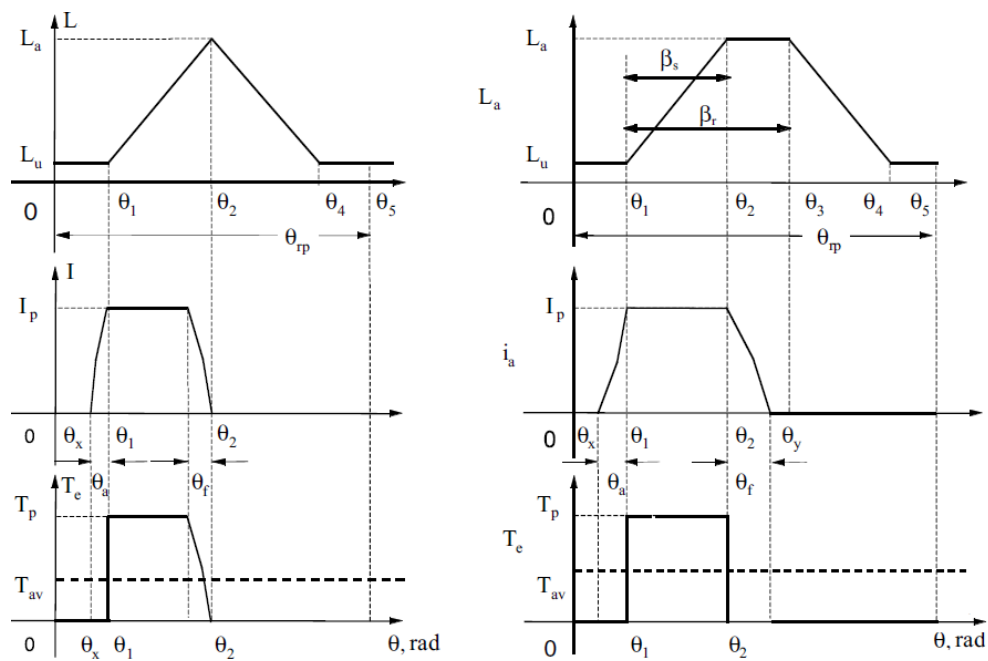
Figure 5.7: Effect of pole arcs on torque generation for same peak currents a) $\beta_r = \beta_s$  b) $\beta_r > \beta_s$ [2]

Given all these factors, it can be seen that it is very advantageous to have the rotor pole arc greater than the stator pole arc.

The constraints to the pole arcs can be expressed graphically as in figure 5.8 in which the 'feasible triangles' define the range of combinations normally permissible [46].
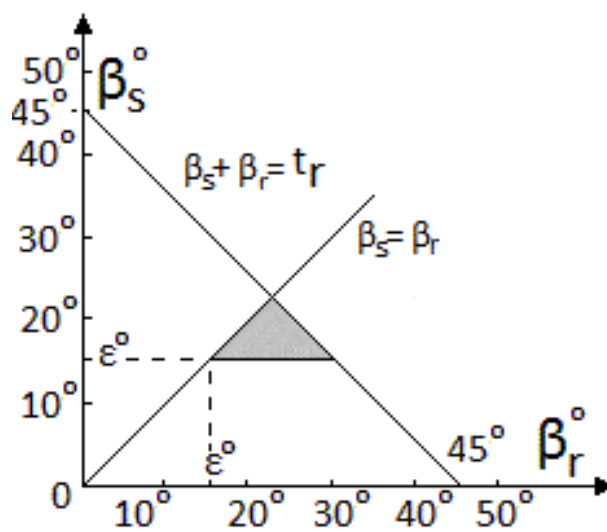


Figure 5.8: Pole arc constraints (feasible triangles) for a three-phase 12/8 SRM

### 5.6.2   Air gap

Aligned inductance is inversely proportional to the air gap length, g, hence any decrease in the air gap results in an increase in the aligned inductance. Thus maintaining all the parameters the same, decreasing the air gap results in a increase in the output torque. However the air gap is not always defined by the manufacturing tolerances, because the available dc link voltage may not be sufficient to force and maintain the desired current, although the decrease in aligned inductance can be accomplished by other means, such as the number of turns in the winding, reduce the motor length or its bore diameter [2].

There are some rough guides to chose the air gap length. In [47] states that if the rotor diameter and stator stack length ratio ($\frac{L_{fe}}{Dr}$) is unitary, then the air gap length should be 0.5% of the rotor diameter. There is some research stating that a high ratio, between 50 and 120, of rotor pole pitch to air gap length $\frac{\tau_r}{g}$ results in maximum torque [43] [48] [49].

Typically the air gap length values depending on the machine size and applications are in the range of [11] [2]

$$0.2 \; < \; g \; < \; 0.6 \quad [mm] \tag{5.29}$$

### 5.6.3   Yoke thickness

Once the pole arcs have been chosen, the stator pole width $t_s$ and rotor pole width $t_r$ can be determined.

$$t_s \;\; = \;\; 2 \cdot \frac{Ds_i}{2} \cdot sin\left(\frac{\beta_s}{2}\right) \;\; = \;\; 2 \cdot \left(\frac{D_r}{2} + g\right) \cdot sin\left(\frac{\beta_s}{2}\right) \quad [m] \tag{5.30}$$

$$t_r \;\; = \;\; 2 \cdot \frac{D_r}{2} \cdot sin\left(\frac{\beta_r}{2}\right) \quad [m] \tag{5.31}$$

The stator back iron thickness, or yoke thickness, $y_s$, is determined on the basis of maximum flux density in it and by the additional of vibration minimization to reduce acoustic noise [2]. The stator and rotor yoke thickness, $y_r$, should be sufficient to carry the peak magnetic flux without saturating. In SRM with 2-pole flux pattern, the main flux is divided into two parallel equivalent parts. Then yoke thickness should be at least $\frac{t_s}{2}$ and $\frac{t_r}{2}$, but preferably 20% - 40% more, because during commutation of two sucessive phases, the overlapping of poles can occur, therefore

$$y_s \;\; = \;\; (1,4) \cdot \frac{t_s}{2} \quad [m] \tag{5.32}$$

$$y_r \;\; = \;\; (1,4) \cdot \frac{t_r}{2} \quad [m] \tag{5.33}$$

### 5.6.4   Rotor pole height

The bigger the rotor pole height, the bigger it is the inductance ratio $\frac{L_a}{L_u}$, and therefore for the same current a greater torque is achieved. However considering that stator outer diameter is already fixed, the bigger the rotor pole height, the smaller the stator pole height must be, which leads to a smaller space for the winding. According to [47], the rotor pole height should be in the range of

$$h_r = k_{hr} \cdot g \ , \ \ 20 \ < \ k_{hr} < 30 \quad [m] \tag{5.34}$$

### 5.6.5   Shaft diameter

A shaft in an electric motor is used to transmit torque and power from the motor to an external loading machine. Because motor shafts are subjected to various combined effects of tension, compression, bending, and torsion during operation, they are typically designed for maximum stiffness and rigidity and minimum deflection to maintain shaft stress/strain below allowable limits under various loading and operating conditions [50].
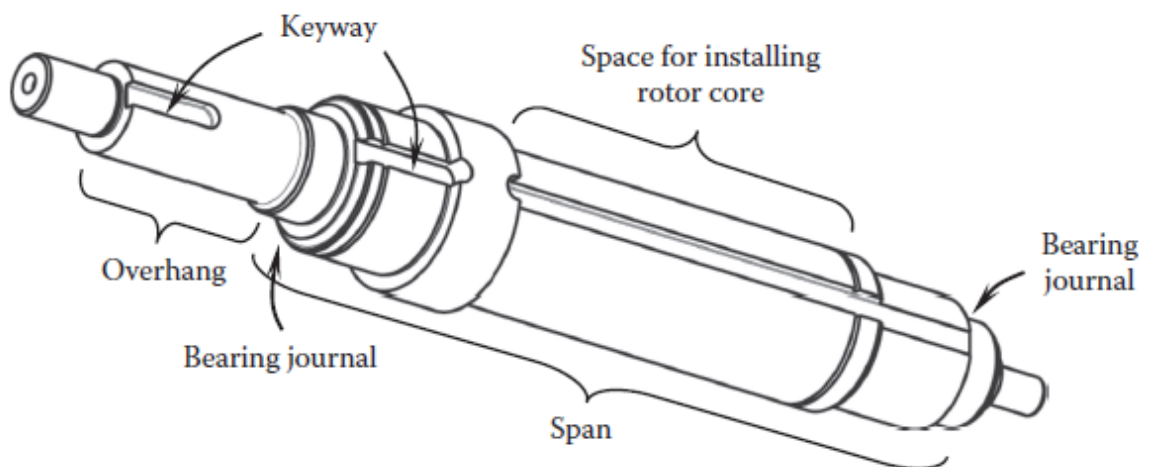


Figure 5.9: Structure of a motor shaft [50]

In the motor that is being designed, the shaft diameter was already a specification, nonetheless if the height and width of the rotor poles and the rotor yoke thickness are fixed, then the shaft diameter can be obtained with the outer rotor diameter Dr as follows:

$$d_{sh} = D_r - 2 \cdot \left( h_r + y_r \right) \quad [m] \tag{5.35}$$

## 5.7   Winding design

Windings play a fundamental role in electric machines by creating magnetomotive force (MMF) distribution. There are different types of windings, depending on the electric machine and application. For salient pole machines, such as the switched reluctance motor, concentrated windings are widely used.

### 5.7.1   Concentrated Windings

On a SRM with 12/8 configuration each phase is made up of four stator poles, and consequently four coils concentrated around them. The connection of the phase coils, series or parallel, strongly influences the rate of rise of the current when the phase is energized. Connecting the coils in parallel reduces unbalanced rotor forces that occur if the rotor is displaced from the center line. In machines with very long stator stack length, rotor eccentricity can be a problem that needs to be taken into account. However in most machines design unbalanced forces are not critical, and thus both serial and parallel coil configurations are used.

Depending on the direction of the coils, different flux paths are held.
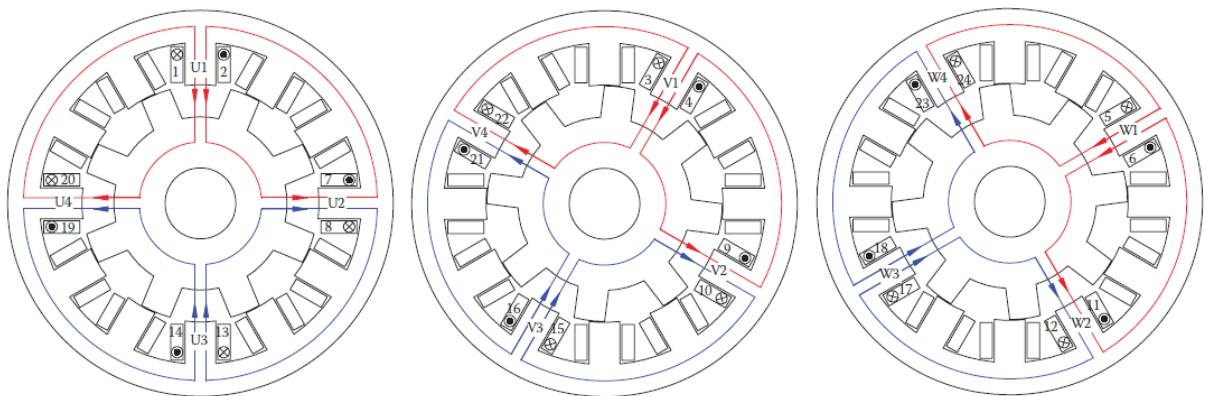


Figure 5.10: Flux path of a salient pole winding with coils with the same polarity in each side [36]

Theoretically, the flux paths presented in figures 5.10 and 5.11 produce the same output torque. However during commutation, where there is multiple phase conduction, these two configurations can lead to different flux paths and as a consequence output torque is affected.

If the coil directions are modified as shown in figure 5.12 where the flux of all the coils faces the opposite directions, the flux lines complete their paths using the stator poles of adjacent phases, resulting in a higher mutual inductance between phases.

Under his coil configuration torque can still be developed, however the self-inductance is now independent of rotor position, while the mutual inductance between phases varies with rotor position [51]. As a result of the new arrangement, the torque is derived entirely from the rate of change of the mutual inductance between phases. Any two phases are excited during the period
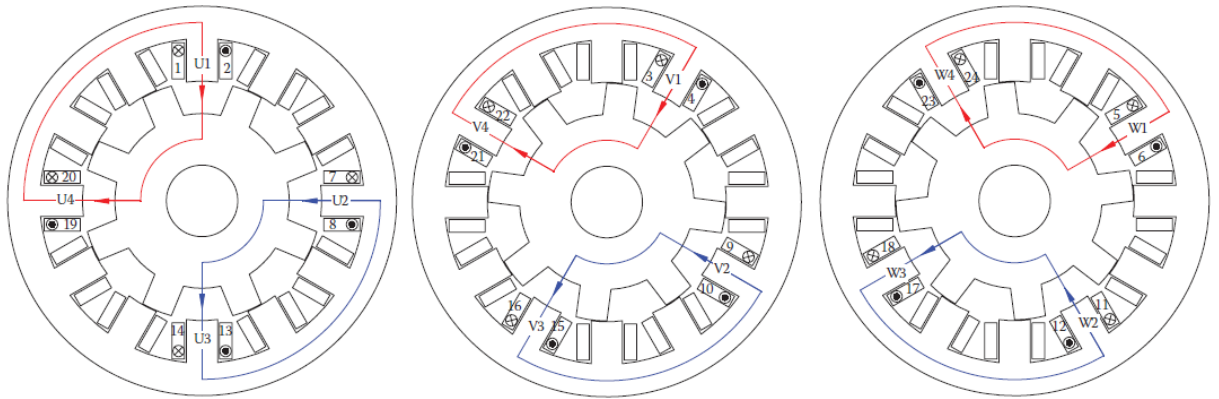
Figure 5.11: Flux path of a salient pole winding with coils with opposite polarity in each side [36]
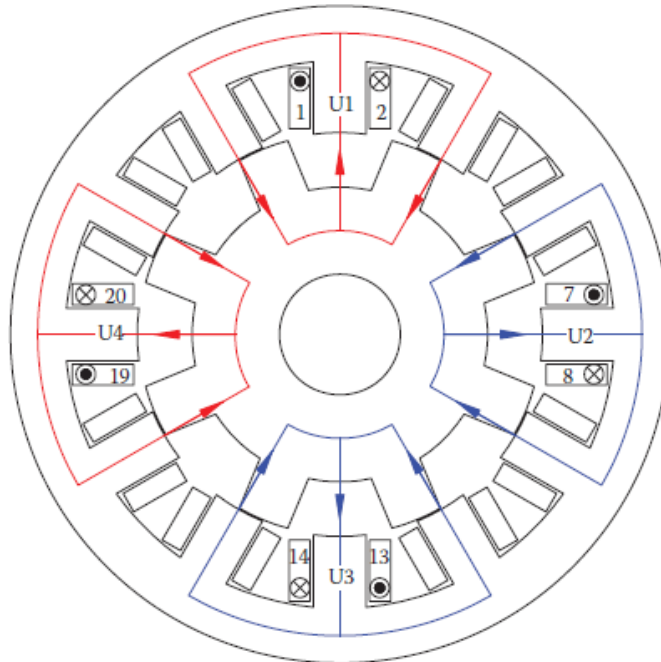


Figure 5.12: Flux path of a salient pole winding with opposite polarities for all the coils, resulting in higher mutual inductance [36]

when their mutual flux linkage is rising, therefore the electromagnetic torque is now produced by the following relationship

$$T_e = I_a \cdot I_b \cdot \frac{dM_{AB}}{d\theta} \quad [N \cdot m] \tag{5.36}$$

Where $I_a$ stands for the current flowing in phase A, $I_b$ the current in phase B and $M_{AB}$ the mutual inductance between phase A and B.

Because of the fundamental change in operating mode, each phase of the machine can contribute to positive torque production for considerably greater one half of the cycle rotation, leading to a more efficient utilization of the windings [52].

Comparative studies have been made concerning the losses between the classical and mutually coupled switched reluctance machine, and for the same load conditions, the mutually coupled SRM copper losses are much lower comparative to the classical SRM, as well as lower iron losses both in the rotor and stator [53].

In order to make use of this coil disposition, different control algorithms that take mutual inductance into account are needed, as well as different power converters [54] than the ones reviewed earlier, as it is not in the scope of the dissertation the review of mutually coupled switched reluctance motors.

### 5.7.2   Coil design

The stator coil dimensions are given by its width, $w_{coil}$, and height, $h_{coil}$, these are determined by the number of turns per coil, $N_{coil}$, and the conductor cross section $S_{cond}$.

$$w_{coil} \cdot h_{coil} \quad = \quad S_{cond} \cdot N_{coil} \quad [m^2] \tag{5.37}$$

The current density $J$, is determined according to the thermal considerations which depend on the SRM cooling system, the coil winding area, $A_{coil}$, can be calculated as

$$A_{coil} \quad = \quad \frac{N_{coil} \cdot I_{RMS}}{J} \quad [m^2] \tag{5.38}$$

With the stator pole arc fixed, the coil width can be obtained by

$$w_{coil} \quad = \quad \frac{\pi \cdot D_{si} - N_s \left( \beta_s \cdot \frac{D_{si}}{2} + w_{cs} \right)}{4 \cdot N_s} \quad [m] \tag{5.39}$$

Where $w_{cs}$ is the space between two stator coils. The coil height can be calculated by dividing the coil winding area by its width.

$$h_{coil} \quad = \quad \frac{A_s}{w_{coil}} \quad [m] \tag{5.40}$$

The minimum stator pole height, $h_s$, is approximately equal to the coil height, but the coil has to be held, therefore some additional space is lost which must be accounted for [2]. The pole height in terms of the coil height $h_{coil}$ is given by

$$h_{coil} \ < \ h_s \ < \ 1.4 \cdot h_{coil} \tag{5.41}$$

### 5.7.2.1 Number of turns

The determination of number of winding turns is an important design parameter, considering that it has a major influence on the final operating behaviour of the machine. At low speeds, the torque is limited by the maximum MMF, $\theta_{coil}$, which is a function of number of turns per coil, $N_{coil}$, and coil current $I_{coil}$.

$$\theta_{coil} = N_{coil} \cdot I_{coil} \tag{5.42}$$

Considering that the current is limited by the machine thermal aspects and the power converter maximum allowed current, the peak torque can be increased by adding additional winding turns. Nonetheless in order to have space necessary space within the stator slot for the extra windings, the conductor cross sectional area, $S_{cond}$, must decrease, consequently current density increases resulting in higher losses.

As the speed increases, the current is no longer limited by the converter but by the available dc link voltage, which becomes insufficient due to the increase in the induced electromotive force. The former is diminished by the reducing the number of turns in the coil, due to the decrease in the inductance. Therefore with a lower number of turns higher currents can be reached at high speed operation. The choice of the optimal turn number is a trade-off between high peak torque at low speed and maximum mechanical output power at high speed [17].

The number of turns per phase can be roughly estimated with the assumption that the conduction angle, $\theta_{dwell}$, of the SRM at a particular speed has a certain value, for example the step angle $\varepsilon^{\circ}$. Under the conditions of single pulse operation and neglecting resistive voltage drops, the maximum flux value is given by the Faraday's law of induction

$$\psi_{peak} = \frac{V_{dc} \cdot \varepsilon^{\circ}}{\omega} \quad [V \cdot s] \tag{5.43}$$

At rated speed the peak flux, $\psi_{peak}$ occurs well before the aligned position, typically when the overlap between the stator and rotor poles is about $\frac{2}{3}$ of the stator pole arc. At this moment it can be assumed that the ampere-turns are sufficient to bring the stator pole to the flux density $\beta_s$ then

$$\psi_{peak} = t_s \cdot L_{fe} \cdot B \cdot n_c \cdot N_{coil} \quad [V \cdot s] \tag{5.44}$$

Substituting equation 5.43 to 5.44 results in

$$N_{coil} = \frac{V_{dc} \cdot \varepsilon^{\circ}}{t_s \cdot L_{fe} \cdot B \cdot n_c \cdot \omega} \tag{5.45}$$

### 5.7.2.2  Slot fill factor

The slot fill factor $\eta_{slot}$ is defined as the ratio of the conductor area over the total slot area. The filling factor is an important design criterion regarding machine efficiency. The higher the $\eta_{slot}$ the less current density is required for the same MMF, as a result the copper losses are reduced.

Usually the slot fill factor is in the range between 30% - 60% [47] [48].

## 5.8   Losses in electrical machines

To evaluate a machine design it is important to understand how the losses are distributed, power losses in electric motor can substantially increase the temperature rise in the windings and deteriorate the performance characteristics of motor. The vast majority of power losses are converted into heat energy, which must be eventually dissipated from the motor to the surrounding environment [50].

During the conversion of electrical power into mechanical power, some of the input power is lost and dissipated inside the machine in the form of heat. The motor efficiency is defined as the ratio of the power output (which equals the power input minus the power losses) to the power input. The efficiency of the machine can be calculated as

$$\eta = \frac{P_{in} - P_{loss}}{P_{in}} \cdot 100\% \tag{5.46}$$

$$\eta = \frac{P_{mech}}{P_{in}} \cdot 100\% \tag{5.47}$$

Where $\eta$ stands for efficiency, $P_{in}$ is the electrical input power, $P_{loss}$ is the total power loss, and $P_{mech}$ is the mechanical output power. The machine power losses can be divided into 4 categories, copper losses, core losses, mechanical losses, and stray load losses that consist of various kinds of losses that are not mentioned previously, and are difficult to predict analytically and to measure accurately.

### 5.8.1   Copper Losses

When current flows through a conductor, due to its inherent resistance, there are associated losses. These can be calculated as

$$P_{cu} = I_{ph}^2 \cdot R_{ph} \tag{5.48}$$

Where $P_{cu}$ stands for copper losses, $V$ for voltage, $I$ current, and $R$ the conductor DC resistance. However this is only true when the current density within the conductor is evenly distributed. Current density, $J$, is defined as the electric current per unit of cross-section of the conductor.

When the current flowing trough the conductor is alternating, its current density might not be homogeneous. As the frequency increases, due to skin effect and proximity effect, the conductor effective resistance increases.

### 5.8.1.1  Skin Effect

As the frequency of the current increases, the current tends to flow on the surface of the conductor, resulting in a non uniform distribution of the current density, this is referred to as skin effect. Skin effect is the result of eddy currents that are generated by the time-changing magnetic field created by the conductor itself.
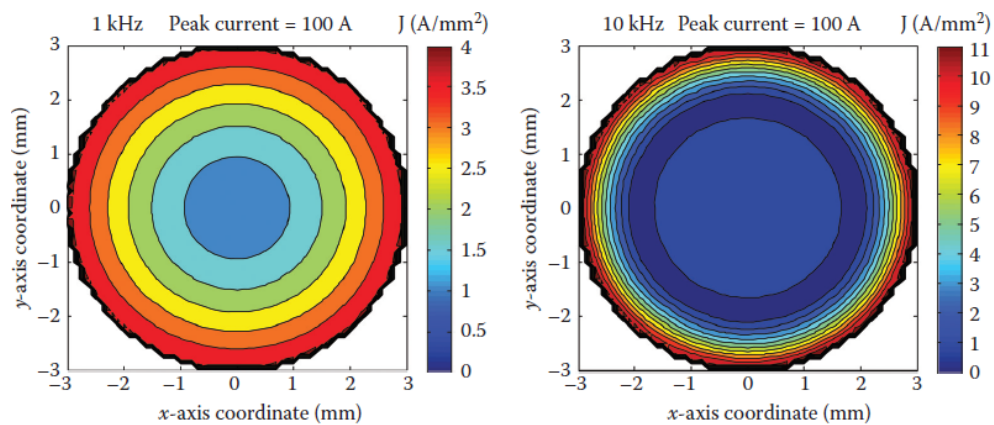


Figure 5.13: Current distribution in a circular conductor for different excitation frequencies [36]

Joule's first law still applies, hence the overall conductor losses are proportional to the square of the current density. Thus, the non-uniform current distribution increases the conductor losses.

### 5.8.1.2  Proximity Effect

Proximity effect is also caused by eddy currents, although unlike skin-effect, the magnetic field is external and is created by current flowing trough one or more nearby conductors. Hence proximity effect occurs at high frequencies and with multilayer windings.

The power losses caused by skin effect and proximity effect, can be mitigated by using Litz wire, it consists of many thin wire strands, individually insulated and twisted together. The path follows two of the parallel strands and it is closed at the coil terminals, where the strands are electrically interconnected Following the path, it becomes obvious that the magnetic field is surrounded in alternating directions. The positive and negative components of the induced voltage cancel each other and therefore no current will flow. For a complete elimination of the induced voltage, the length of lay of the Litz wire needs to be adjusted to the pole length [17].
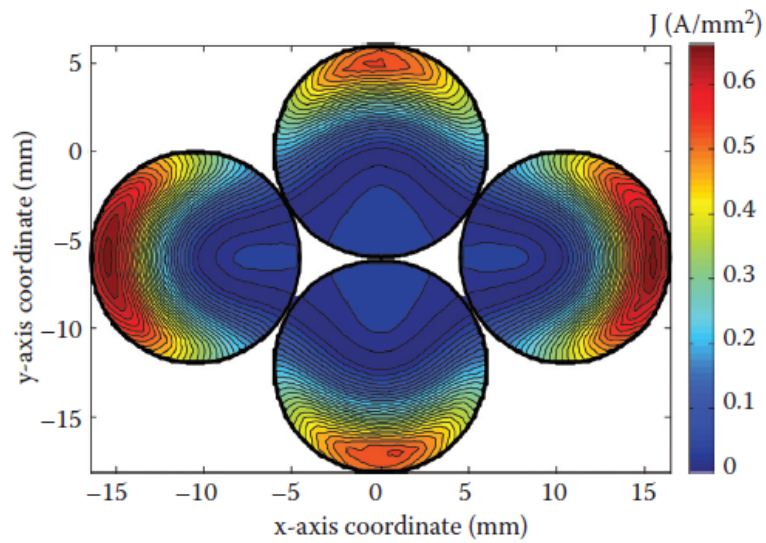
Figure 5.14: Proximity effect on a stranded conductor [36]

## 5.8.2 Core Losses

Also known as iron losses, these are associated with the magnetic losses in the magnetic paths of the motor. When alternating magnetic field is applied to the ferromagnetic material, hysteresis losses and eddy current losses occur.

### 5.8.2.1 Hysteresis losses

Whenever the core is subjected to an alternating magnetic field, the domain present in the material will change their orientation periodically. The power consumed by the magnetic domains for changing the orientation is called Hysteresis loss.



Figure 5.15: Typical hysteresis loop for a ferromagnetic material [55]

The figure 5.15 represents an entire *B-H* magnetization curve. In this process, the area under the *B-H* loop represents the energy, which is required to change the orientation of 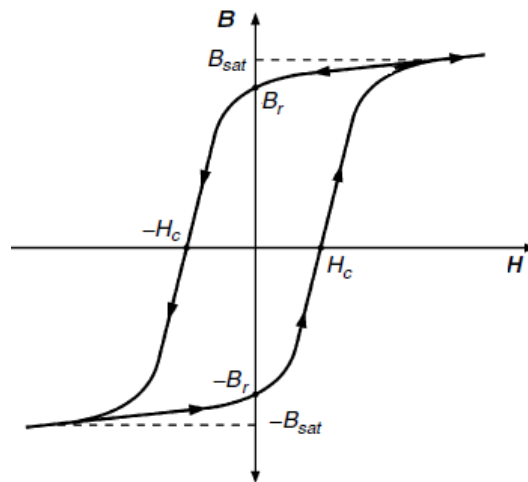domains and expanded in the form of heat. This energy is called as the hysteresis loss and it is dependent on the strength of the magnetic flux density and the excitation frequency [36]

Hysteresis losses are minimized by using high grade silicon steel.

### 5.8.2.2 Eddy current losses

Considering that the magnetic materials used in electric machines are electrically conductive, another type of core losses can occur, the so called eddy current losses. These appear in a similar way as the skin effect, when the core material is exposed to an alternating magnetic field eddy currents are induced in the core.
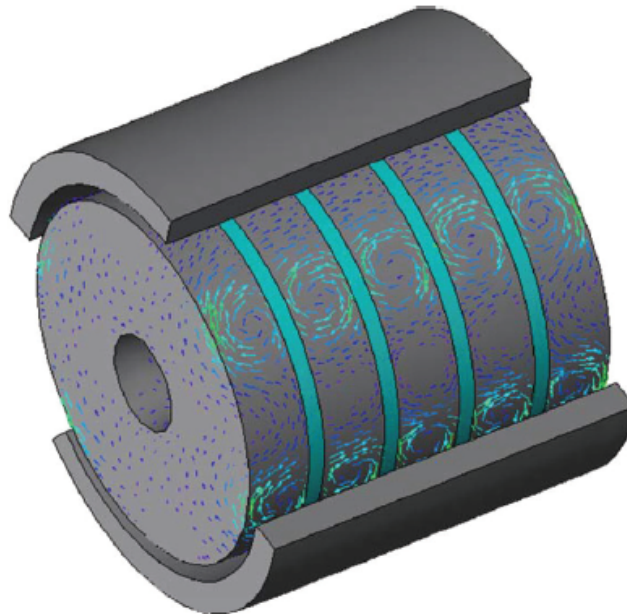


Figure 5.16: Eddy currents and laminations [36]

A way to decrease the density of eddy currents is by using cores made from stacks of many thin laminations. By laminating the core, area decreases and hence resistance increases, therefore decreasing eddy currents and consequently the losses.

### 5.8.3 Mechanical Losses

Mechanical losses in an electric motor refer to the losses due to mechanical friction between two or among more motor components as they contact each other and have relative movements. Whenever there is relative motion of two surfaces in contact, there is frictional resistance between two surfaces [50].

The losses produced by the friction created by the relative movement between air and the machine moving parts are called windage losses. In an electric motor, the windage losses increase exponentially as a function of the rotor rotating speed $\omega_m$ and the rotor radius.

Mechanical losses can also be divided into another category, which are the bearing losses. These are produced by friction on the bearings, and are dependent on a number of factors such as, the dimension of the bearing, bearing type, the shaft rotating speed the lubricant. Bearing losses increase linearly with the shaft speed.

## 5.9   Finite Element Analysis simulation

For a switched reluctance motor, which has many possible configurations, examining of various configurations through constructing and testing prototypes is too costly, so the virtual prototyping is the best option [35].

The final machine design is achieved trough an iterative process of analytical steady-state and dynamic performance calculations. Making use of *ANSYS Maxwell*, the following iterative approach was taken.
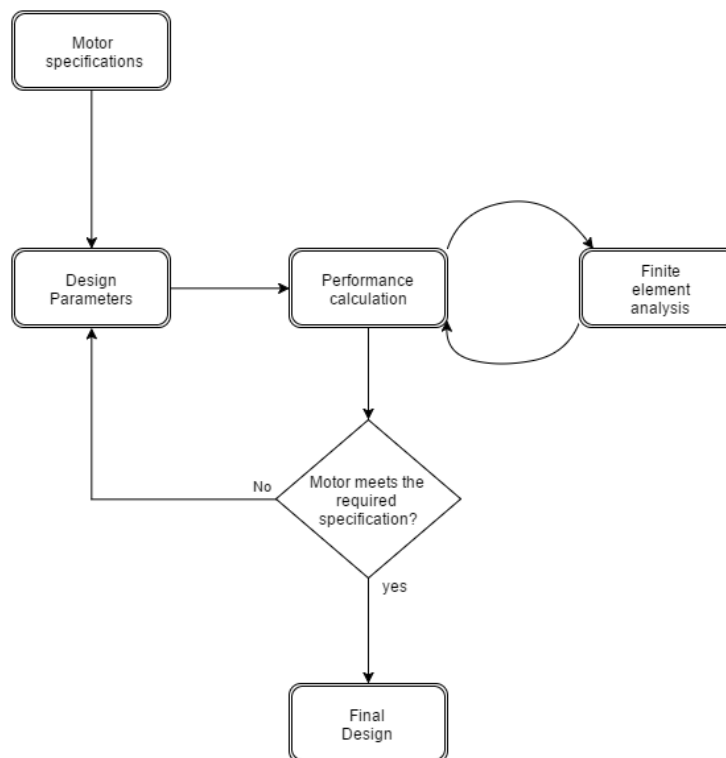


Figure 5.17: Machine design process

With the basic knowledge of how each variable affects the overall machine performance, it is possible to start the motor initial design.

The machine specifications and constraints were the following.

Table 5.5: Specifications and constraints of the machine

| Parameter | Symbol | Value | Units |
|---|---|---|---|
| Rated output power | $P_n$ | 60000 | W |
| Rated Speed | $n_n$ | 2500 | RPM |
| DC link voltage | $V_{dc}$ | 600 | V |
| Rated Torque | $T_n$ | 230 | *Nm* |
| Number of phases | $N_{ph}$ | 3 | - |
| Multiplicity | M | 2 | - |
| Number of coils per phase | $N_c$ | 4 | - |
| Number of rotor poles | $N_r$ | 8 | - |
| Number of stator poles | $N_s$ | 12 | - |
| Step angle | $\varepsilon^{\circ}$ | 15 | ° |
| Rotor pole pitch | $\tau_r$ | 45 | ° |
| Stator pole pitch | $\tau_s$ | 30 | ° |
| Stator outer diameter | $Ds_o$ | 0.380 | m |
| Shaft diameter | $D_{sh}$ | 0.085 | m |
| Flux density | B | 1.8 | T |

Assuming the machine as an efficiency around 90%, and having the DC link voltage and rated output power defined, the current rms value is given by

$$I_{RMS} = \frac{P_n}{V_{dc}} \cdot \left( \frac{100}{\eta} \right) = 111 \quad [A] \tag{5.49}$$

The maximum allowed phase peak current is a function of rms current and number of motor phases and can be calculated as

$$I_p = I_{RMS} \cdot \sqrt{(N_{ph})} = 192.4 \quad [A] \tag{5.50}$$

The company that is manufacturing the machine, WEG, advised a current density of 4.4 $A/mm^2$.

$$J = 4.4 \quad [A \cdot mm^2] \tag{5.51}$$

The air gap was defined by the *WEG*

$$g = 0.0005 \quad [m] \tag{5.52}$$

For the initial design, the simplest way to estimate rotor diameter is from typical ratio $\frac{Ds_o}{D_r}$. This ratio can vary over the range between

$$0.4 \; < \; \frac{Ds_o}{D_r} \; < 0.7 \tag{5.53}$$

Therefore the rotor diameter belongs to the interval

$$0.152 \; < \; D_r \; < 0.266 \quad [m] \tag{5.54}$$

For the first design, some parameters were arbitrated such as the rotor pole arcs in order to model a motor prototype which was then by an iterative process polished, as to meet all the required specifications. The finite element model is constructed for the given prototype and is shown in figure 5.18.
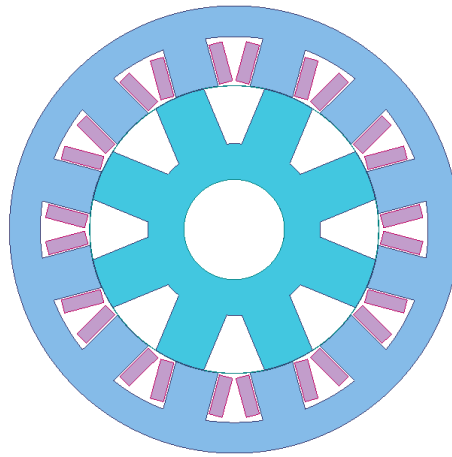
Figure 5.18: Schematic of the designed prototype

The windings polarities are presented in figure 5.19, every marked coil has the same polarity.
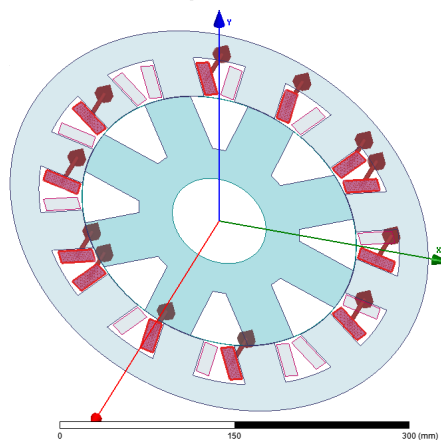
Figure 5.19: Schematic of the motor winding polarities

The final result is a design sheet summarizing all the design parameters and many aspects of performance, including graphical data. The final design parameters are as follows.

Table 5.6: Dimensions of the proposed Switched Reluctance Motor

| Parameter | Symbol | Value | Units |
|---|---|---|---|
| Step angle | $\varepsilon^{\circ}$ | 15 | $\circ$ |
| Stator Pole arc | $\beta_s$ | 17.5 | $\circ$ |
| Rotor Pole arc | $\beta_r$ | 20.5 | $\circ$ |
| Stator Core length | L | 0.160 | m |
| Stator outer diameter | $Ds_o$ | 0.380 | m |
| Air gap | g | 0.0005 | m |
| Rotor diameter | $D_r$ | 0.249 | m |
| Shaft diameter | $d_{sh}$ | 0.085 | m |
| Stator Pole Height | $h_s$ | 0.06 | m |
| Rotor Pole Height | $h_r$ | 0.0516 | m |
| Stator Yoke Thickness | $y_s$ | 0.0261 | m |
| Rotor Yoke Thickness | $y_r$ | 0.0304 | m |
| Stator Pole Width | $t_s$ | 0.0380 | m |
| Rotor Pole Width | $t_r$ | 0.0443 | m |
| Number of Turns per phase | N | 56 | - |

The plot of torque vs position for different currents from 0A to 200A is shown in figure 5.20, the plot of inductance vs rotor position for different currents from 0A to 200A is shown in figure 5.21 and the plot of flux-linkage vs current for different rotor positions is presented in figure 5.22.
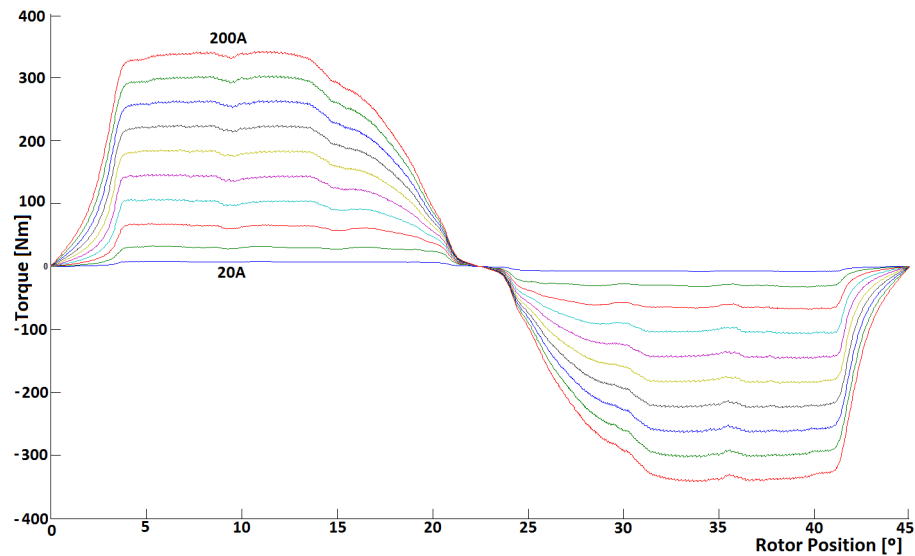


Figure 5.20: Plot of torque vs. rotor position for varying currents from 0A to 200A obtained by finite element analysis
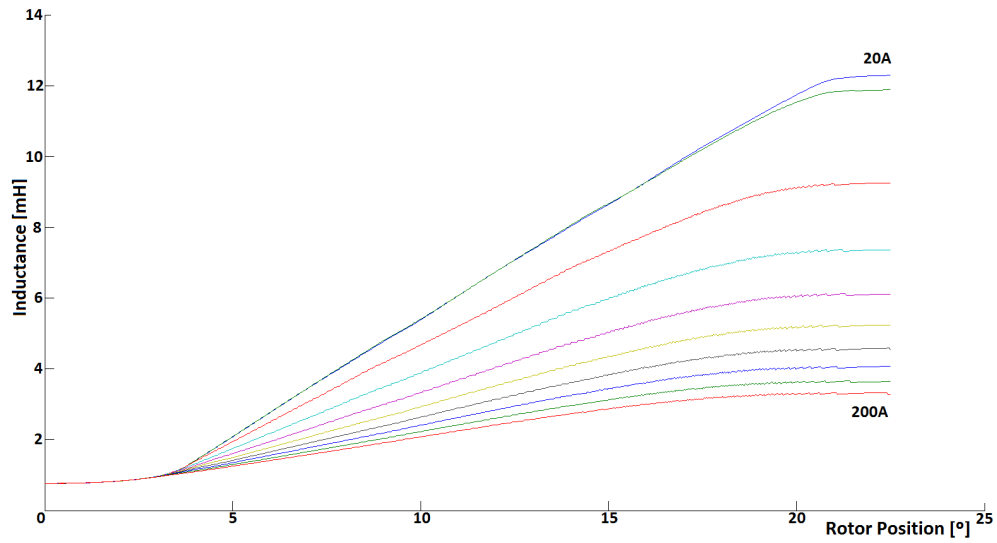
Figure 5.21: Plot of inductance vs. rotor position for varying currents from 0A to 200A obtained by finite element analysis
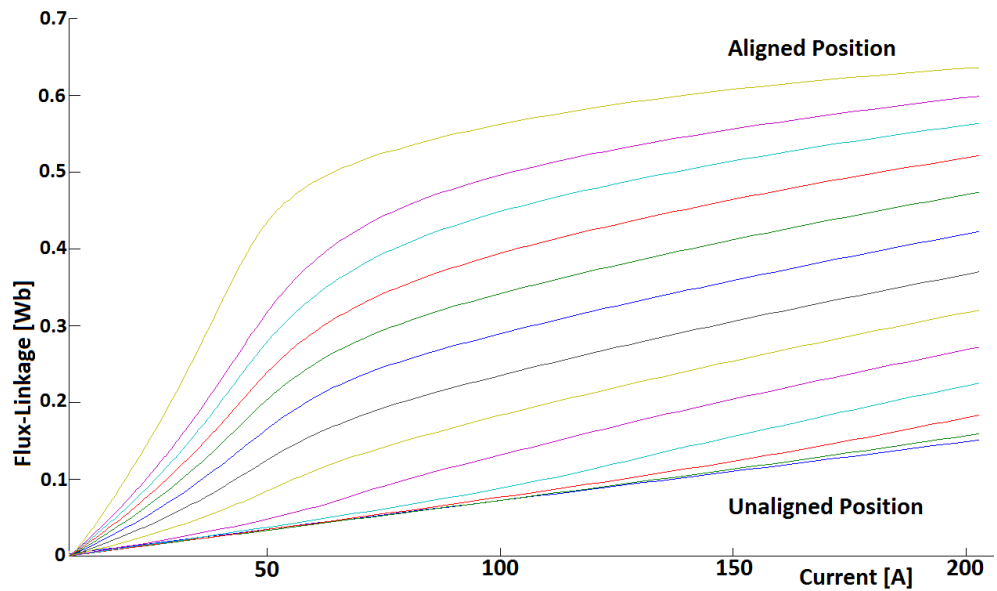


Figure 5.22: Plot of obtained by finite element analysis

The torque developed by the motor at rated speed with trapezoidal rated current profile is presented in figure 5.23.
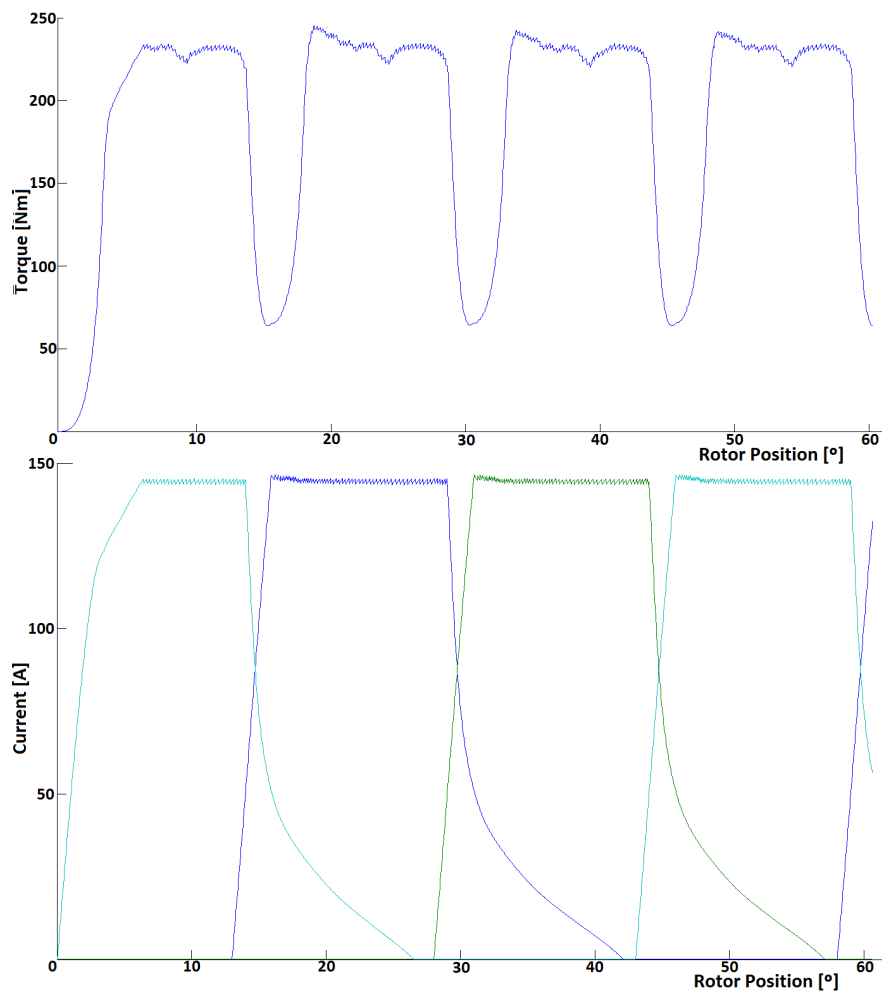


Figure 5.23: Torque developed at 2500 RPM with rated current

The average torque at 2500 RPM is

$$T_{avg} = 188 \quad [N \cdot m] \tag{5.55}$$

The torque ripple is given by

$$T_{ripple} \quad = \quad \left| \frac{T_{max} - T_{min}}{T_{avg}} \cdot 100\% \right| = \left| \frac{245 - 63}{188} \cdot 100\% \right| = 96\% \tag{5.56}$$

Where $T_{max}$ is the maximum torque, $T_{min}$ the minimum torque and $T_{avg}$ is the average torque. During the design of the motor, no control techniques were employed apart from an hysteretic control of the current, which explains the considerable ripple.

The non saturated inductance profiles of the motor are shown in figure 5.25 and the flux density distribution as the motor is moving, is presented in figure 5.24.
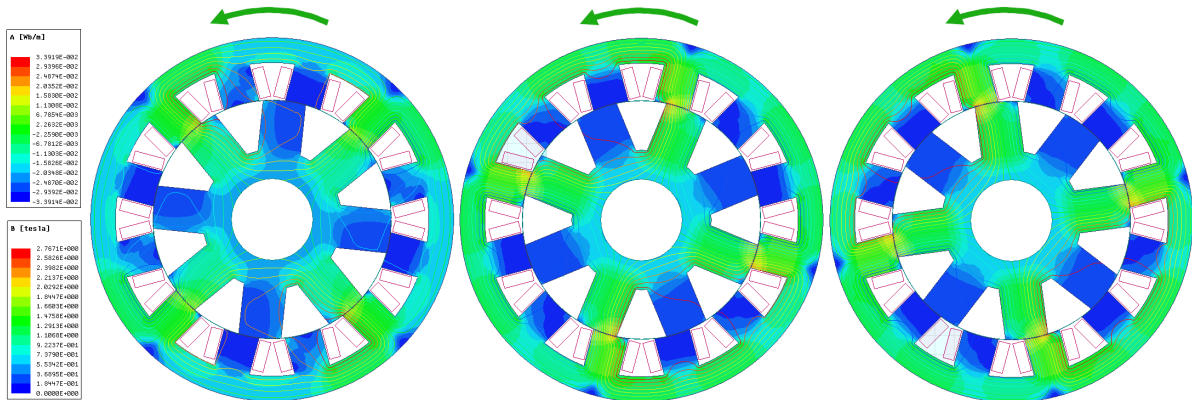


Figure 5.24: FEA solution for the sequential excitation of all phases and the corresponding motion of the outer rotor
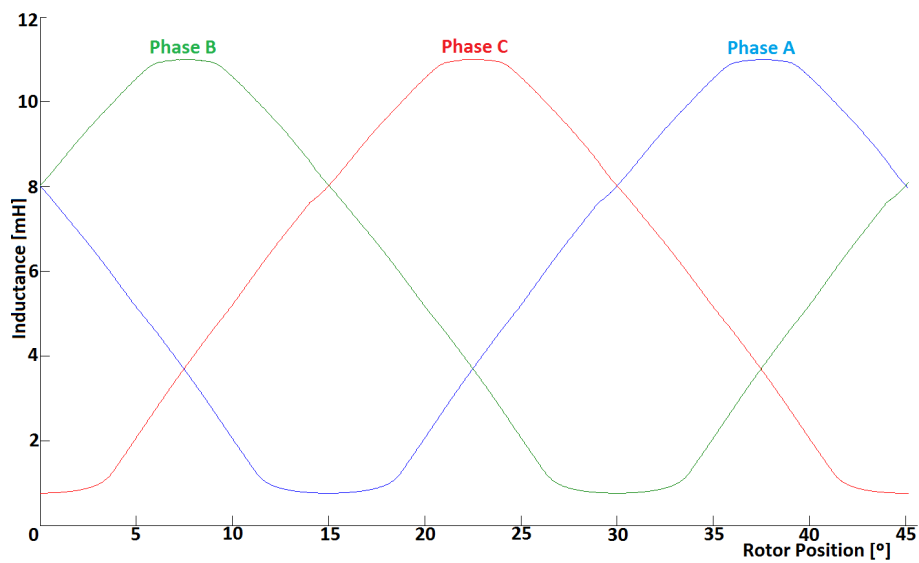


Figure 5.25: Unsaturated inductance profiles for all the phases

The following planes were withdrawn from the finite element analysis and are to be used later for the control scheme.
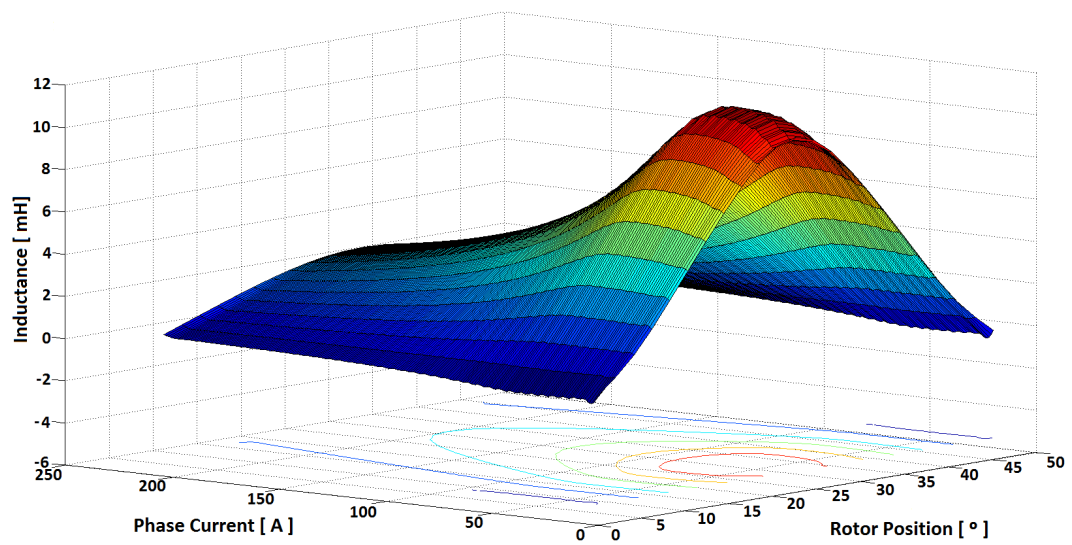
Figure 5.26: Phase inductance as a function of phase current and rotor position 5.21
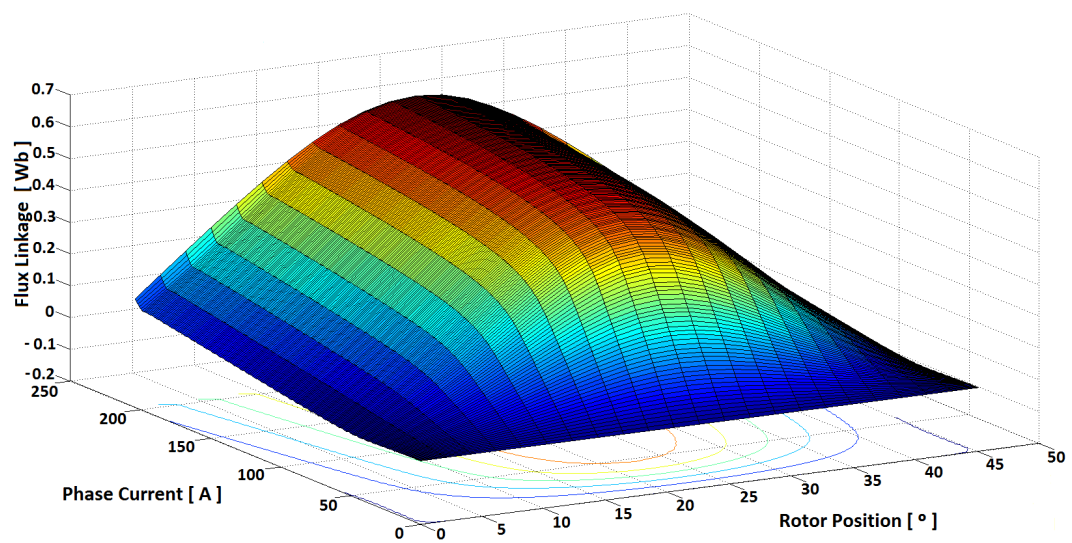


Figure 5.27: Flux linkage as a function of phase current and rotor position
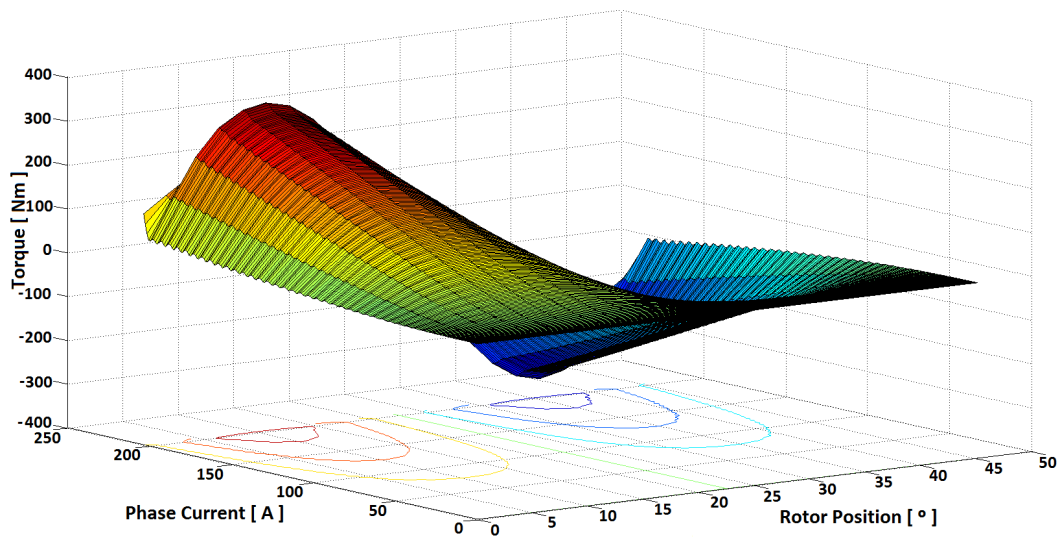
Figure 5.28: Torque produced by one phase as a function of phase current and rotor position

## 5.10   Prototype

The motor was then manufactured by *WEG*. The cross section of the stator is presented in figure 5.29, the rotor in figure 5.30 and both stator and rotor in figure 5.31.
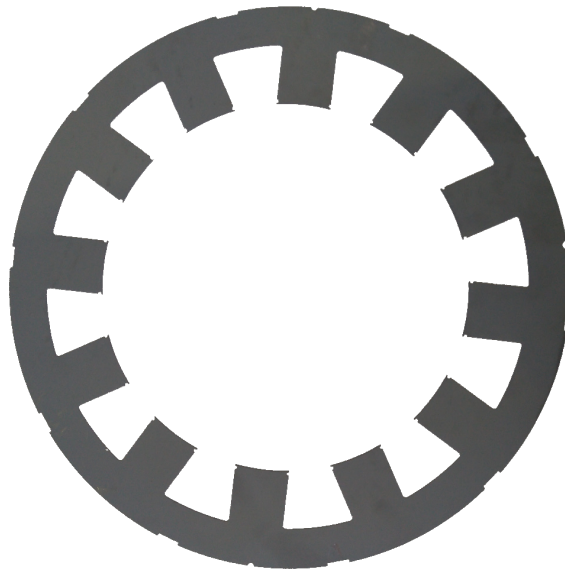


Figure 5.29: Stator cross section

Figure 5.30: Rotor cross section
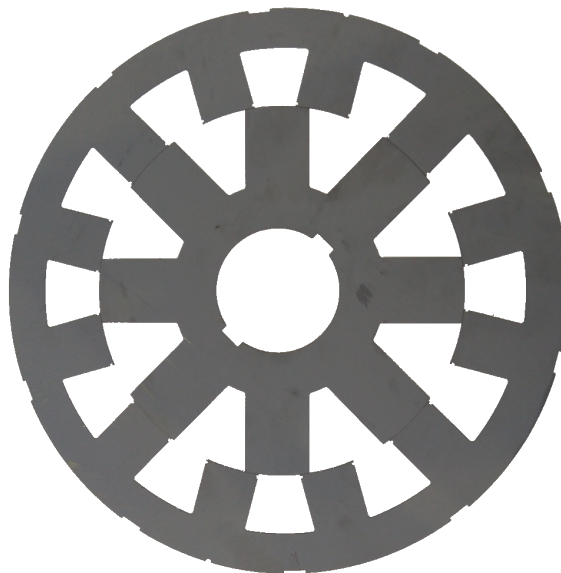


Figure 5.31: Stator and Rotor cross section

As of the writing of the dissertation the motor assembly was still being finished by *WEG* and the most recent picture of the motor is present in figure 5.32.

Figure 5.32: Current status of machine manufacture

## 5.11   Conclusion

In this chapter a 12/8 switched reluctance motor was designed that fulfils the defined requirements and the machine characteristics were extracted from the FEA simulation.

# Chapter 6

# Simulation

## 6.1 Introduction

With the motor designed and built it is necessary to develop a controller capable of driving it. In the following chapter a Simulink based model for the simulation of the motor is developed along with its controller. The motor model is designed based on its working principle covered in chapter 2 and its non linear characteristics extracted from the FEA simulations. The power converter topology used in the simulation was covered in chapter 3 as well as the unipolar switching strategy. The motor controller was devised based on the control schemes reviewed in chapter 4. The simulation results are then presented for different shaft speeds.

## 6.2 Switched Reluctance Motor Drive Model

The motor drive is essentially composed by two components, the motor and the power converter.

### 6.2.1 Motor model

The inputs of the SRM model are the stator phase voltages, and by integrating the difference between the input voltage and the voltage drop across the stator resistance, the magnetic flux linkage in the windings is obtained.

$$\psi(t) \quad = \quad \int_0^t \left( U_{ph} - I_{ph} \cdot R_{ph} \right) \mathrm{d}t. \tag{6.1}$$

The mutual coupling between phases is supposed to be negligible and therefore was not considered in the model. With the magnetisation characteristic presented in the previous chapter, the current as a function of flux and position, $I(\psi, \theta)$, is obtained by making use of a 2d look up table. Figure 6.1 depicts the implementation of the winding current computation block in Simulink. The sampling period is in the same magnitude as the simulation step.
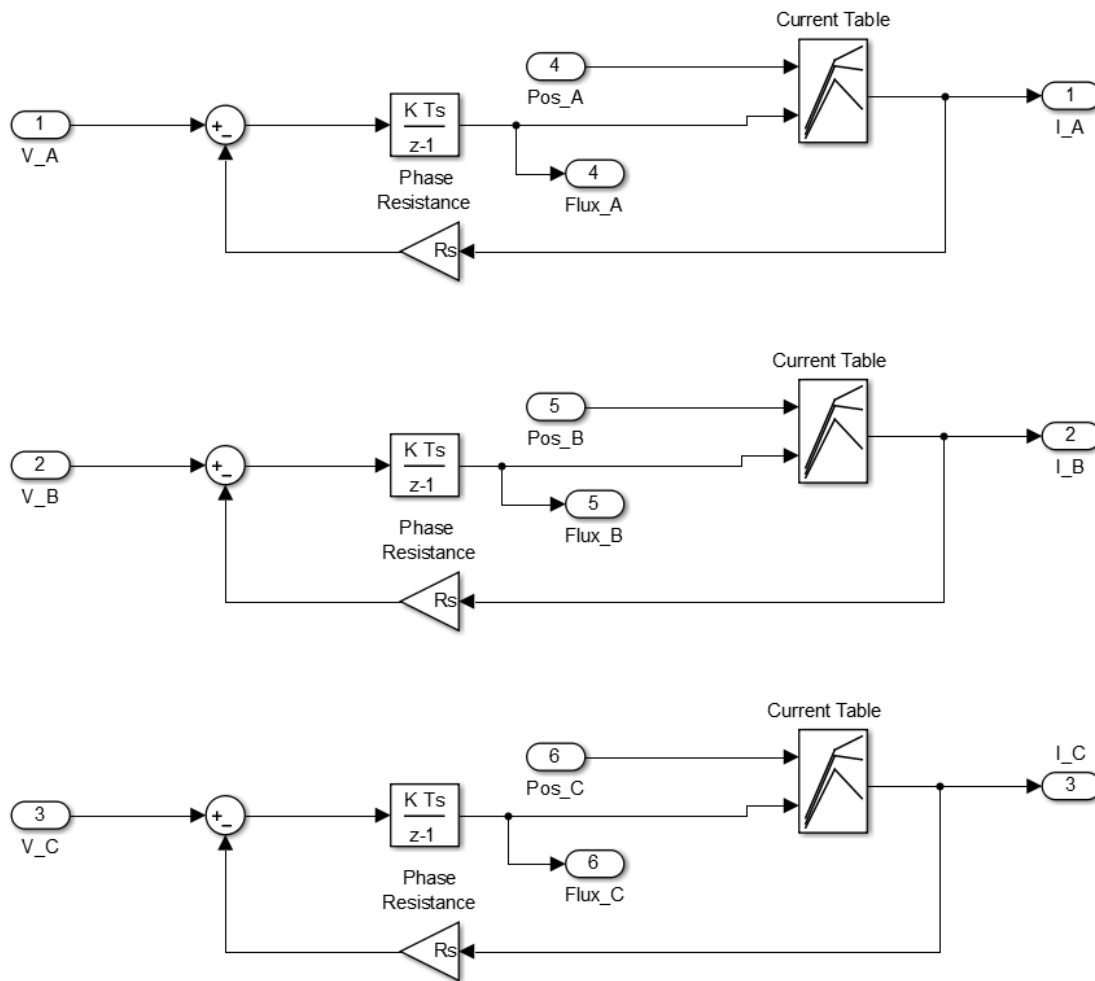
Figure 6.1: Simulink subsystem that computes the windings currents

The electromagnetic torque produced by the machine is equal to the sum of the individual torques produced by each phase. Due to the non linearity of the magnetisation curves, the developed torque is a function of the winding current and rotor position.

$$T_e(I,\theta) \quad = \quad \frac{\partial W_c(I,\theta)}{\partial \theta} \quad [Nm] \tag{6.2}$$

Making use of the data extracted from previous FEA simulations, the torque function, $T_e(I,\theta)$, is implemented by making use of 2d look up tables. The Simulink block containing the computation of the motor output torque is shown in figure 6.2.
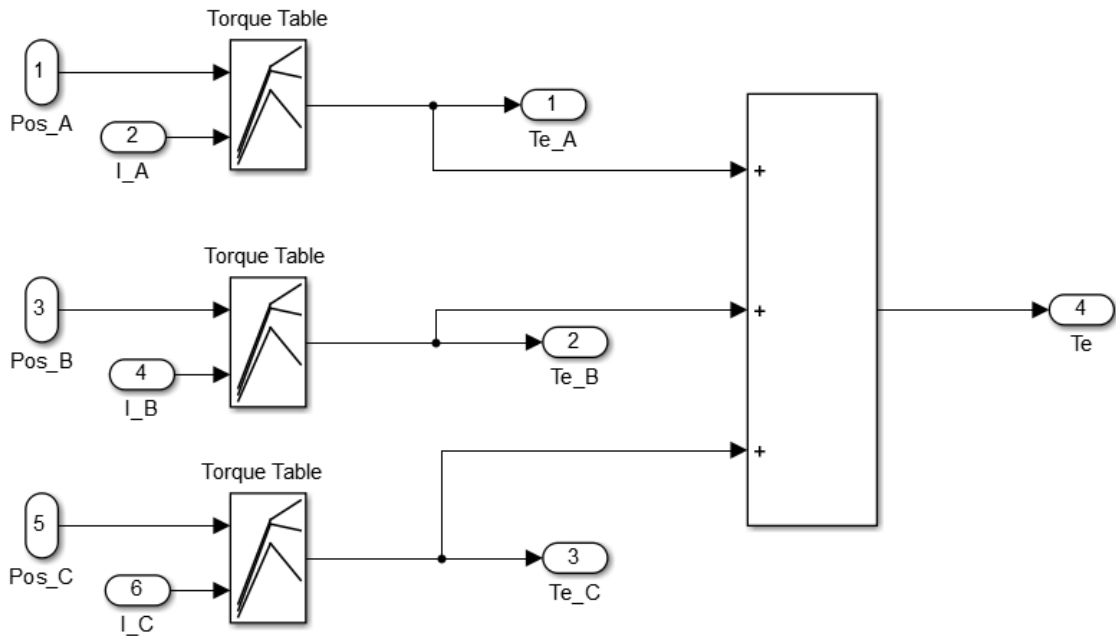
Figure 6.2: Simulink subsystem that computes the output torque

The above subsystems are linked together and their blocks are presented in the figure 6.3.
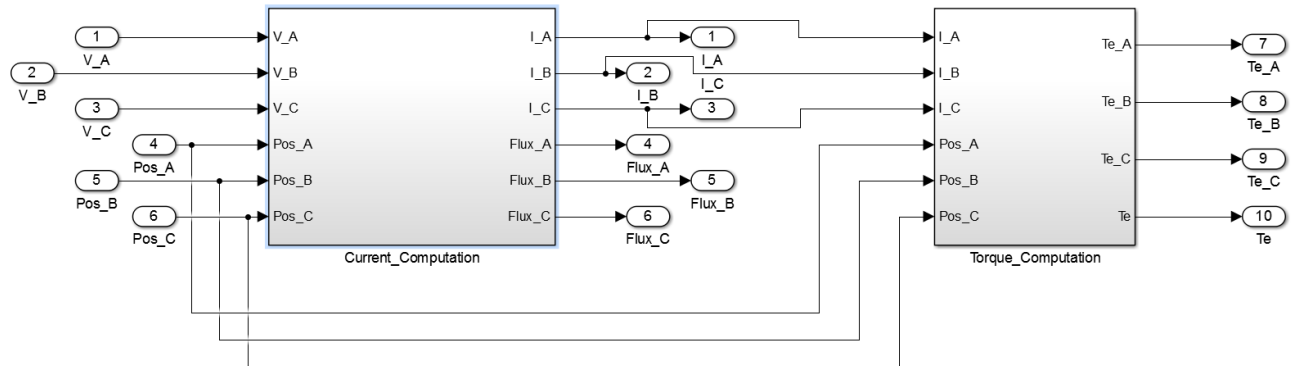


Figure 6.3: Simulink subsystem containing the motor model

#### 6.2.1.1   Mechanical dynamics

The mechanical dynamics of the motor and the load are governed by the motion equation 6.3.

$$T_e \quad = \quad J_m \cdot \frac{\mathrm{d}\omega_m}{\mathrm{d}t} + B_m \cdot \omega_m + T_L \quad [N \cdot m] \tag{6.3}$$

Where $T_e$ stands for the electromagnetic torque developed by the motor, $T_L$ the constant torque required by the load and $\omega_m$ the shaft angular speed. When the mechanical load is directly coupled

to the motor shaft, the total inertia $J_m$ is the sum of the motor and load inertias. There are internal frictional effects in the motor due to several factors such as for example the bearings and these are then translated into torque due the shaft angular speed. Despite the torque generated by friction being small when compared to the torque required by the load, it is necessary to take it into account, with $B_m$ being the sum of the motor and load viscous friction factors.
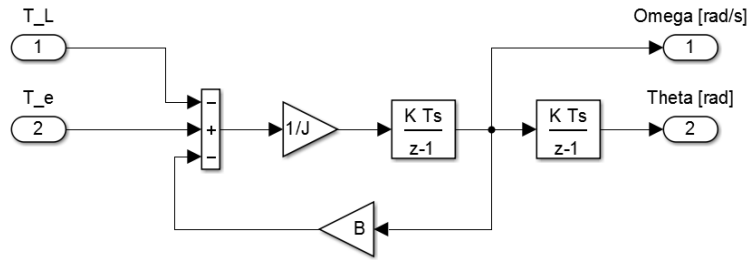


Figure 6.4: Simulink model of the motor and load mechanical characteristics

The main difference between switched reluctance motors with different stator and rotor poles configurations is the inductance cycle. As seen in chapter 2, the inductance cycle period is equal to the rotor pole pitch.

$$\tau_r \quad = \quad \frac{360}{N_r} \quad [°] \tag{6.4}$$

In the case of a 12/8 SRM, the inductance cycle is 45 degrees and each phase has 15 degrees lag from one another. The calculation of each phase relative position is illustrated in figure 6.5
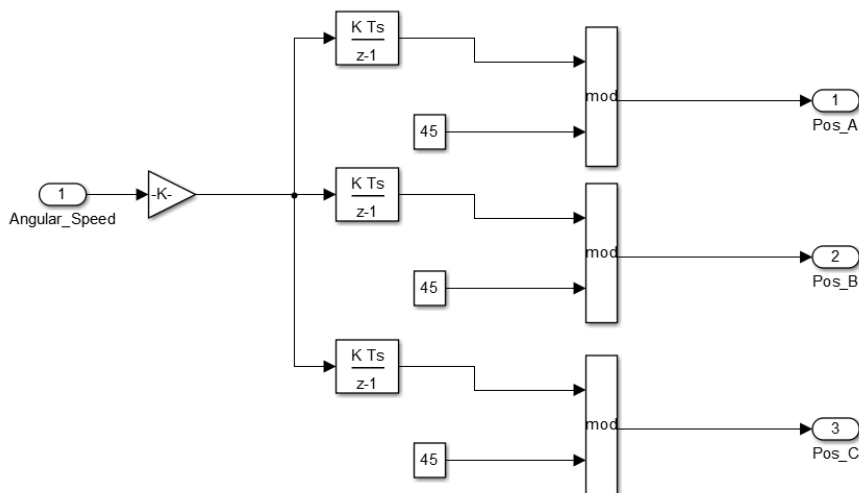


Figure 6.5: Simulink subsystem containing the motor model

The system inputs are the phase voltages provided by the power converter subsystem, and the outputs are the phase currents, flux linkages, torques, shaft position and velocity. With all the blocks presented above, the motor model is concluded and shown in figure 6.7.The connections between said blocks is shown in figure 6.6.
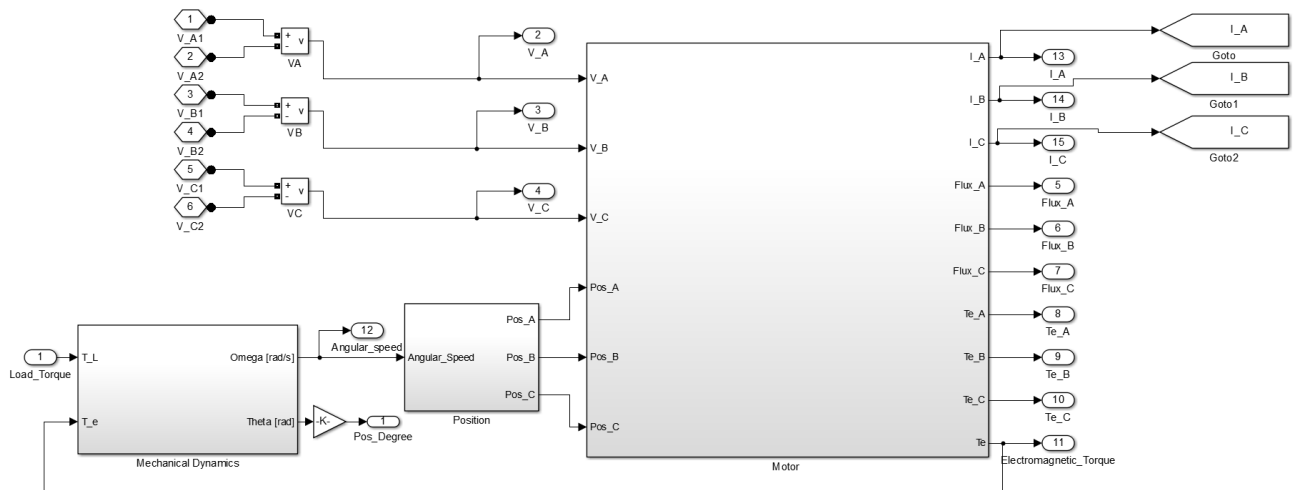


Figure 6.6: Simulink subsystem containing the motor model
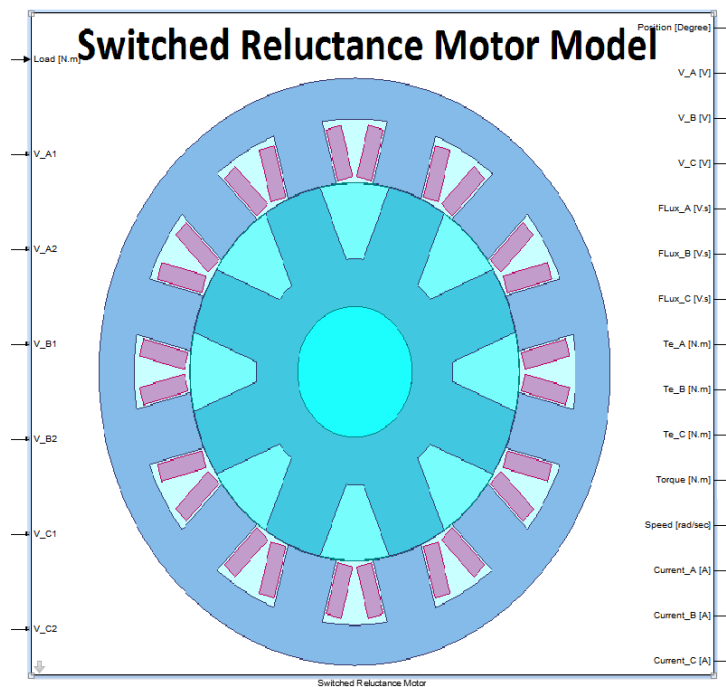


Figure 6.7: Simulink subsystem containing the motor model

### 6.2.2 Power converter

The converter topology used in the simulation was the one described in Chapter 3, the Asymmetric H-bridge. The parameters for the IGBTs and diodes that comprise the converter are only presented in the next chapter.

The power converter subsystem is illustrated in figure 6.9 and its contents are presented in figure 6.8.
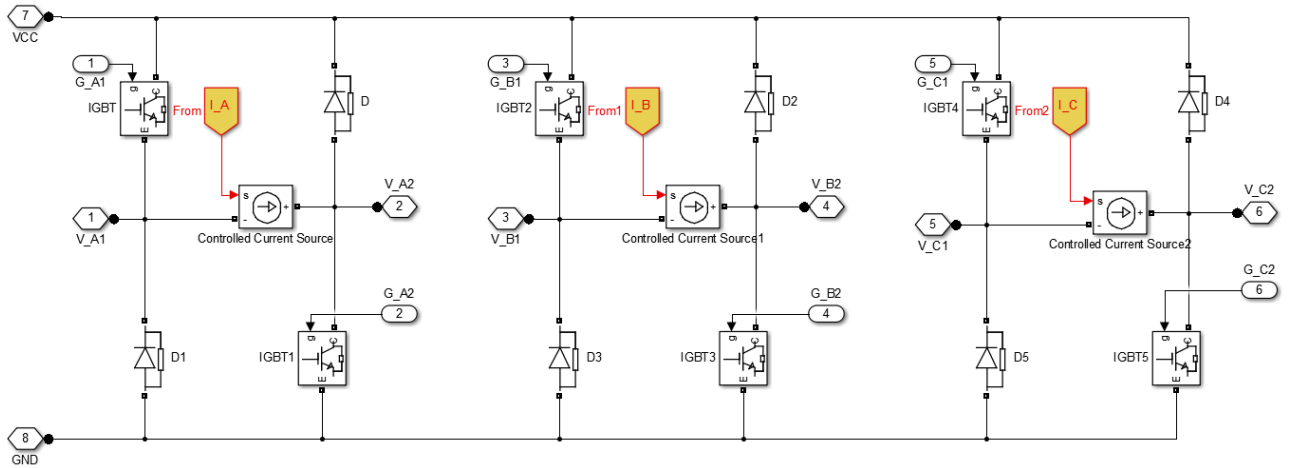
Figure 6.8: Simulink model of the power converter
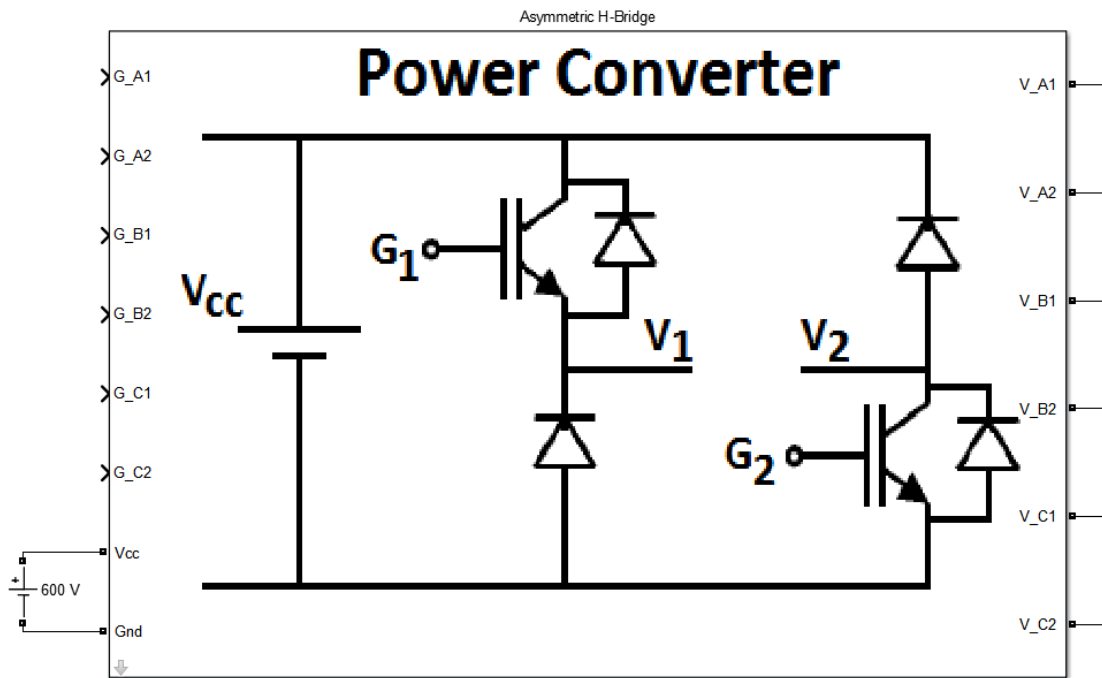
Figure 6.9: Simulink subsystem containing the power converter

### 6.2.3 Model validation

In order to validate the developed electric motor drive model, a basic controller was devised so that the phases are excited sequentially, with $\theta_{on} = 0°$ and $\theta_{off} = 15°$. The phase currents are being controlled by a simple hysteresis controller with a current reference of 150 A, the switching frequency of the power converter is 10kHz. The controller is illustrated in figure 6.10, and the Simulink circuit in figure 6.11.
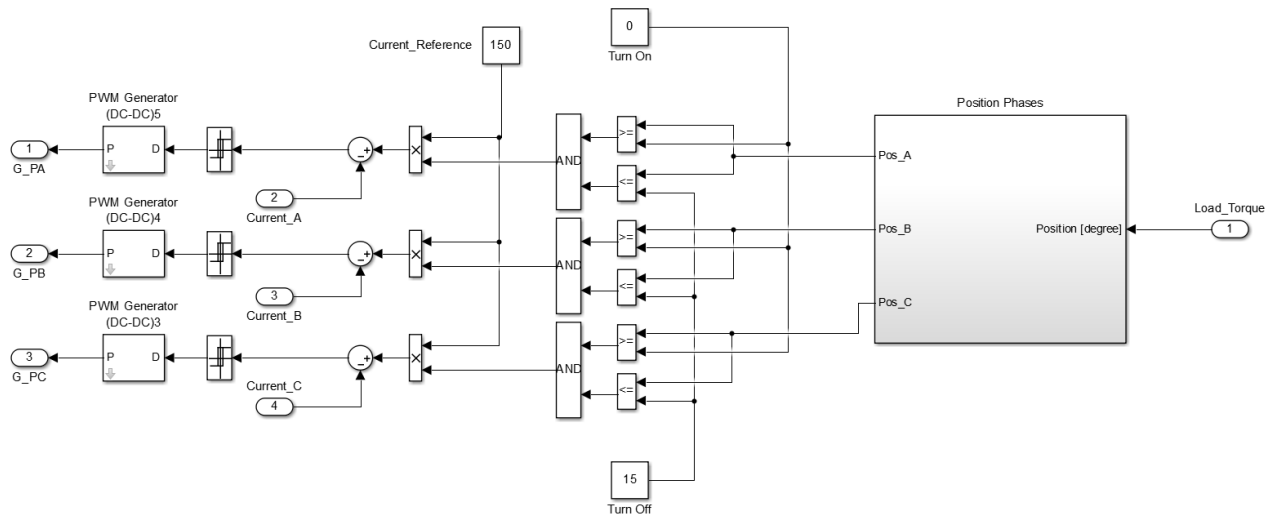


Figure 6.10: Simulink subsystem containing the motor controller
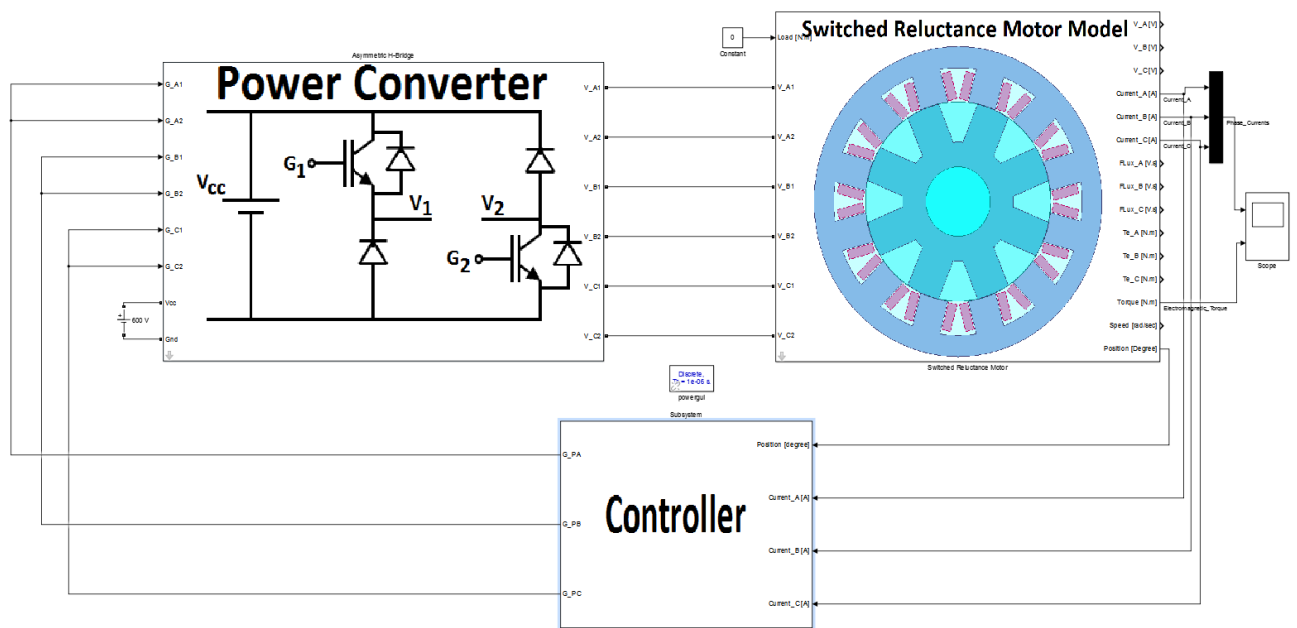


Figure 6.11: Simulink diagram of the SRM drive testing circuit

With an initial velocity of 2500 rotations per minute, for a peak current of 150A the phase currents and the output torque are presented in figure 6.12. The results are in agreement with the previous simulation that made use of Maxwell Ansys software, depicted in figure 5.23 present in chapter 5.
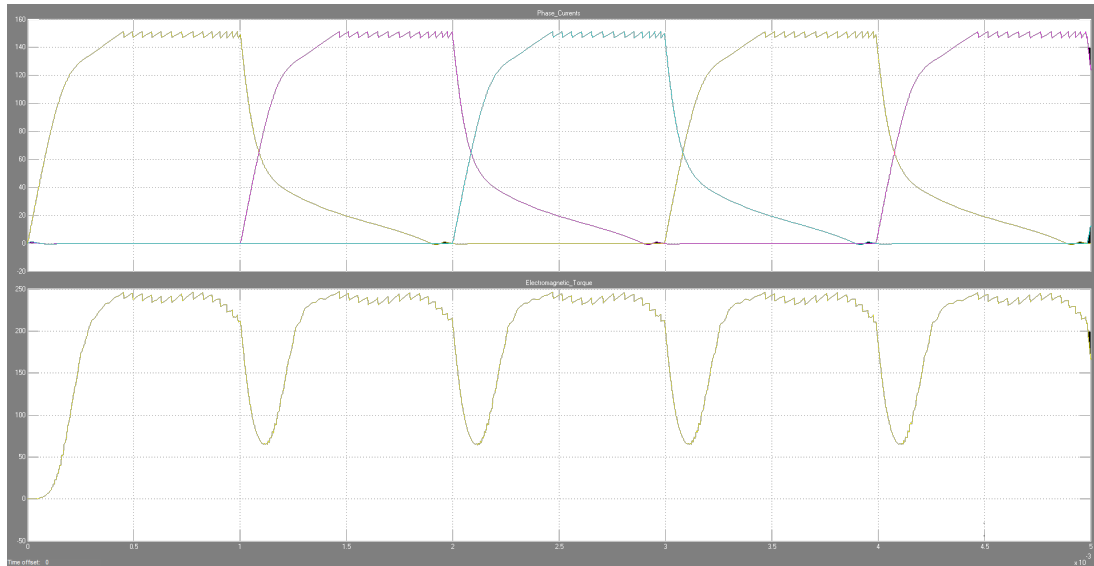


Figure 6.12: Simulation results with the shaft rotating at 2500 RPM

The simulation was repeated but this time with the initial speed of 300 rotations per minute and the results are presented in figure 6.13.
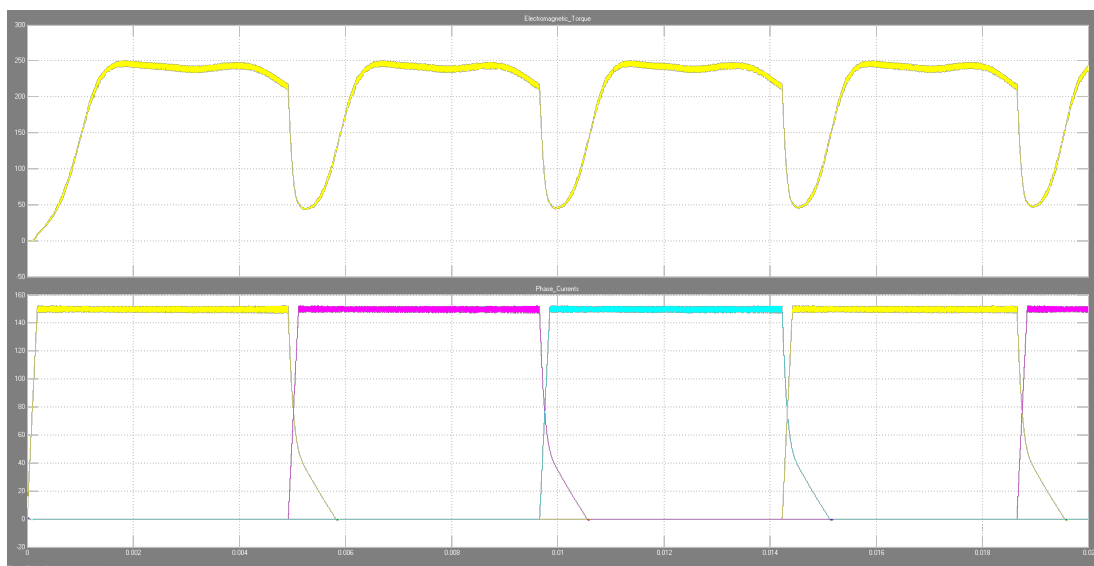


Figure 6.13: Simulation results with the shaft rotating at 300 RPM

## 6.3    Controller

With the electric motor drive model validated the next step is the development of a controller with the goal of reducing the torque ripple.

As revised in chapter 4, the control scheme is dependent on the motor speed. At low speeds there are small changes made to the turn on, $\theta_{on}$, and turn off, $\theta_{off}$, angles and it is possible to control the instantaneous torque by current chopping, however at high speed operation current chopping becomes harder to realise and only the average torque can be controlled.

Considering that the final goal of the dissertation was the development of an electric motor drive for traction with the lowest ripple possible, the controller was designed for low speed operation and the control scheme diagram developed is illustrated in figure 6.14.

### 6.3.1    Switching Angle controller

This subsystem is assigned with the task of computing the turn of and turn off angles. Their computation is done according to the relationships of the angles with the DC link voltage, reference current, shaft speed and minimum inductance presented in chapter 4. Considering that most the these variables maintain their value throughout the simulation and the only time changing variables are the reference current and shaft speed, the subsystem inputs and outputs are reference current and shaft speed.

### 6.3.2    Torque sharing function

The torque sharing function block is responsible by the distribution of torque production by the three phases. As stated in chapter 4, the TSF parameters are the torque reference, turn on angle, overlap angle and turn off angle.

### 6.3.3    Current Reference

In order to convert the reference torque into the controlled variable, which is the current, the next block makes use of the pre defined look up tables of the motor characteristics to do so. As to perform this action, the input variables are the rotor position and the reference torque for each phase.

### 6.3.4    Current Controller

The output torque is achieved via current state variable, this subsystem is must ensure that the current flowing trough the motor windings equals the current reference provided by the previous block thus controlling the motor output torque.
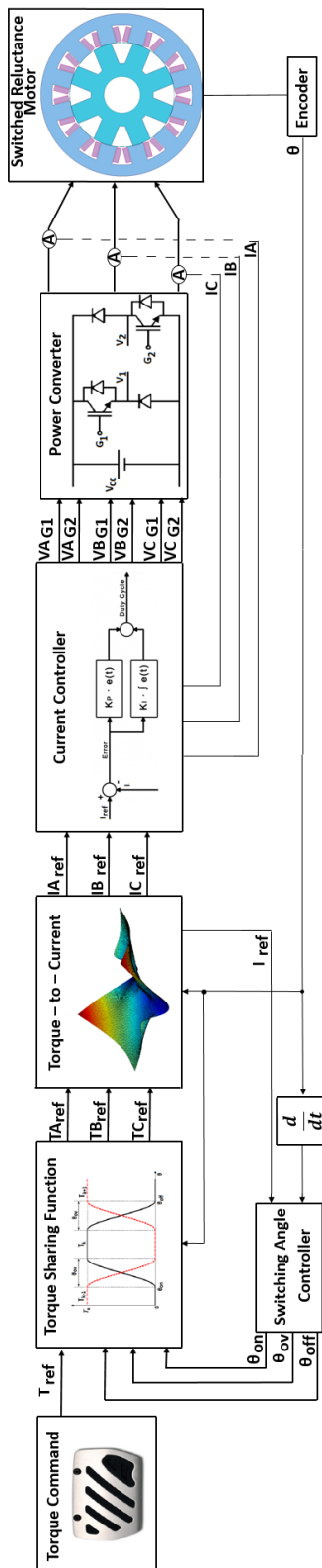
Figure 6.14: Control diagram of proposed controller

### 6.3.5   Simulink implementation

The above controller was implemented in Simulink as is shown in figure 6.15.
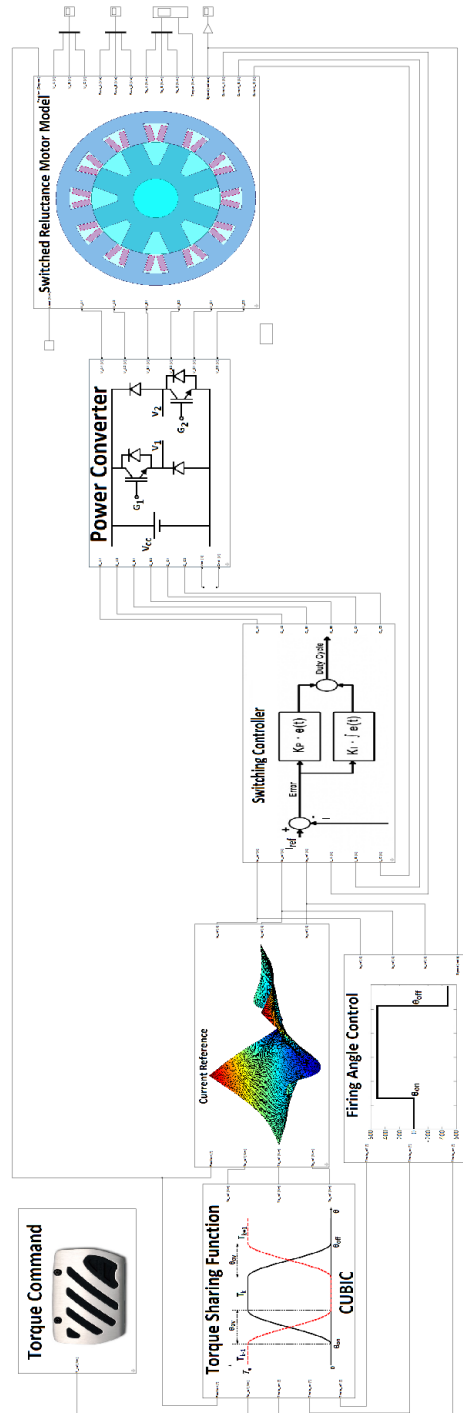
Figure 6.15: Simulink diagram of the developed controller

## 6.4   Simulation results

In the following results the power converter switching frequency is 10kHz. At very low speeds, 500 RPM, and low speed, 1500 RPM, for a reference torque of 230 Nm with cubic TSF, the output torque is shown in figure 6.16 and 6.17
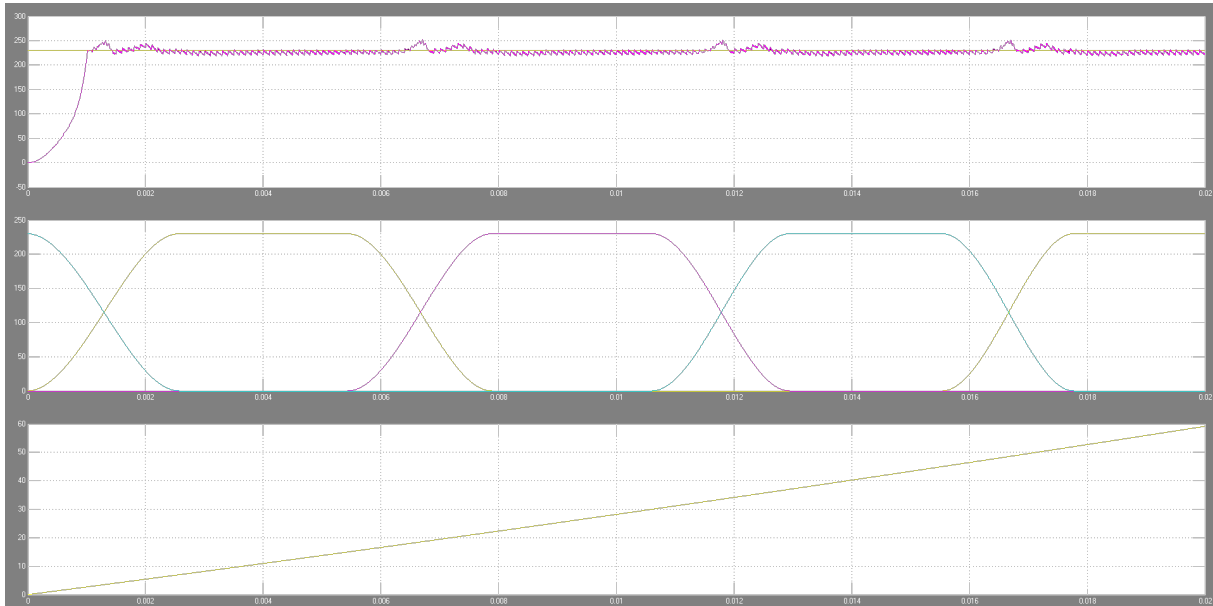


Figure 6.16: Cubic torque sharing function simulation at 500 RPM
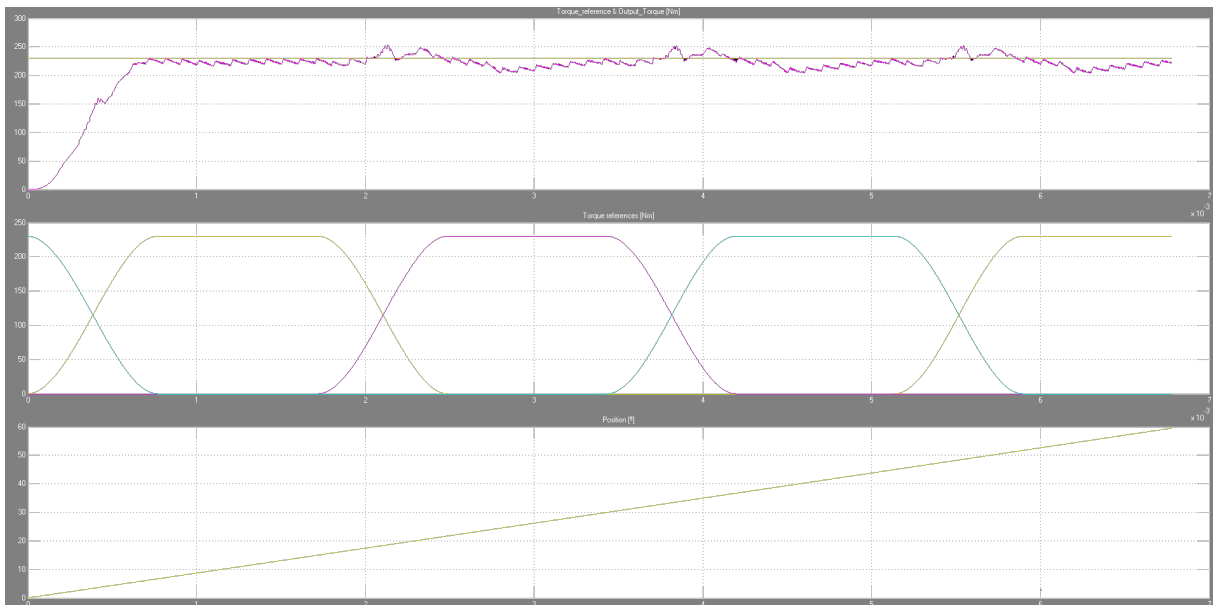


Figure 6.17: Cubic torque sharing function simulation at 1500 RPM

At rated speed, 2500 RPM, and rated torque as a reference, the output torque is present in figure 6.18.
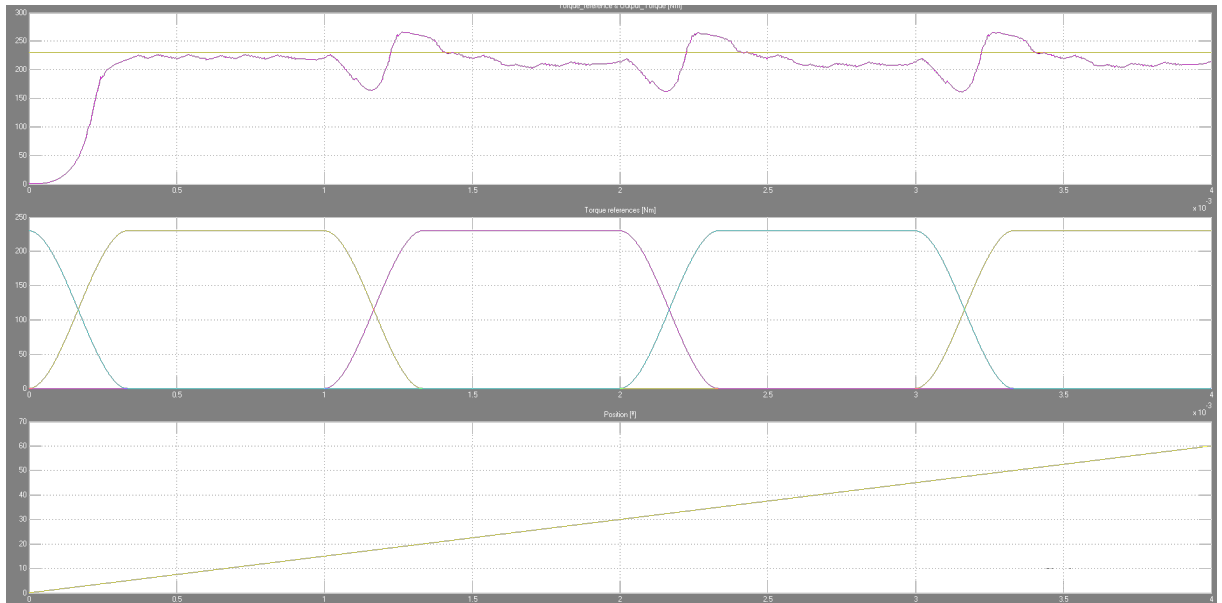


Figure 6.18: Cubic torque sharing function simulation at 2500 RPM

For each of the above simulations the torque ripple is present in table 6.1.

Table 6.1: Torque at low speed operation with diferent torque sharing functions

|          | $T_{average}$ | $T_{max}$ | $T_{min}$ | $T_{ripple}$ |
|----------|---------------|-----------|-----------|--------------|
| 500 RPM  | 229           | 251       | 219       | 13.9%        |
| 1500 RPM | 225           | 253       | 204       | 21.7%        |
| 2500 RPM | 217           | 265       | 161       | 47.9%        |

## 6.5   Conclusion

In this chapter the design of a model of the motor for the simulation is accomplished as well as the development of a control strategy based on the control schemes presented in chapter 4. The results obtained were satisfactory and the main goal of the dissertation was achieved, that is the development of a SRM drive with low torque ripple.

# Chapter 7

# Experimental verification

## 7.1 Introduction

Having the motor designed simulated and built the next step is the experimental validation of both the control scheme and the motor performance.

In the following chapter the necessary steps for the experimental verification are taken. For the experimental procedure the selection of semiconductors is needed as well as the dc-link capacitor and the voltage and current sensors. These need to be assembled in a heat sink that must be capable of dissipating the power loss generated during the motor operation.

With the power electronics components assembled, only the control unit needs to realized. A microcontroller capable of executing the algorithm needs to be selected and an interface between the power unit and control unit is required.

## 7.2 DC-link capacitor

The DC link capacitor provides a buffer for power transfer between the converter and DC power source. In switched reluctance drives since the flux linkage needs to be rebuilt from zero in every cycle a big part of the energy is going back and forth from the motor to the power source, resulting in a high current ripple for the capacitor. The ability to handle ripple current is one of the main criteria when selecting DC-link capacitors. There are some approaches for reducing the current ripple and therefore lessen the constraints on the capacitor [60].

The first step in sizing capacitors for bus link applications is to understand how capacitance is required for a given inverter design. An excessive amount of bus link capacitance can also present some safety concerns, considering that once the motor is turned off, a large amount of energy is still stored in the bus link capacitor.

The commonly used DC-link capacitors are the electrolytic capacitor and film capacitor. The main advantage of electrolytic capacitors are its large capacitance at high nominal voltages. However electrolytic capacitors needs to pay at least twice the price and reducing the half power or reducing the half load in lower temperature to ensure the reliable operation of the system [63].

The typical requirements for a DC-link capacitor in an automotive traction application is presented in figure 7.1.
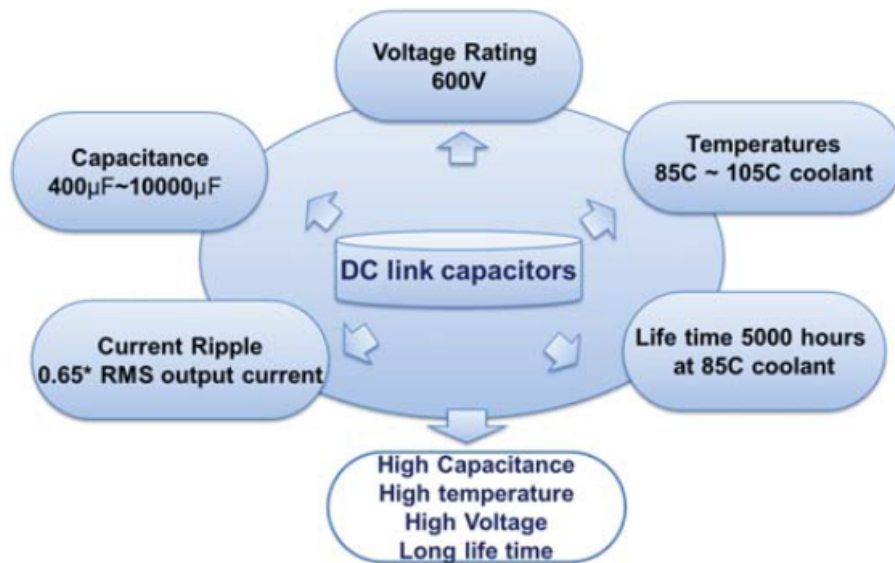


Figure 7.1: Specifications for the DC link capacitor for a typical automotive traction SRM drive [62]

The equivalent series resistor, ESR, should be as low as possible in order to minimize the losses. Seeing that the power converter will have its switching frequency in the range of some kHz, the equivalent series inductance, ESL, must be as low as possible, in the range of a few nH, as to not generate voltage spikes in the bus.

Recalling the energy conversion ratio (Q) defined in chapter 2

$$Q \quad = \quad \frac{converted\ \ energy}{energy\ \ supplied} \quad = \quad \frac{W_c}{W_f + W_c} \tag{7.1}$$

Usually SRM with regular air gap lengths have an energy conversion factor above 0.7, therefore the average magnetization energy, $W_f$, that flows back of the phase during demagnetization can be estimated as

$$W_f = T_n \cdot \frac{1 - Q}{Q} \cdot \frac{2 \cdot \pi}{N_r \cdot N_{ph}} \tag{7.2}$$

Once the magnetic energy is calculated, the minimum DC-link capacitance can be derived

$$C_{min} = \frac{2 \cdot W_f}{V_{dc}} \quad [F] \tag{7.3}$$

The capacitor selected for the DC-link power supply has the following characteristics, and is presented in figure 7.2.

Table 7.1: Electrical characteristics of 947D601K901DCRSN

| Parameter | Symbol | Value | Units |
|---|---|---|---|
| Rated voltage | $V_R$ | 900 | V |
| Capacitance | C | 600 | $\mu$F |
| Maximum RMS current | $I_{RMS}$ | 83 | A |
| Equivalent series resistor | ESR | 0.9 | m$\Omega$ |
| Equivalent series inductance | ESL | 35 | nH |



Figure 7.2: Power supply capacitor

## 7.3   Semiconductors

The power converter is formed by an asymmetric H-bridge for each motor phase, thus three asymmetric H-bridges must be assembled. Nowadays only two types of switches are used, namely IGBTs and MOSFETs. The DC-link voltage is too high for MOSFETs therefore IGBTs were used.

The requirements for the semiconductors are essentially the collector emitter voltage rating and their current, keeping in mind that the collector emitter resistance should be as low as possible as to reduce power losses. For the voltage rating the double of the DC-link voltage was dictated and for the current rating the peak motor corrent with a security factor of 20%.

Each asymmetric H-bridge is composed by modules, namely SEMiX302GAL12E4s and SEMiX302GAR12E4s presented in figure 7.3.
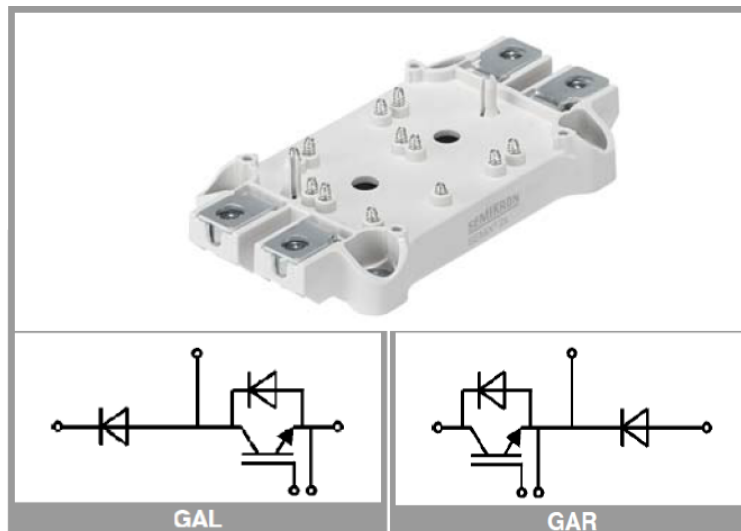


Figure 7.3:   Power semiconductors chosen to compose the asymmetric H-bridge Left:SEMiX302GAL12E4s schematic, Right:SEMiX302GAR12E4s schematic

To ease the physical connections between the gate signals and the modules a printed circuit board was designed and is shown on figure 7.4.

The modules characteristics are presented in table 7.2.

## 7.4   Converter losses

As revised earlier in Chapter 3, three different switching states can be distinguished for the power electronic devices assuming an asymmetric H-bridge supplying the SRM.

- Magnetization mode
- Freewhealing mode
- Demagnetization mode
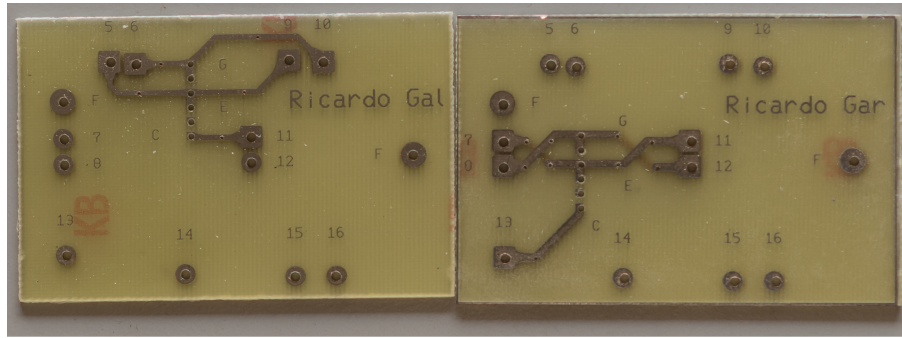
Figure 7.4: GAR GAL interface modules

Table 7.2: Electrical characteristics of SEMiX302GAL/GAR12E4s

| Parameter | Symbol | Value | Units |
|---|---|---|---|
| **IGBT** | | | |
| Collector emitter voltage | $V_{CES}$ | 1200 | V |
| Nominal collector current | $I_C$ | 356 | A |
| Gate emitter voltage | $V_{GES}$ | $\pm$ 20 | V |
| Collector emitter saturation voltage | $V_{CE}$ | 1.8 V @ 300 A | V |
| Collector emitter resistance | $R_{CE}$ | 3.3 @ $T_j$=25°C | m$\Omega$ |
| Gate internal resistance | $R_{Gint}$ | 2.50 | $\Omega$ |
| Turn-on switching energy | $E_{on}$ | 30 @ $I_c$=300 A $V_{CE}$=600 V $R_{G(on)}$=1.9$\Omega$ $V_{GE}$=+15V | mJ |
| Turn-off switching energy | $E_{off}$ | 44 @ $I_c$=300 A $V_{CE}$=600 V $R_{G(off)}$=1.9$\Omega$ $V_{GE}$=-15V | mJ |
| Gate charge | $Q_G$ | 1700 | nC |
| Maximum junction temperature | $T_{j(max)}$ | 175 | °C |
| Minimum junction temperature | $T_{j(min)}$ | -40 | °C |
| **Free-Wheeling Diode** | | | |
| Nominal current | $I_F$ | 266 $T_c$=80° | A |
| Forward voltage drop | $V_F$ | 2.1 @ 300 A $T_C$=25°C | V |
| Reverse recovery charge | $Q_{rr}$ | 50 | $\mu$C |
| Forward resistance | $R_F$ | 2.8 @ $T_j$=25°C | m$\Omega$ |
| Maximum junction temperature | $T_{j(max)}$ | 175 | °C |
| Minimum junction temperature | $T_{j(min)}$ | -40 | °C |

It is assumed a switching strategy like the one present in Fig 3.8, so the anti-parallel diodes do not conduct, consequently there is no loss on their part.

The total converter losses, $P_{total_{conv}}$, are given by the sum of switching losses and conduction losses.

$$P_{total_{conv}} = P_{cond} + P_{sw} \ [W] \tag{7.4}$$

### 7.4.1   Conducting losses

If one switch in the converter is in the conducting state, a forward voltage drop occurs due to the finite resistance of the power electronic devices. The resulting losses depend on the forward voltage $V_F$ and the junction temperature of the semiconductors. The conduction loss does not dependent on frequency, it only depends on duty cycle. The equation to calculate the conduction loss of a IGBT is given by [64].

$$P_{cond_{IGBT}} \quad = \quad V_{CE} \cdot <I_{IGBT}> + I_{RMS_{IGBT}}^2 \cdot R_{CE} \quad [W] \tag{7.5}$$

Where the $R_{CE}$ is the collector emitter resistance of the IGBT, $I_{RMS_{IGBT}}$ the root mean square of the current that flows through the switch and $<I_{IGBT}>$ the average current.
The diode conduction loss is another major conduction loss term in a converter.

$$P_{cond_{Diode}} \quad = \quad <I_D> \cdot V_F + I_{RMS_{Diode}}^2 \cdot R_F \quad [W] \tag{7.6}$$

With $<I_D>$ being the average current through the diode and $V_F$ the diode forward drop, $R_F$ the forward resistance and $I_{RMS_{Diode}}$ the mean square current on the diode.

### 7.4.2   Switching losses

These are the losses associated with the transition of the switch from its ON state to its OFF state, and vice versa. The higher the switching frequency, the greater the number of times the switch changes its state per second. Therefore these losses are proportional to the switching frequency [65].

There is an unavoidable voltage and current overlap during every switching transition. That overlap occurs because the inductor keeps trying to force current and tries to create suitable conditions for that to happen. The crossover period depends on the time it takes for the internal capacitances of the IGBT to charge or discharge, so the choice the gate resistor greatly impacts the switching losses.

In a switch with an ideal inductor, the switching loss is given by

$$P_{sw_{IGBT}} \quad = \quad V_{dc} \cdot I_p \cdot f_{sw} \cdot t_{cross} \quad [W] \tag{7.7}$$

The diode switching losses reside mainly on the turn-off losses, the turn-on energy losses are so small that they can be neglected. These depend on the reverse recovery time $t_{rr}$ which is the time necessary to remove the recovery charge $Q_{rr}$, until the diode can overtake the cut-off voltages V. Making the switching losses by the diode equal to

$$P_{sw_{Diode}} = f_{sw} \cdot V \cdot Q_{rr} \ [W] \tag{7.8}$$

Making use of the equations derived earlier in chapter 3, 3.2 and 3.2, using the values available in the Table 7.2, and assuming a switching frequency of 20 kHz, it is possible to derive the total power losses on the converter.

## 7.5 Heatsink

With the power components selected, the power converter can be assembled but the components must be placed close as possible in order to minimize the parasitic elements originated due to the connections. Given that the power losses are not irrelevant a proper heat sink is required. Normally the heat sink is designed in order to maximize its surface area in contact with cooling medium. As of the writing of this dissertation, the heat-sink was not yet assembled. Nonetheless the components placement is already prepared via solidworks and can be seen in figure 7.5.



Figure 7.5: Cad of heat sink

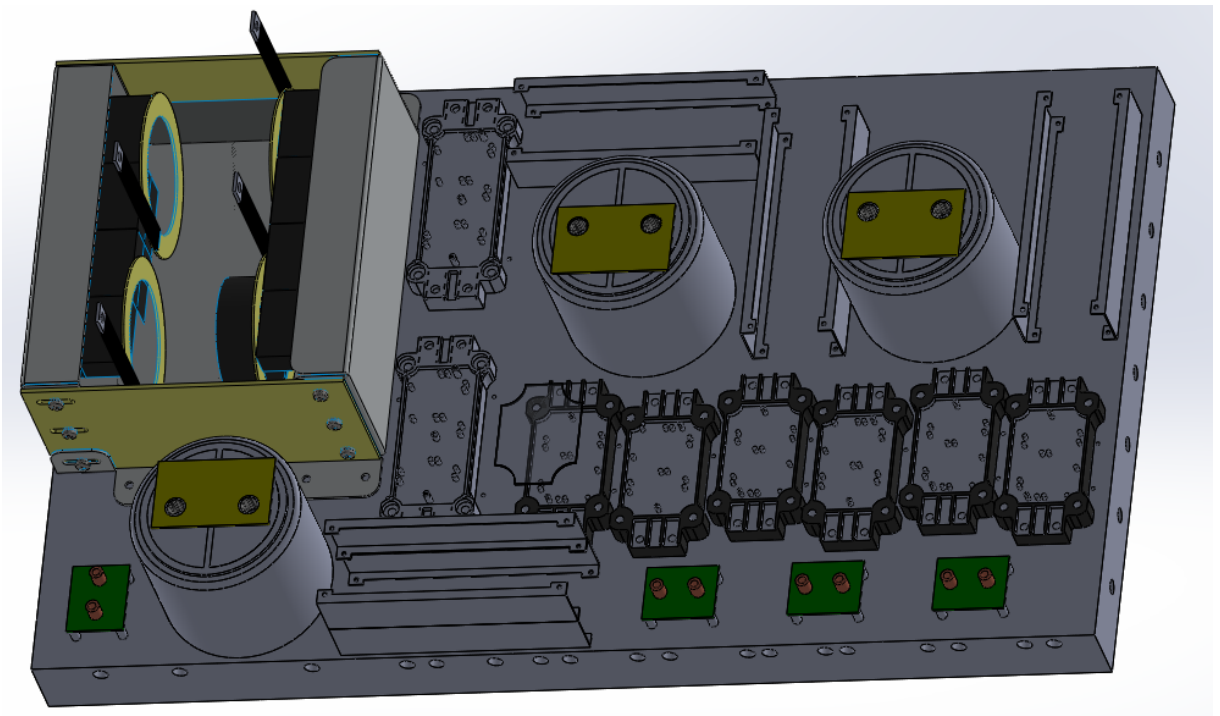The figure above contains more components than the ones needed to build three asymmetric H-bridge converters. The extra elements present in figure 7.5, such as the inductor and semiconductors are for the necessary power converter that will regulate the 600 V on the dc link. There are no mentions throughout the dissertation of this converter because unfortunately there was not enough time to finish it.

## 7.6   Drivers

In order to provide the galvanic insulation between the low power input provided by the micro-controller and the output signal with sufficient high current for the IGBT, a gate driver is needed.

The maximum average output current of the driver must be higher than the calculated value

$$I_{OUT(avg)} = f_{sw} \cdot Q_G \tag{7.9}$$

The driver must be able to provide the necessary gate current $I_G$. The output capacitors of the driver must be able to deliver the gate charge, $Q_G$, needed to charge and discharge the IGBT therefore

$$Q_{out/pulse} > Q_G \tag{7.10}$$

The driver must also be able to withstand the dc-link voltage, and dv/dt capability. With all of the above specifications, it was opted to use the *2SC0108T2A0-17*.

Table 7.3: 2SC0108T2A0 characteristics

| Parameter | Symbol | Value | Units |
|---|---|---|---|
| Supply Voltage | $V_{CC}$ | 15 | V |
| Gate peak current | $I_{out}$ | $\pm 8$ | A |
| Minimum external gate resistance | $R_{Gmin}$ | 2 | $\Omega$ |
| Typical internal resistance | $R_{G(int)}$ | 0.5 | $\Omega$ |
| Output power | $P_o$ | 1 | W |
| Switching frequency | $f_{sw}$ | 50 | kHz |
| Operating voltage | $V_{peak}$ | 1700 | V |
| Turn-on delay | $T_{d(on)}$ | 90 | ns |
| Turn off delay | $T_{d(off)}$ | 90 | ns |
| Turn-on voltage | $V_{G+}$ | 15 | V |
| Turn off voltage | $V_{G-}$ | -7.6 | V |
| Minimum operating ambient Operating Temperature | $T_{Min}$ | -20 | °C |
| Maximum operating ambient Operating Temperature | $T_{Max}$ | 85 | °C |



Figure 7.6: 2SC0108T2A0 module

However the module in the above figure is only an element of a two piece kit that compose the driver. The other component *2BB0108T2A0-17* is no longer available and in order not to waste the money that had already been spent on the module it was necessary to build the base board. The first prototype is of the base board is presented in figure 7.7.
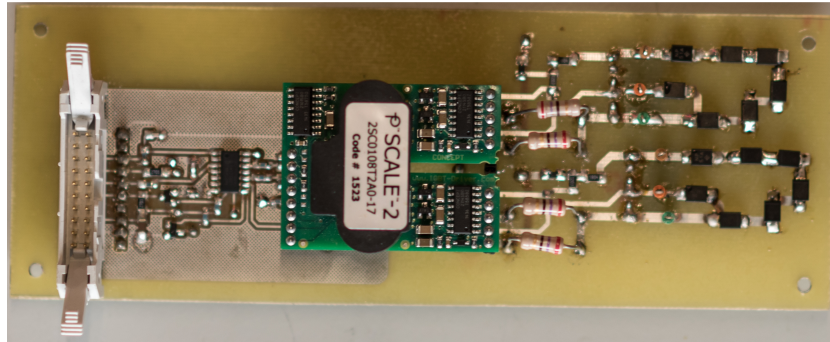


Figure 7.7: Base board prototype

After testing and validating the driver a few more boards were printed and the final version of the base board is shown in figure 7.8 and the board assembled in figure 7.9.
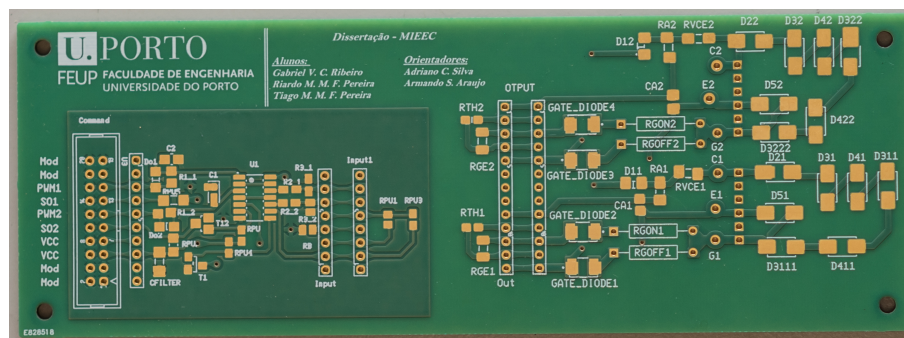


Figure 7.8: Final version of the base board
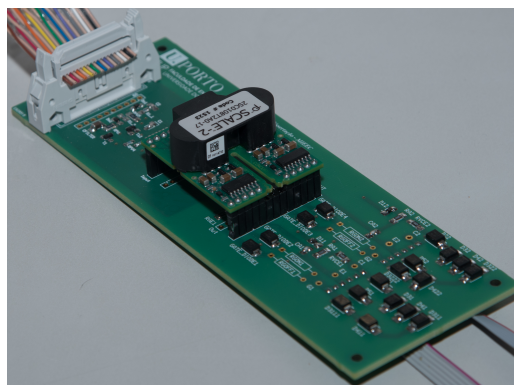


Figure 7.9: Base board assembled

### 7.6.1   Gate Resistor

The IGBT on/off status is defined by its gate voltage. The charging and discharging current is limited by the gate resistor $R_g$. The gate resistor influences the IGBT switching time, and therefore dv/dt and di/dt which in turn affect the electromagnetic interference (EMI), switching losses, reverse recovery current on the free wheeling diode and short-circuit safe operating area [66].
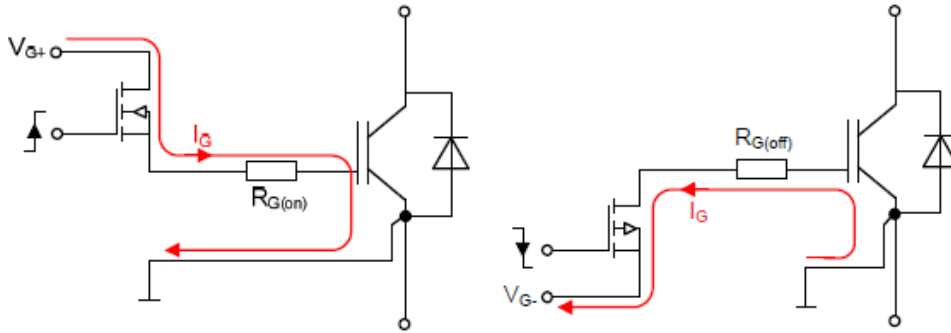


Figure 7.10: Turn on gate current and turn off gate curent

The gate resistance is the series sum of the gate driver impedance, the physical gate resistor and the internal gate resistance. The charging and discharging current must be lower than the peak current allowed for the drivers *IG_peak*.

$$I_{G(on)\_peak} = \frac{V_{G+} - V_{G-}}{R_{Gon}} \quad [\Omega] \tag{7.11}$$

$$I_{G(off)\_peak} = \frac{V_{G+} - V_{G-}}{R_{Goff}} \quad [\Omega] \tag{7.12}$$

$$I_{G(on)\_peak} < IG_{peak} \quad [A] \tag{7.13}$$

Therefore the minimum gate resistance is given by

$$R_{Gmin} = \frac{V_{G+} - V_{G-}}{I_{G\_peak}} \tag{7.14}$$

Given that the resistance has to withstand substantial peak current although for brief periods of time, its power rating has to be taken into account. A typical gate current wave form is presented in figure 7.11.
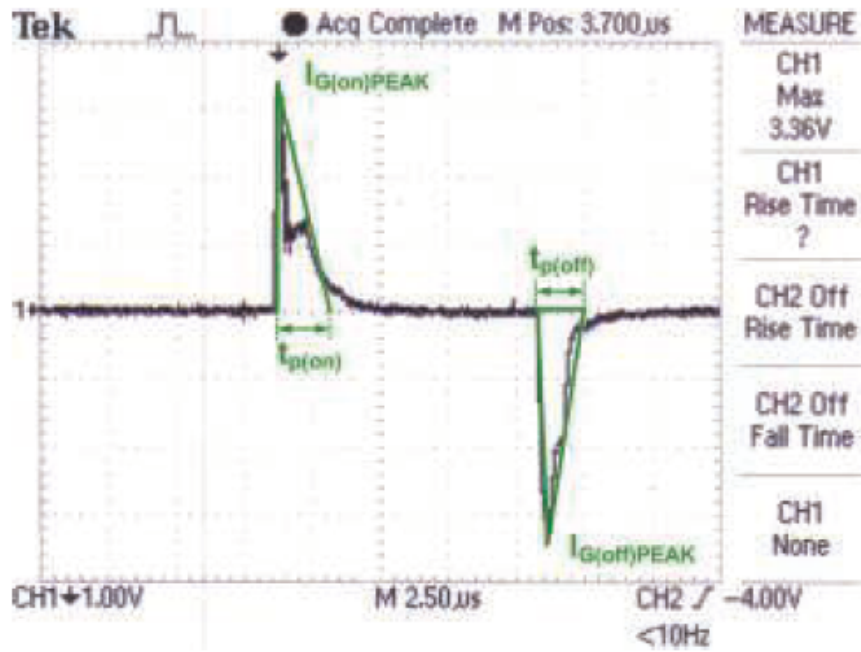
Figure 7.11: Gate current waveform [66]

$$I_{G(on)RMS} = I_{G(on)peak} \cdot \sqrt{\frac{K}{3}} \quad [A] \tag{7.15}$$

Where

$$K = \frac{t_p}{T} = t_p \cdot f_{sw} \tag{7.16}$$

Therefore the power dissipated by the turn on resistor is

$$P_{G(on)} = I^2_{G(on)RMS} \cdot R_{G(on)} \tag{7.17}$$

Generally speaking, with higher gate resistance value, the switching speed of the power device will decrease. This means the switching loss will be increased as illustrated in Figure 4 as an example. This in turn will finally influence the efficiency. In contrast, when a lower gate resistance is applied, the switching will become faster which can reduce the switching loss. Meanwhile, the noise induced by di/dt and dv/dt will increase with higher switching speed.

## 7.7   Encoder

The excitation of the switched reluctance motor phases needs to be carefully synchronized with rotor position to obtain an acceptable drive performance, therefore rotor position sensing is an integral part of the SRM drives control. Additionally, for precise torque and speed control applications, it is necessary to have rotor position information with reasonably good resolution and high degree of accuracy. For the dissertation the *RSI 58H* encoder was bought and its characteristics are presented in table 7.4.

Table 7.4: RSI 58H 7951144 characteristics

| Parameter | Value | Units |
|---|---|---|
| Input Voltage max | 30 | V |
| Input Voltage min | 10 | V |
| Pulses per revolution | 5000 | - |
| Max pulse frequency | 200 | kHz |
| Max operating speed | 6000 | RPM |



Figure 7.12: RSI 58H

## 7.8   Control Unit

In order to implement the control scheme simulated in the previous chapter a microcontroller is needed.

The microcontroller must be able to execute the control algorithm at a 10 kHz frequency, therefore every 100 $\mu$s it must read the current value of each motor phase and update the PWM of the corresponding asymmetric half bridge.

Although it was not addressed in the dissertation, there is a plan to eventually implement a converter between the motor power converter and the battery pack. The topology of said converter is composed of two half-bridges and therefore the microcontroller needs an extra four PWM channels and four ADC's, three for voltage sensors and another one for a current sensor.

As to make the motor driver complete, the command for the torque value should be able to change dynamically with a pedal like signal, thus another ADC is needed.

The control method also needs the rotor position, hence the microcontroller must decode the signals provided from the encoder and determine the shaft position.

### 7.8.1 Microprocessor XMC-4500

The power electronics research group has been using the XMC-4500 microcontroller for motor control. The board that is presented in figure 7.13 has some features that make it suitable for the application in question.
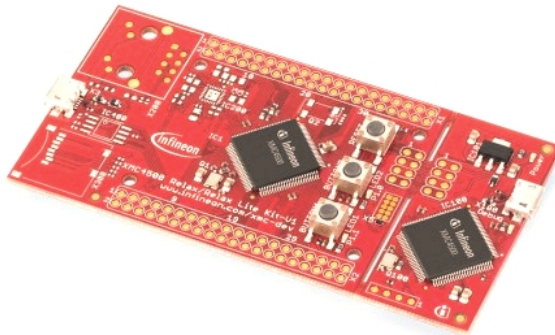


Figure 7.13: XMC-4500

The XMC-4500 device is a high performance and energy efficient microcontroller with a 32 bit ARM CPU. The board contains four analog digital converters groups of 12 bit resolution each with 8 channels, with the possibility of synchronous conversion between different ADC groups.

The also board possess a module specially designed for servo motor positioning, *POSIF* which simplifies the calculation of the rotor position.

For the PWM signals that are necessary for the control o both power converters, the device embody's a capture compare unit 8, also known as CCU8 that is designed specially for PWM signal generation and motor control.

## 7.9   Control board design

With the power converter designed and built, as well as the motor, an interface between the power unit and control unit is needed in order to link the two. The control scheme for the motor makes us of both voltage sensor and current sensor.

### 7.9.1   Voltage sensor

The voltage sensor chosen was the *ACPL-C87AT*, that with its high working voltage, bandwidth and temperature operating range combined with the small error and non linearity, makes it suitable for the application in question.

Table 7.5: ACPL-C87AT characteristics

| Parameter | Symbol | Minimum | Maximum | Units |
|---|---|---|---|---|
| Ambient Operating Temperature | $T_A$ | -40 | 125 | °C |
| Input Supply Voltage | $V_{DD1}$ | 4.5 | 5.5 | V |
| Input supply current | $I_{DD1}$ | 10.4 | 15 | mA |
| Output Supply Voltage | $V_{DD2}$ | 3.0 | 5.5 | V |
| Output supply current | $I_{DD2}$ | 6.5 | 12 | mA |
| Input Voltage | $V_{IN}$ | 0 | 2.0 | V |
| Nonlinearity | NL | 0.05 | 0.12 | % |
| Maximum Working Insulation Voltage | $V_{IORM}$ | - | 1414 | V |
| Input offset voltage | $V_{OS}$ | -10 | 10 | mV |
| Equivalent Input impedance | $R_{IN}$ | - | 1000 | MΩ |

The sensor provides isolation by making use of optical coupling technology, figure 7.14 presents the sensor functional diagram. The input supply voltage, $V_{DD1}$, and output supply voltage, $V_{DD2}$, are electrically isolated from one another.
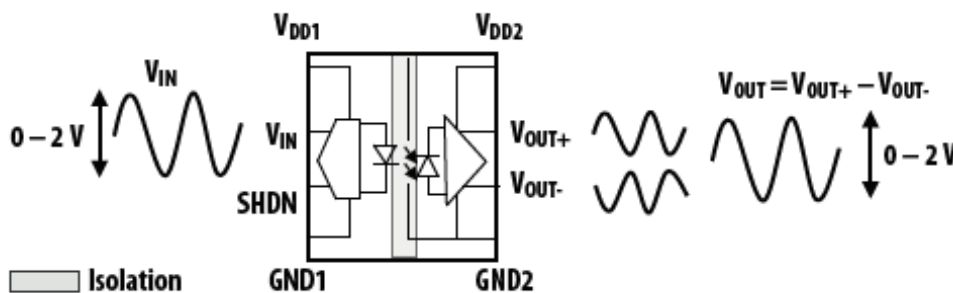


Figure 7.14: Voltage Sensor functional diagram

The motor was designed for a dc-link voltage of 600 V, as seen in chapter 3, the demagnetization energy of the outgoing phase causes a voltage increase in the dc-link, therefore taking into account these voltage spikes, a 650 V voltage reference was used to define the $R_1$ and $R_2$ resistors.

$$R_1 = 648 \quad [k\Omega] \tag{7.18}$$

$$R_2 = 2 \quad [k\Omega] \tag{7.19}$$

Based on the *ACPL-C87AT* datasheet, the following schematic was conceived.
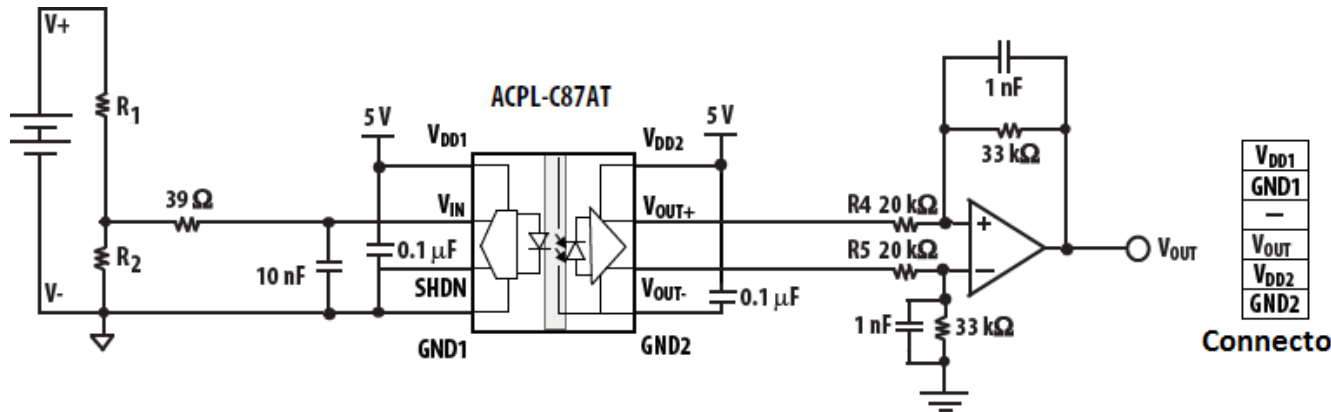


Figure 7.15: Voltage Sensor Schematic

To reduce the voltage stress of a sole resistor, $R_1$ was decided to be a series of 4 resistors, each with 162 kΩ. Each resistor needs to handle 162.5 V of voltage drop instead of 200 V and considering that only 1 mA current is flowing through them, a power rating of 250 mW the following resistor was selected.

Table 7.6: RP73D2B162KBTG 162 $k\Omega$ film resistor characteristics

| Parameter | Value | Units |
|---|---|---|
| Resistance | 165 | kΩ |
| Voltage rating | 200 | V |
| Power rating | 250 | mW |
| Tolerance | 0.1 | % |

The resistor tolerance is very low because the total system error is the sum of the voltage divider error and isolation amplifier error. The other passive components were selected with similar characteristics, however their voltage rating was not as critical, and therefore significantly lower.

The op amp necessary for the amplification of the differential signals provided by the voltage sensor needs TLV2470AIP

For the amplification of the differential signals originated from the voltage sensor, an op amp is needed. The requirements for such op amp are low off set voltage, a supply voltage compatible with the ACPL-C87AT and high differential input resistance. The following op amp was selected.

Table 7.7: Precision amplifier TLV2470AIP characteristics

| Parameter | Value | Units |
|---|---|---|
| Maximum supply voltage | 6 | V |
| Minimum supply voltage | 2.6 | V |
| Operating Supply Current | 900 | $\mu$ A |
| Output Current per Channel | 35 | mA |
| Input Offset Voltage | 1.6 | mV |
| Maximum Operating Temperature | 125 | °C |
| Minimum Operating Temperature | -40 | °C |
| Gain Bandwidth Product | 2.8 | MHz |
| Differential input resistance | $10^{12}$ | Ω |

The sensor makes use of two independent power supply's of 5 V each, as it will be addressed later the board which will host the microcontroller has 5 V and 12 V voltage levels, in order to attain the isolated supply of 5 V, an isolated buck dc-dc converter was used, namely the MEV1S1205DC.



| Order Code | Nominal Input Voltage | Output Voltage | Output Current | Input Current at Rated Load | Load Regulation (Typ) | Load Regulation (Max) | Ripple & Noise (Typ)[2] | Ripple & Noise (Max)[2] | Efficiency (Min) | Efficiency (Typ) | Isolation Capacitance | MTTF[3] | Package Style |
|---|---|---|---|---|---|---|---|---|---|---|---|---|---|
| | V | V | mA | | % | | mVp-p | | % | | pF | kHrs | |
| MEV1S1205DC | 12 | 5 | 200 | 98 | 4.6 | 5.5 | 11 | 20 | 80 | 84 | 34 | 6644 | DIP |

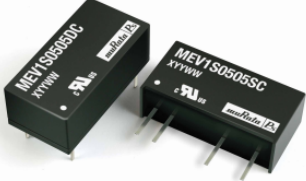Figure 7.16: Voltage Sensor function diagram

After testing the schematic in a breadboard, a printed circuit board was devised, the final voltage sensor prototype is shown in figure 7.17.
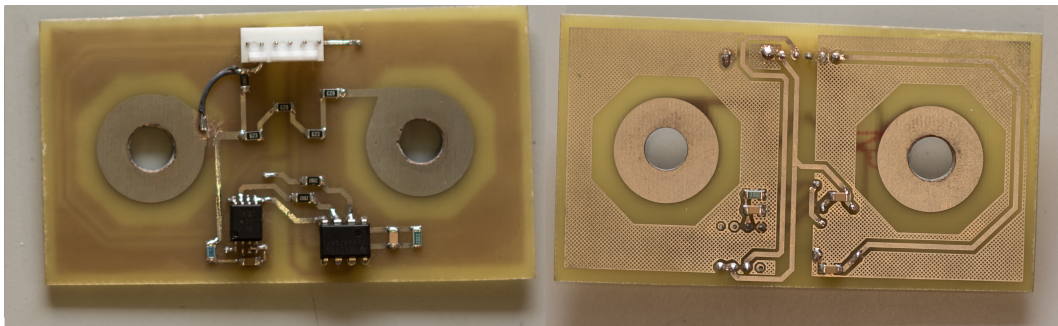
Figure 7.17: Voltage sensor printed circuit board

The printed circuit board was designed in a way that would fit in the dc-link capacitor as shown in figure 7.18.
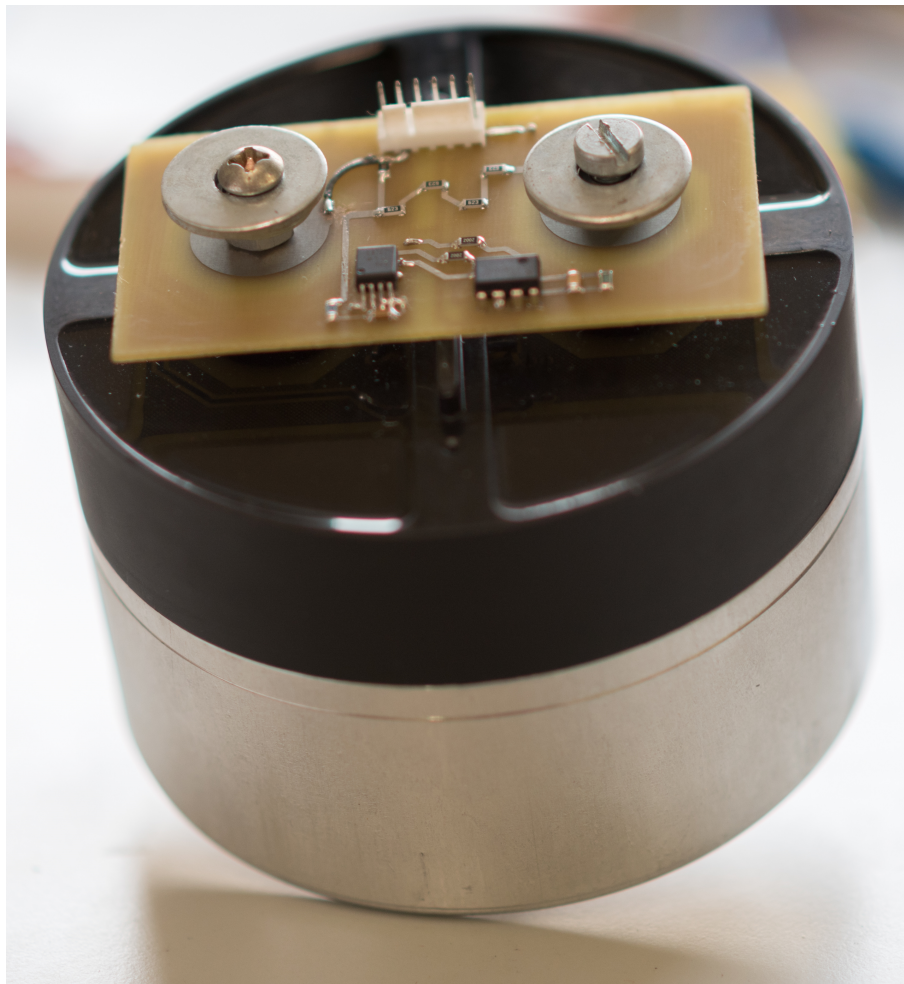


Figure 7.18: Voltage sensor printed circuit board

### 7.9.2   Current sensor

During the motor design, some simulations were performed with currents up to 200 A, the sensor
chosen for the experimental verification of the project was the *ACS759-200B*. Some of its features
makes it appropriate for the task, such as the high level immunity to current conductor dV/dt, low
conductor loss due to its small internal resistance, high bandwidth and low rise time which allows
a fast tracking of the current and small error.

Table 7.8: ACS759-200B characteristics

| Parameter | Symbol | Value | Units |
|---|---|---|---|
| Supply Voltage | $V_{CC}$ | 3.3 | V |
| Supply Current | $I_{CC}$ | 10 | mA |
| Sensitivity | $S_{ens}$ | 6.6 | mV/A |
| Primary sampled current | $I_P$ | $\pm\,200$ | A |
| Internal Bandwidth | $BW_i$ | 120 | 120 kHz |
| Electrical voltage off set | $V_{OE}$ | $\pm\,5$ | mV |
| Nonlinearity | $E_{LIN}$ | $<\pm\,1$ | % |
| Noise | $v_{NOISE}$ | 2 | mv |
| Total output error | $E_{TOT}$ | $\pm\,2$ | % |
| Minimum operating ambient Operating Temperature | $T_{Min}$ | -40 | °C |
| Maximum operating ambient Operating Temperature | $T_{Max}$ | 85 | °C |
| Rise time | $t_r$ | 3 | $\mu$s |
| Primary conductor resistance | $R_{PRIMARY}$ | 100 | $\mu\Omega$ |
| Quiescent Output Voltage ($I_P$= 0 A) | $V_{IOUT}$ | $\frac{V_{CC}}{2}$ | V |

The current sensor diagram and board is presented in figure 7.19.
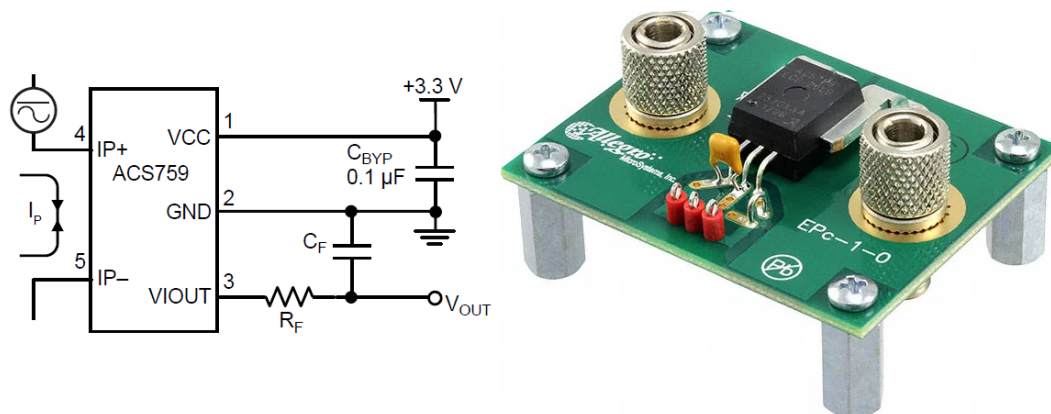


Figure 7.19: Current sensor diagram and board

The device measures bidirectional current providing an output voltage of $\frac{V_{cc}}{2}$ and has a negative
slope when an increasing current flows through the primary copper conduction path from terminal
5 to terminal 4, and a positive slope when the current flows from terminal 4 to 5.  Considering
that the motor winding is excited unidirectionally, in order to make full use of the microprocessor

ADC, a simple non inverting amplifier configuration was used. The op amp selected was again the precision amplifier *TLV2470AIP* for the same reasons as mentioned above.
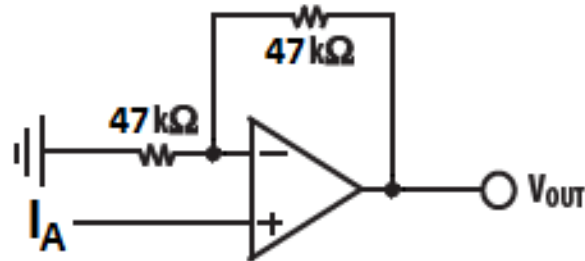


Figure 7.20: Voltage Sensor function diagram

### 7.9.3   User interface

The board will contain five drive connectors, three for each phase of the motor and two more for the buck boost that is expected to be developed. Each connector has the 15V supply for the drive, the two signals for the semiconductors and another two signals for fault detection. As stated earlier, one of the advantages of the drivers that were chosen are its ability to identify short circuits in the semiconductor and turning them off. When a fault occurs the driver module transmits to the corresponding status output, $SO_x$, a low signal (0 V). However when these signals output are high the voltage level needs to be adjusted and this is accomplished by using a voltage divider as shown in figure 7.21.
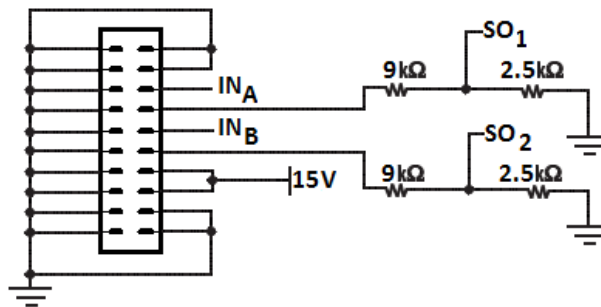


Figure 7.21: Schematic of the connector used in the control board for the drive

Where $IN_A$ and $IN_B$ are the signals that command to semiconductors.

Considering that there will be a total of ten semiconductors and simultaneous faults may occur, in order to identify where the failure occurred for each semiconductor there is an analog memory cell composed by two NAND gates that in case of failure light a LED. To make sure that the led stays on even after the driver status output signal goes high again, the led only turns off after the user presses the button *clear* that is presented in figure 7.22.
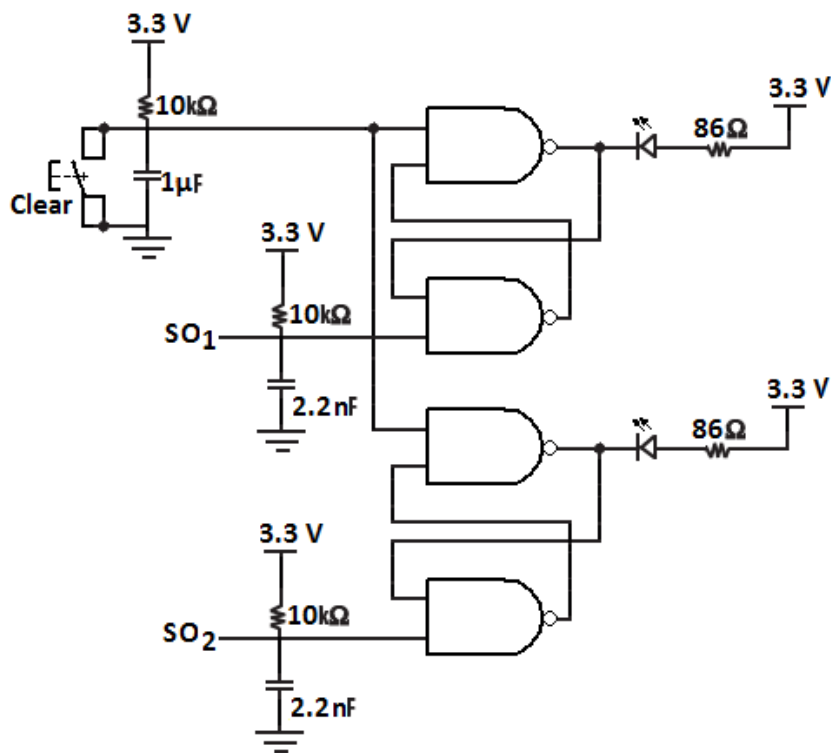
Figure 7.22: Schematic of the boolean circuit used for the fault diagonosis

After having a way to identify where the fault occurred, it is important that whenever a fault takes place the semiconductors stay turned off until a proper diagnosis is made, because the driver only turns the semiconductor off for a brief period of time. Therefore whenever a fault occurs, with a simple boolean circuit that is presented in figure 7.23 an error signal is generated.
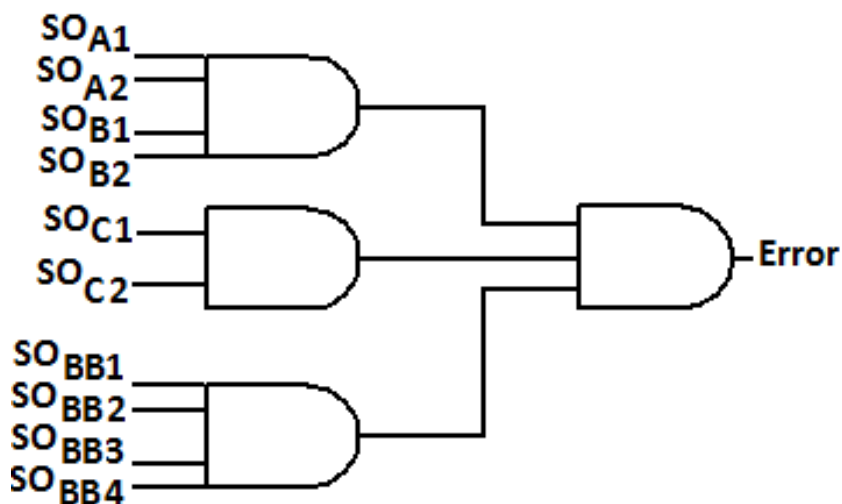


Figure 7.23: Schematic of the boolean circuit used to determine the Error signal

This signal is then feed into another logic circuit that generates an enable signal, and this stays

low even if the error signal changes its state to high again. This is achieved by making use of a D type flip flop, and the schematic is presented in figure 7.24.

If no error is detected then a green led is turned on, whenever a fault is detected a red led is turned on and the enable signal goes low. After a proper diagnosis is made, and no fault is being detected, error signal state is high, in order to make the enable signal state high the reset button must be pressed.
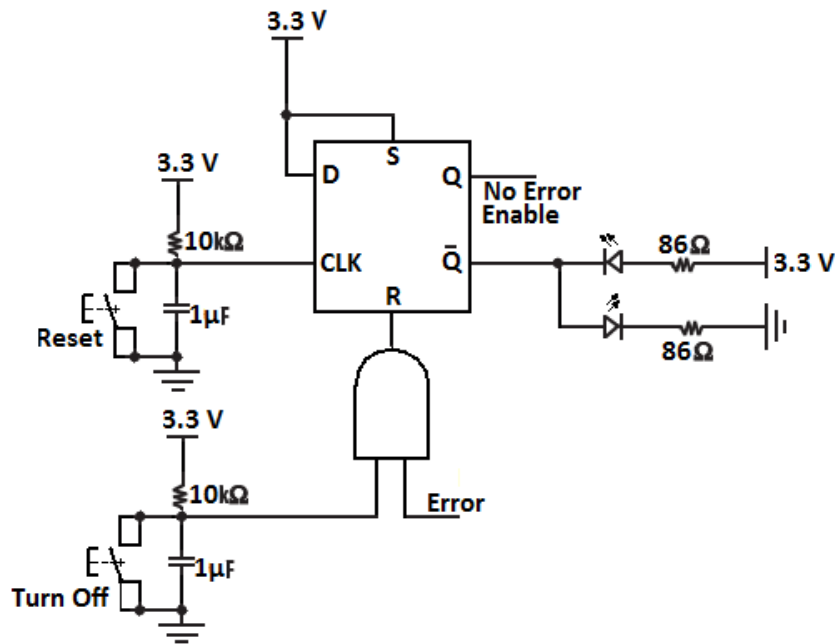


Figure 7.24: Electric shematic of the flip flop circuit

The enable signal that originates in the flip flop is then feed into an AND gate that finds the minimum between the enable and a signal that depends on the position of a toggle switch.



Figure 7.25: Enable for each phase of the motor

The simple boolean circuit that is presented in figure 7.25 prevents the power devices to be turned on in case of error and when the the toggle switch is in its off position. A led was added to the circuit in order to have visual feedback whenever the toggle switch is in a position that enables the power devices to be turned on. A replica of the above circuit was also designed for the buck boost power circuit. However considering that the topology for the buck boost that the author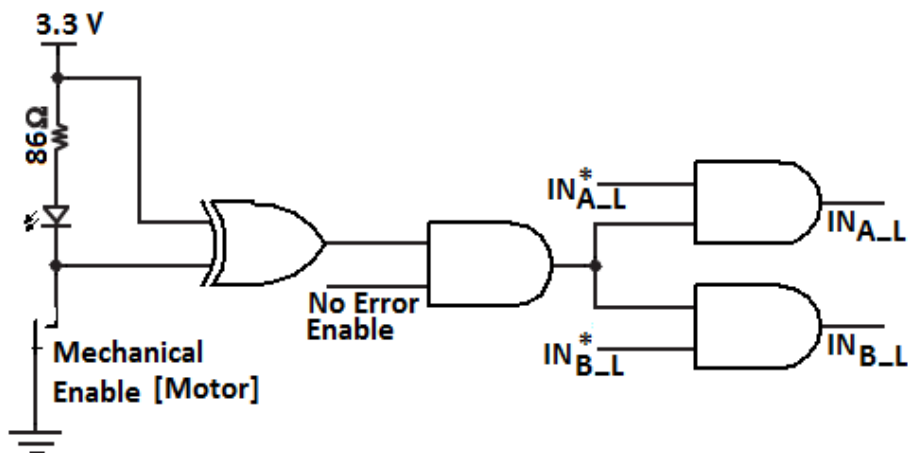 has in mind is composed by two half bridges, in order to avoid shoot-through fault, the two transistors of the half bridge cannot be closed at the same time. Therefore as to avoid the two transistors to be closed at the same time a XOR gate is used as shown in figure 7.26.
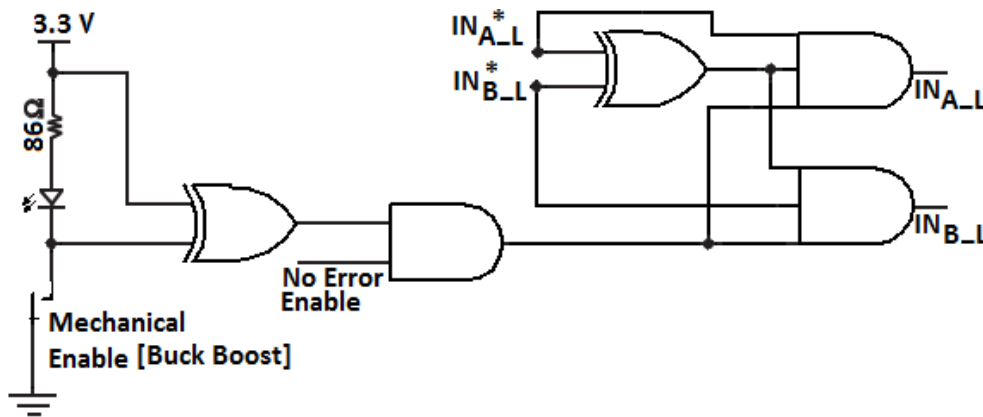


Figure 7.26: Enable for the buck boost half bridge

The preceding circuits made use of logic gates and the criteria used for their choice was essentially their propagation delay time, which had to be the lowest possible in order to achieve the lowest lag between the microcontroller signal and the semiconductor. An example of the gate integrated circuit used is presented in table 7.9.

Table 7.9: SN74LV21ADR logic gate AND with 4 input characteristics

| Parameter | Symbol | Value | Units |
|---|---|---|---|
| Supply Voltage - Max | $V_{CCmax}$ | 5 | V |
| Supply Voltage - Min | $V_{CCmin}$ | 5 | V |
| Input current | $I_{in}$ | 50 | mA |
| Output Current | $I_{out}$ | 12 | mA |
| Propagation Delay Time | $t_{pd}$ | 8.5 | ns |
| Minimum operating ambient Operating Temperature | $T_{Min}$ | -40 | °C |
| Maximum operating ambient Operating Temperature | $T_{Max}$ | 85 | °C |
| Number of Gates | | 2 | |
| Number of Input Lines | | 4 | |
| Number of Output Lines | | 1 | |

After all the boolean operations are applied to the $IN_A$ and $IN_B$ signals, these need to change their voltage level from 3.3V to 15V for the semiconductors drive, *2SC0108T2A0-17*, be able to accurately distinguish the LOW state from HIGH state. This change in voltage level was accomplished by the use of the integrated circuit *CD40109BE* and the schematic is depicted in figure 7.27.
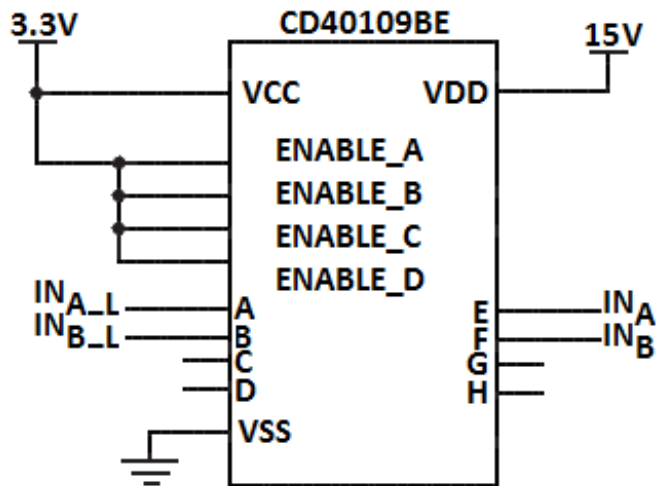


Figure 7.27: Electric schematic of the integrated circuit that changes the voltage level of the driver signals

Once again the criteria for the integrated circuit, IC, was the propagation time delay.

As a means to test the practical implementation of the control algorithm, the torque command needs to change overtime. The schematic illustrated in figure 7.28 portrays the two ways the torque can be commanded, initially for the first tests the torque can be increased or decreased with the use of two push buttons. Eventually when the algorithm is calibrated, the torque can be changed with a pedal like signal through the use of an ADC, therefore a connector for the command signal was included in the control board.
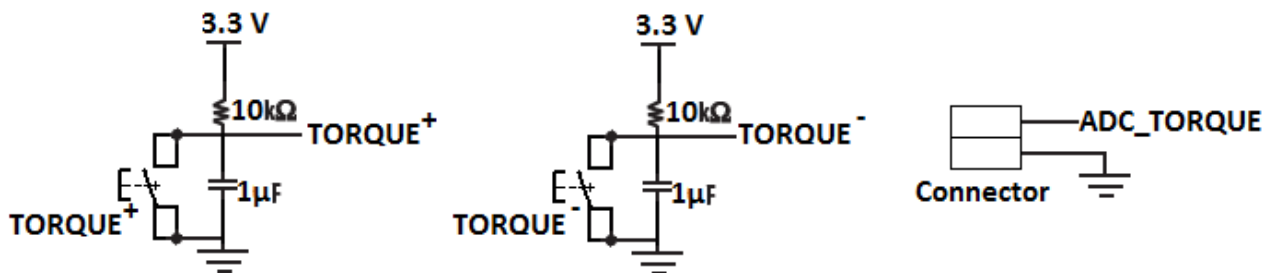


Figure 7.28: Electric schematic of the the torque command signal

The electric connection of the encoder with the control board is shown in figure 7.29. As observed earlier in the encoder characteristics table, the encoder can be powered by a 12V supply voltage and considering that the output signals voltage level is the same as the supply voltage, a voltage divider is necessary in order to reduce the signals *A*, *B* and *N* voltage to acceptable voltage level for the microcontroller.
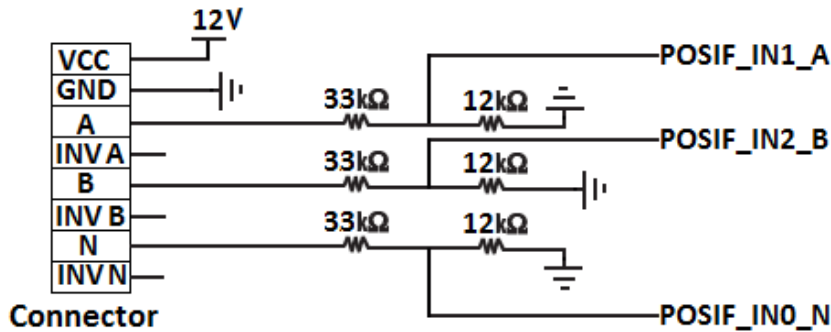


Figure 7.29: Encoder electric interface with the control board

The input output connections with the microcontroller are depicted in figure 7.30.
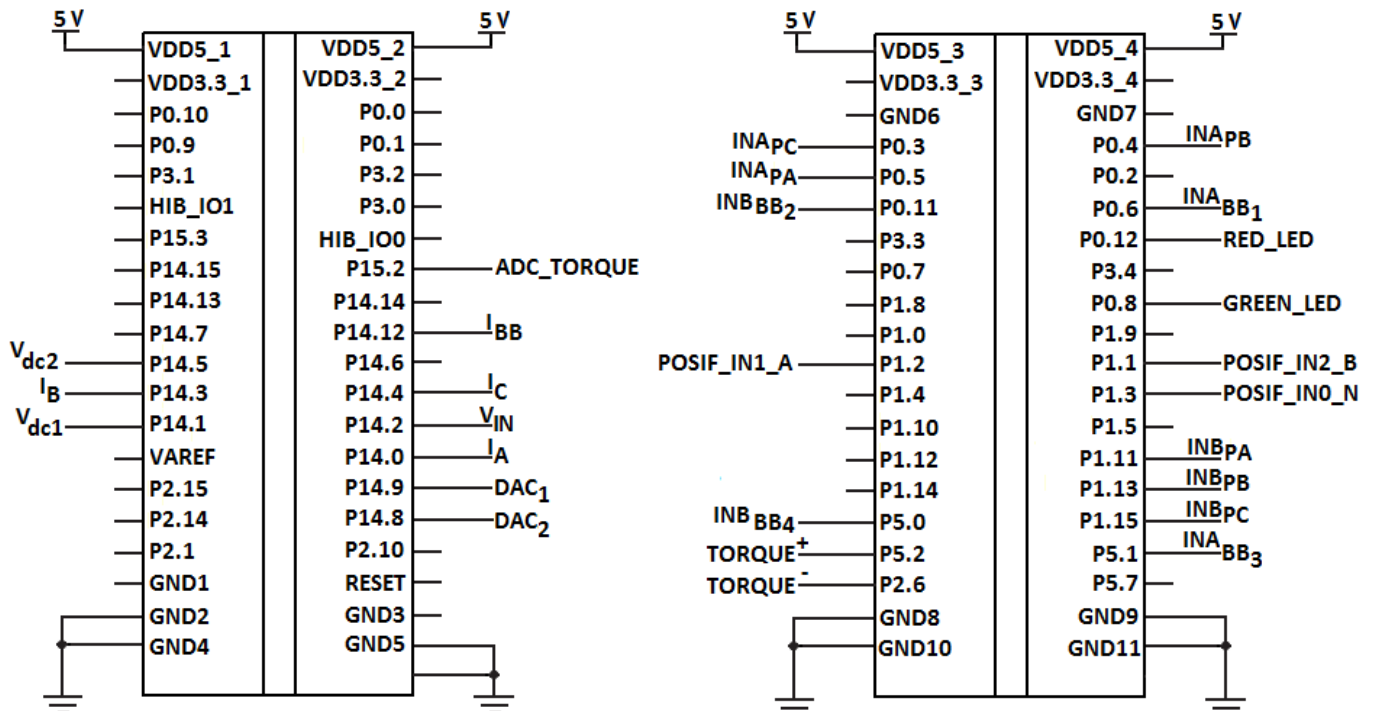


Figure 7.30: Connection

The XMC 4500 possess two digital to analog converter, DAC, outputs and these were connected to test points so that during the experimental validation some variables of the control algorithm could be accessed, for example the estimated average torque.

### 7.9.4 Power supply

The circuits necessary for the proper operation of the control board have different voltage levels, 3.3V, 5V, 12V and 15V respectively. The final goal of the dissertation is to have a switched reluctance drive for an electric vehicle. The electric car that the college possess still carry's its 12V battery, therefore the power supply of the control board was decided to be the battery.

The components that need a supply voltage of 15V are the semiconductor drivers and the integrated circuit that changes the voltage level of the $IN_A$ and $IN_B$ signals. The *LM2577T-15* is suitable for application and has the following features.

Table 7.10: LM2577T-15 characteristics

| Parameter | Symbol | Value | Units |
|---|---|---|---|
| Input Voltage - Max | $V_{CCmax}$ | 40 | V |
| Input Voltage - Min | $V_{CCmin}$ | 3.5 | V |
| Output Current | $I_{out}$ | 3 | A |
| Output Voltage | $V_{out}$ | 15 | V |
| Efficiency | $\eta$ | 80 | % |
| Load Regulation | $\frac{\Delta V_{OUT}}{\Delta LOAD}$ | 20 | mV |
| Minimum operating ambient Operating Temperature | $T_{Min}$ | -40 | °C |
| Maximum operating ambient Operating Temperature | $T_{Max}$ | 125 | °C |

The switching voltage regulator *LM2577T-15* requires a minimum number of external components and the schematic is depicted in figure 7.31.
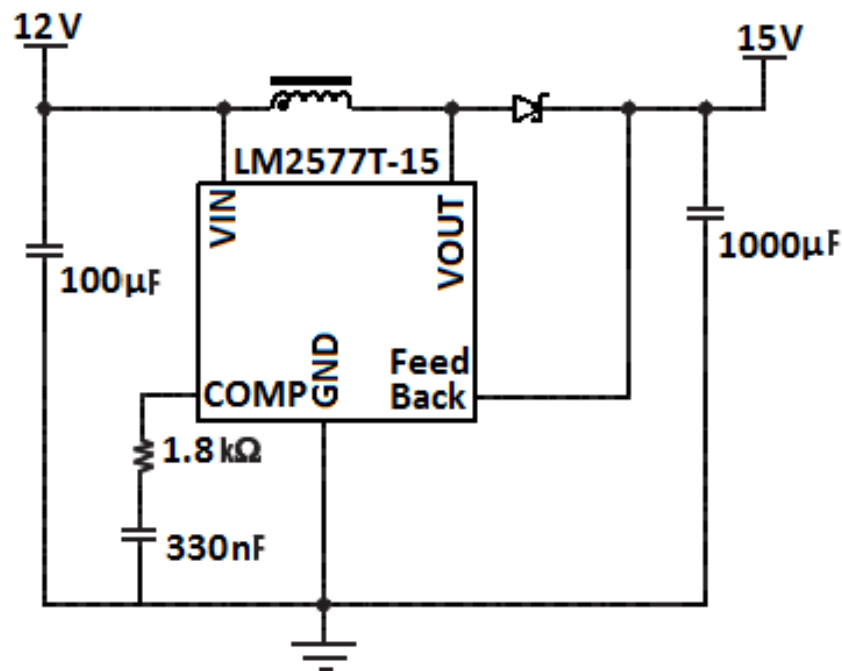


Figure 7.31: Schematic of the voltage regulator used to boost 12V to 15V

The microcontroller and the voltage sensors operate using a voltage level of 5V, in order to transform the input voltage provided by the battery to the necessary output voltage, the non isolated dc-dc converter, *AXA005A0X*, presented in figure 7.32 was used.



Figure 7.32: 12V to 15V DC-DC converter

The dc-dc converter specifications meet the necessary requirements for the 5V power supply and are presented in table 7.11.

Table 7.11: AXA005A0X specifications

| Parameter | Symbol | Value | Units |
| --- | --- | --- | --- |
| Input Voltage - Max | $V_{CCmax}$ | 10 | V |
| Input Voltage - Min | $V_{CCmin}$ | 14 | V |
| Output Current | $I_{out}$ | 5 | A |
| Output Voltage - Max | $V_{out(max)}$ | 5.5 | V |
| Output Voltage - Min | $V_{out(min)}$ | 0.75 | V |
| Efficiency | $\eta$ | 92 | % |
| Load Regulation | $\frac{\Delta V_{OUT}}{\Delta LOAD} \cdot 100\%$ | 0.4 | % |
| Minimum operating ambient Operating Temperature | $T_{Min}$ | -40 | °C |
| Maximum operating ambient Operating Temperature | $T_{Max}$ | 85 | °C |

The dc-dc converter transforms a voltage in the range of 10V to 14V to a regulated output voltage in the range of 0.75V to 5.5V depending on its $R_{TRIM}$ resistor. The electric schematic used for the 5V power supply is shown in figure 7.33.
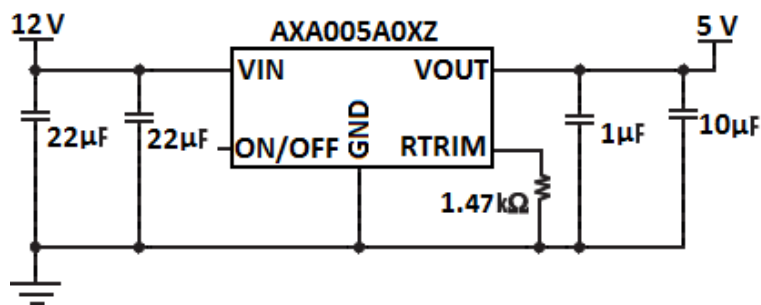


Figure 7.33: Schematic of the 5V power supply

The logic circuits need 3.3V in order to function properly, this voltage level is achieved by making use of a linear converter to reduce 5V to 3.3V, namely the *TLV1117-33CD* and its characteristics are presented in table 7.12.

Table 7.12: TLV1117-33CD linear converter characteristics

| Parameter | Symbol | Value | Units |
|---|---|---|---|
| Input Voltage - Max | $V_{CCmax}$ | 4.7 | V |
| Input Voltage - Min | $V_{CCmin}$ | 15 | V |
| Output Current | $I_{out}$ | 800 | mA |
| Output Voltage | $V_{out}$ | 5.5 | V |
| Load Regulation | $\frac{\Delta V_{OUT}}{\Delta LOAD} \cdot 100\%$ | 0.4 | % |
| Minimum operating ambient Operating Temperature | $T_{Min}$ | -40 | °C |
| Maximum operating ambient Operating Temperature | $T_{Max}$ | 125 | °C |

The schematic for the 3.3V linear converter is depicted in figure 7.34.
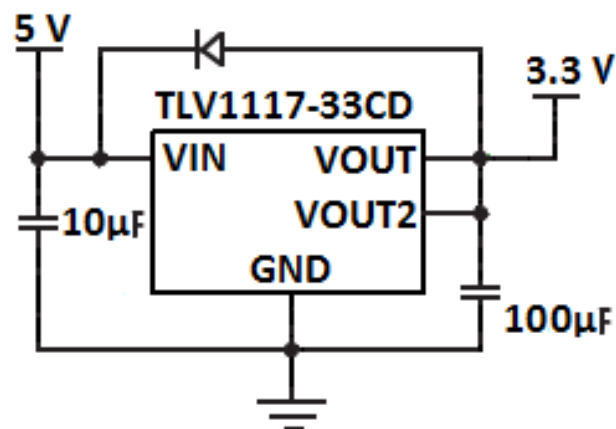


Figure 7.34: Schematic of the 3.3V linear converter

### 7.9.5 Board Prototype

At the beginning all the circuits above were validated using breadboards. To increase the board reliability, they were later merged into two printed circuit boards that are presented in the figures 7.36 and 7.35.
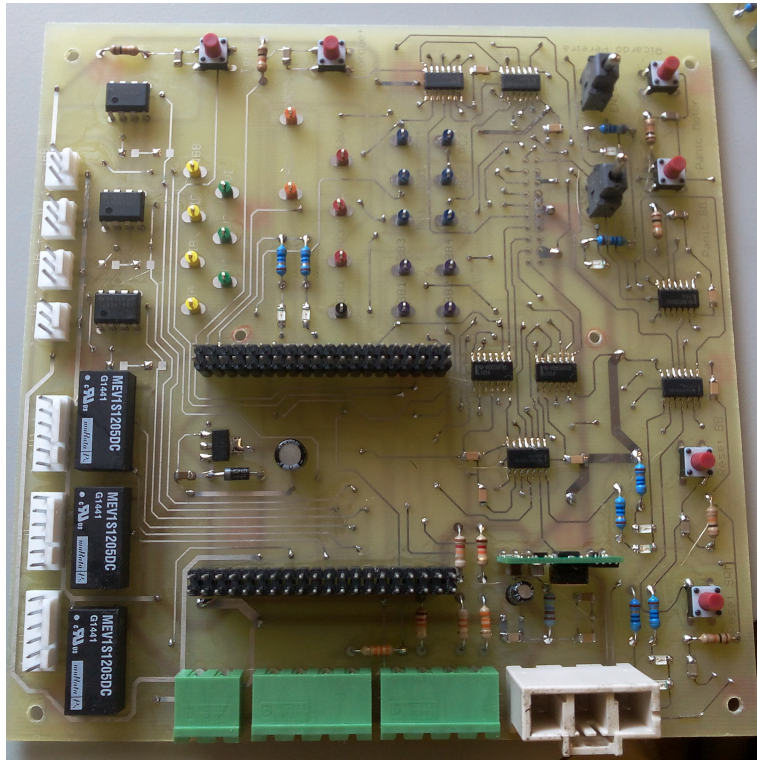
Figure 7.35: Top part of the board
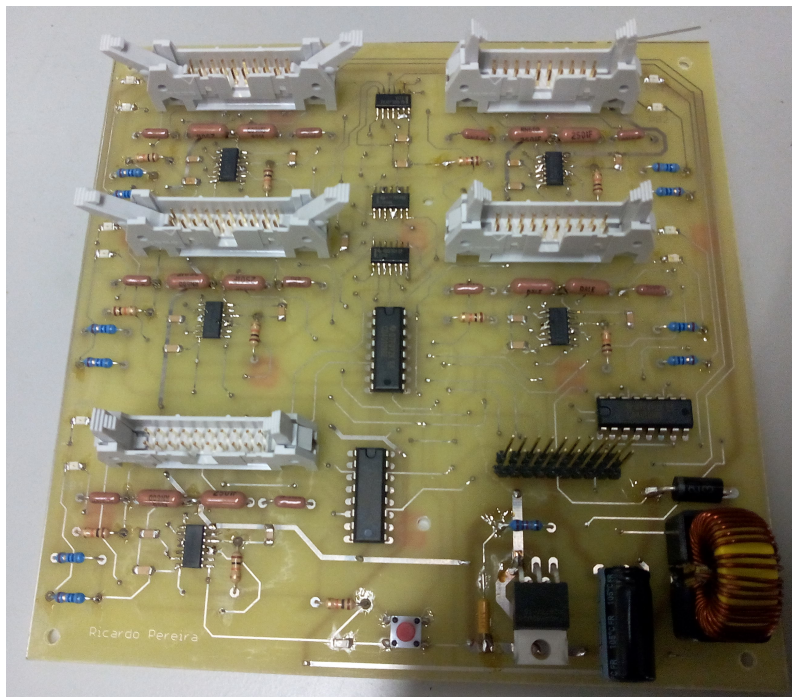


Figure 7.36: Bottom part of the board

The two printed circuit boards were designed so as to be assembled one in top of one another as can be seen in figure 7.37.
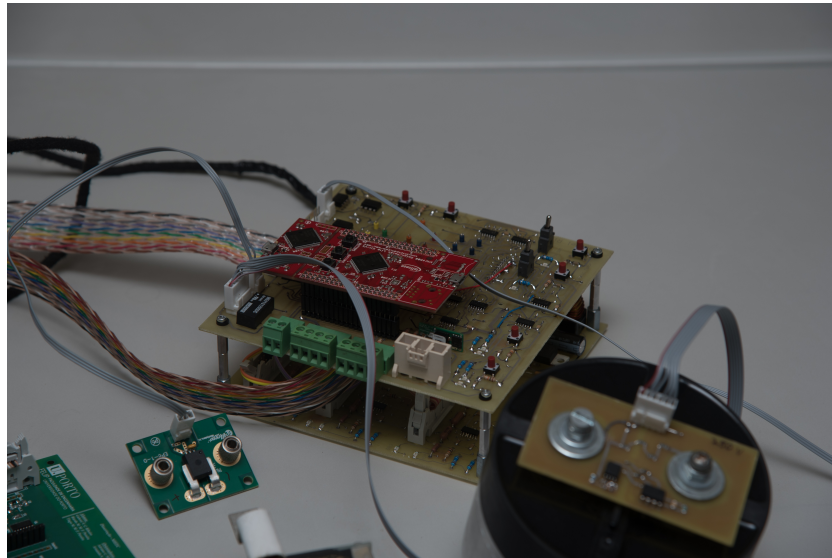


Figure 7.37: Developed board prototype

## 7.10 Conclusion

All the necessary steps for the preparation of the practical implementation of the switched reluctance motor drive were taken. Although the dissertation has a big theoretical component, the practical component began being prepared ever since the thesis was assigned to the student, and it was by far the thesis aspect that consumed most the students time. Despite some drawbacks such as the driver board being discontinued, all the components for the practical implementation were acquired, however there was not enough time to finish the power unit component, namely the assembly of the heat sink and consequently validate the control scheme.

# Chapter 8

# Conclusion

## 8.1 Final Remarks

The dissertation from the very beginning was a very ambitious project even though some of its contents were not entirely defined such as the motor rated power and voltage. As to make sure the components would arrive on time they were ordered months before they were needed, this is the reason why the semiconductors ratings are far superior than the ones required. As the project developed the student was entrusted with the task of designing the motor, which was originally going to be performed by the manufacturer *WEG*. This extra assignment although very attractive from a technical point of view, turned out to be a heavy burden considering the research that needed to be done on how to design a switched reluctance machine and the familiarization with the software Maxwell from ANSYS.

With all the dissertation goals set in stone, the steps taken to design the switched reluctance motor drive are essentially divided in the chapters. The approach taken was initially the review of the state of art of both the switched reluctance motor and the power converters used to drive it, followed by the current control schemes used for its control. As the dissertation advanced, the design of the motor began and with the characteristics of the simulated motor it was possible to develop a machine model in Simulink which was then used to devise the controller. The development of the hardware and test setup for experimental validation presented the main challenge in this dissertation. Despite being only present in chapter 7, more than two thirds of time spent during the project was focused on this final component.

All in all the dissertation final goal was accomplished, although only in simulation but still the results achieved were satisfactory.

## 8.2 Future work

Despite much of the proposed work has been completed, in order to finish the experimental validation there are still some tasks that need to be done. Starting from the assembly of the power converter on the heat-sink and the necessary tests on each semiconductor. From there the control

algorithm needs to be implemented on the XMC-4500. The motor is expected to arrive within the following weeks, upon its arrival it is necessary to confirm some of its parameters, namely the unsaturated aligned and unaligned inductance. As to finish the assembly of the bench test, the power converter needs to be connected to the motor terminals and the motor shaft needs to be coupled to a load, a torque sensor and the encoder. After having the bench test assembled, the control algorithm can be validated by comparing the torque reference with the output of the torque sensor. It would also be interesting to test the motor performance and extract its torque speed curve and efficiency and compare them with the simulation.

# Bibliography

[1] Yao Duan. *Method for design and optimization of surface mount permanent magnet machines and induction machines*. PhD thesis, Georgia Institute of Technology, 2010.

[2] R. Krishnan. *Switched Reluctance Motor Drives: Modeling, Simulation, Analysis, Design, and Applications*. Industrial Electronics. CRC Press, 2001.

[3] TJE Miller. *Electronic Control of Switched Reluctance Machines*. Newnes Power Engineering Series. Elsevier Science, 2001.

[4] B.M. Wilamowski and J.D. Irwin. *Power Electronics and Motor Drives*. Taylor & Francis, 2011.

[5] T.L. Skvarenina. *The Power Electronics Handbook*. Industrial Electronics. CRC Press, 2001.

[6] T.J.E. Miller. *Brushless permanent-magnet and reluctance motor drives*. Monographs in electrical and electronic engineering. Clarendon Press, 1989.

[7] Wadah Abass Aljaism. *Switched Reluctance Motor: Design, Simulation and Control*. PhD thesis, University of Western Sydney, 2007.

[8] Radim Visinka. *3-Phase Switched Reluctance (SR) Sensorless Motor Control Using a 56F80x, 56F8100 or 56F8300 Device*. Texas Instruments, 2005. Application note AN1932.

[9] A. Hughes and B. Drury. *Electric Motors and Drives: Fundamentals, Types and Applications*. Elsevier Science, 2013.

[10] P. Srinivas and P. V. N. Prasad. Comparative analysis of DTC Based Switched Reluctance Motor Drive Using Torque Equation and FEA Models. *International Journal of Electrical, Computer, Electronics and Communication Engineering*, 8(3):498–503, 2014.

[11] Torsten Wichert. *Design and Construction Modifications of Sswitched Reluctance Machines*. PhD thesis, Warsaw University of Technology, 2008.

[12] Michael T. DiRenzo. *Switched Reluctance Motor Control – Basic Operation and Example Using the TMS320F240*. Texas Instruments, 2000. Application Report SPRA420A.

[13] T. J. E. Miller. Converter volt-ampere requirements of the switched reluctance motor drive. *IEEE Transactions on Industry Applications*, IA-21(5):1136–1144, Sept 1985.

[14] Han-Kyung Bae. *Control of Switched Reluctance Motors Considering Mutual Inductance.* PhD thesis, Virgina Polytechnic Institute and State University, Blacksburg, Virginia, August 2000.

[15] H. Cheng, H. Chen, and Z. Yang. Average torque control of switched reluctance machine drives for electric vehicles. *IET Electric Power Applications*, 9(7):459–468, 2015.

[16] O. Ellabban and H. Abu-Rub. Torque control strategies for a high performance switched reluctance motor drive system. In *GCC Conference and Exhibition (GCC), 2013 7th IEEE*, pages 257–262, Nov 2013.

[17] Christian Carstensen. *Eddy Currents in Windings of Switched Reluctance Machines.* PhD thesis, University of Aachen, 2008.

[18] Y. Sozer and D. A. Torrey. Optimal turn-off angle control in the face of automatic turn-on angle control for switched-reluctance motors. *IET Electric Power Applications*, 1(3):395–401, May 2007.

[19] Y. Z. Xu, R. Zhong, L. Chen, and S. L. Lu. Analytical method to optimise turn-on angle and turn-off angle for switched reluctance motor drives. *IET Electric Power Applications*, 6(9):593–603, November 2012.

[20] R. B. Inderka and R. W. A. A. De Doncker. Ditc-direct instantaneous torque control of switched reluctance drives. *IEEE Transactions on Industry Applications*, 39(4):1046–1051, July 2003.

[21] H. Zeng, H. Chen, and J. Shi. Direct instantaneous torque control with wide operating range for switched reluctance motors. *IET Electric Power Applications*, 9(9):578–585, 2015.

[22] Huijun Wang, Dong-Hee Lee, and Jin-Woo Ahn. Torque ripple reduction of srm using advanced direct instantaneous torque control scheme. In *Electrical Machines and Systems, 2007. ICEMS. International Conference on*, pages 492–496, Oct 2007.

[23] JIn-Woo Ahn. *Torque Control*, chapter Switched Reluctance Motor. InTech, February 2011.

[24] P. G. Barrass and B. C. Mecrow. Flux and torque control of switched reluctance machines. *IEE Proceedings - Electric Power Applications*, 145(6):519–527, Nov 1998.

[25] Predictive pwm-based direct instantaneous torque control of switched reluctance drives. In *Power Electronics Specialists Conference, 2006. PESC '06. 37th IEEE*, pages 1–7, June 2006.

[26] T. H. Kim, D. H. Lee, and J. W. Ahn. Advanced non-linear logic torque sharing function of srm for torque ripple reduction. In *INTELEC 2009 - 31st International Telecommunications Energy Conference*, pages 1–4, Oct 2009.

[27] D. S. Schramm, B. W. Williams, and T. C. Green. Torque ripple reduction of switched reluctance motors by phase current optimal profiling. In *Power Electronics Specialists Conference, 1992. PESC '92 Record., 23rd Annual IEEE*, pages 857–860 vol.2, Jun 1992.

[28] M. Ilic-Spong, T. J. E. Miller, S. R. Macminn, and J. S. Thorp. Instantaneous torque control of electric motor drives. *IEEE Transactions on Power Electronics*, PE-2(1):55–61, Jan 1987.

[29] I. Husain and M. Ehsani. Torque ripple minimization in switched reluctance motor drives by pwm current control. *IEEE Transactions on Power Electronics*, 11(1):83–88, Jan 1996.

[30] S. K. Sahoo, S. K. Panda, and Jian-Xin Xu. Indirect torque control of switched reluctance motors using iterative learning control. *IEEE Transactions on Power Electronics*, 20(1):200–208, Jan 2005.

[31] W. Peng, K. Niyomsatian, J. Van den Keybus, A. C. Pop, and J. Gyselinck. Switched reluctance machine drives for electrical vehicle propulsion - optimal control with regard to the losses in machine and converter. In *Ecological Vehicles and Renewable Energies (EVER), 2015 Tenth International Conference on*, pages 1–10, March 2015.

[32] X. D. Xue, K. W. E. Cheng, and S. L. Ho. Optimization and evaluation of torque-sharing functions for torque ripple minimization in switched reluctance motor drives. *IEEE Transactions on Power Electronics*, 24(9):2076–2090, Sept 2009.

[33] A. C. Pop, V. Petrus, C. S. Martis, V. Iancu, and J. Gyselinck. Comparative study of different torque sharing functions for losses minimization in switched reluctance motors used in electric vehicles propulsion. In *Optimization of Electrical and Electronic Equipment (OPTIM), 2012 13th International Conference on*, pages 356–365, May 2012.

[34] Ahmed O. Khalil. *MODELING AND ANALYSIS OF FOUR QUADRANT SENSORLESS CONTROL OF A SWITCHED RELUCTANCE MACHINE OVER THE ENTIRE SPEED RANGE*. PhD thesis, University of Akron, 2005.

[35] Alexey Matveev. *Development of Methods, Algorithms and Software for Optimal Design of Switched Reluctance Machine Drives*. PhD thesis, University Eindhoven, 2006.

[36] A. Emadi. *Advanced Electric Drive Vehicles*. Energy, Power Electronics, and Machines. Taylor & Francis, 2014.

[37] I. Husain. Minimization of torque ripple in srm drives. *IEEE Transactions on Industrial Electronics*, 49(1):28–39, Feb 2002.

[38] R. Vandana, S. Nikam, and B. G. Fernandes. Criteria for design of high performance switched reluctance motor. In *Electrical Machines (ICEM), 2012 XXth International Conference on*, pages 129–135, Sept 2012.

[39] A. V. Radun. Design considerations for the switched reluctance motor. *IEEE Transactions on Industry Applications*, 31(5):1079–1087, Sep 1995.

[40] K. Ohyama, Y. Nakazawa, K. Nozuka, H. Fujii, H. Uehara, and Y. Hyakutate. Design of high efficient switched reluctance motor for electric vehicle. In *Industrial Electronics Society, IECON 2013 - 39th Annual Conference of the IEEE*, pages 7325–7330, Nov 2013.

[41] P. Rafajdus, P. Dubravka, A. Peniak, J. Saitz, and L. Szabo. Design procedure of switched reluctance motor used for electric car drive. In *Power Electronics, Electrical Drives, Automation and Motion (SPEEDAM), 2014 International Symposium on*, pages 112–117, June 2014.

[42] A. Labak and N. C. Kar. Outer rotor switched reluctance motor design for in-wheel drive of electric bus applications. In *Electrical Machines (ICEM), 2012 XXth International Conference on*, pages 418–423, Sept 2012.

[43] J. Faiz and J. W. Finch. Aspects of design optimisation for switched reluctance motors. *IEEE Transactions on Energy Conversion*, 8(4):704–713, Dec 1993.

[44] A. Labak and N. C. Kar. Development and analysis of a five-phase pancake shaped switched reluctance motor. In *Electrical Machines (ICEM), 2010 XIX International Conference on*, pages 1–6, Sept 2010.

[45] T. J. E. Miller. Optimal design of switched reluctance motors. *IEEE Transactions on Industrial Electronics*, 49(1):15–27, Feb 2002.

[46] P. J. Lawrenson, J. M. Stephenson, P. T. Blenkinsop, J. Corda, and N. N. Fulton. Variable-speed switched reluctance motors. *IEE Proceedings B - Electric Power Applications*, 127(4):253–265, July 1980.

[47] T.J.E. Miller. *Switched Reluctance Motors and Their Control*. Monographs in electrical and electronic engineering. Magna Physics, 1993.

[48] Liuchen Chang. Design procedures of a switched reluctance motor for automobile applications. In *Electrical and Computer Engineering, 1996. Canadian Conference on*, volume 2, pages 947–950 vol.2, May 1996.

[49] J. W. Finch, J. Faiz, and H. M. B. Metwally. Design study of switched reluctance motor performance. In *Industry Applications Society Annual Meeting, 1992., Conference Record of the 1992 IEEE*, pages 242–248 vol.1, Oct 1992.

[50] W. Tong. *Mechanical Design of Electric Motors*. CRC Press, 2014.

[51] C. S. Edrington, M. Krishnamurthy, and B. Fahimi. Bipolar switched reluctance machines: A novel solution for automotive applications. *IEEE Transactions on Vehicular Technology*, 54(3):795–808, May 2005.

[52] B. C. Mecrow. New winding configurations for doubly salient reluctance machines. *IEEE Transactions on Industry Applications*, 32(6):1348–1356, Nov 1996.

[53] G. J. Li, J. Ojeda, E. Hoang, M. Lecrivain, and M. Gabsi. Comparative studies between classical and mutually coupled switched reluctance motors using thermal-electromagnetic analysis for driving cycles. *IEEE Transactions on Magnetics*, 47(4):839–847, April 2011.

[54] B. C. Mecrow, A. C. Clothier, P. G. Barrass, and C. Weiner. Drive configurations for fully-pitched winding switched reluctance machines. In *Industry Applications Conference, 1998. Thirty-Third IAS Annual Meeting. The 1998 IEEE*, volume 1, pages 563–570 vol.1, Oct 1998.

[55] W.G. Hurley and W.H. Wölfle. *Transformers and Inductors for Power Electronics: Theory, Design and Applications*. EngineeringPro collection. Wiley, 2013.

[56] Praveen Vijayraghavan. *Design of Switched Reluctance Motors and Development of a Universal Controller for Switched Reluctance and Permanent Magnet Brushless DC Motor Drives*. PhD thesis, Virginia Tech, 2001.

[57] H. Le-Huy and P. Brunelle. A versatile nonlinear switched reluctance motor model in simulink using realistic and analytical magnetization characteristics. In *31st Annual Conference of IEEE Industrial Electronics Society, 2005. IECON 2005.*, pages 6 pp.–, Nov 2005.

[58] T. Benamimour, A. Bentounsi, H. Djeghloud, and I. Bouchareb. Finite element modeling and dynamic simulation of nonlinear vrm using matlab. In *Modeling, Simulation and Applied Optimization (ICMSAO), 2013 5th International Conference on*, pages 1–5, April 2013.

[59] H.A. Toliyat and G.B. Kliman. *Handbook of Electric Motors*. Electrical and computer engineering. CRC Press, 2004.

[60] C. R. Neuhaus, R. W. De Doncker, and N. H. Fuengwarodsakul. Control scheme for switched reluctance drives with minimized dc-link capacitance. In *2007 7th International Conference on Power Electronics and Drive Systems*, pages 501–506, Nov 2007.

[61] W. Suppharangsan and J. Wang. Experimental validation of a new switching technique for dc-link capacitor minimization in switched reluctance machine drives. In *Electric Machines Drives Conference (IEMDC), 2013 IEEE International*, pages 1031–1036, May 2013.

[62] H. Wu, D. Winterborne, M. Ma, V. Pickert, and J. Widmer. Dc link capacitors for traction srm drives in high temperature automotive environments: A review of current issues and solutions. In *Hybrid and Electric Vehicles Conference 2013 (HEVC 2013), IET*, pages 1–6, Nov 2013.

[63] Shumei Cui, Lei Hu, Chao Zhang, Shouliang Han, and Wei Zheng. Research on temperature characteristic of dc-link capacitors applied in electric vehicles. In *Transportation Electrification Asia-Pacific (ITEC Asia-Pacific), 2014 IEEE Conference and Expo*, pages 1–5, Aug 2014.

[64] Infineon. *IGBT Power Losses Calculation Using the Data-Sheet Parameters*. Application Note V1.1. January 2009.

[65] S. Maniktala. *Switching Power Supplies A - Z.* Elsevier Science, 2012.

[66] Semikron. *Gate Resistor – Principles and Applications*. Application Note 7003. November 2007.

[67] Infineon. *Gate resistor for power devices*. Application Note AN2015-07. June 2015.

[68] Onsemi. *IGBT Gate Drive Considerations*. Application Note AND9052/D. October 2011.